

DOE/ER/3072-20

Princeton University  
Elementary Particles Laboratory  
Department of Physics

FORWARD PRODUCTION OF HIGH MASS MUON  
PAIRS IN PION-NUCLEON INTERACTIONS

Sandro Palestini

December 1984



**FORWARD PRODUCTION  
OF HIGH MASS MUON PAIRS  
IN PION-NUCLEON INTERACTIONS**

by

**Sandro Palestini**

**A dissertation  
presented to the  
Faculty of Princeton University  
in partial fulfillment of the requirements  
for the degree of  
Doctor of Philosophy  
in the  
Department of Physics**

**Princeton, New Jersey  
© Sandro Palestini, 1984**

**ABSTRACT**

The production of muon pairs in negative pion-nucleon interactions has been studied at a center-of-mass energy of 12.2 GeV. About 4000 events have been collected over a broad range of longitudinal momentum and invariant mass. A comparison with the Drell-Yan Model has been made, confirming the factorization hypothesis. The results favor a non-vanishing value of the pion structure function at the kinematic limit of large longitudinal momentum. Other departures from the standard parton-QCD model are found in this region. The angular distribution of the muon pair becomes characteristic of longitudinal virtual photon polarization, and the transverse momentum of the pair is found to decrease.



ADD 1885

# CONTENTS

	Page
Acknowledgements . . . . .	vii
List of Tables . . . . .	ix
List of Figures . . . . .	xi
Chapter 1. Introduction . . . . .	1
Chapter 2 The Drell-Yan Process . . . . .	5
2.1 Lepton pair production in the approximation of free partons	5
2.2 The factorization hypothesis . . . . .	7
2.3 Scale invariance . . . . .	10
2.4 Transverse momentum and quark masses . . . . .	10
2.5 Angular distribution . . . . .	11
2.6 Other predictions . . . . .	12
Chapter 3 QCD and lepton pair production . . . . .	14
3.1 Overview of the chapter . . . . .	14
3.2 Scale dependence of the quark density functions . . . . .	14
3.3 Higher order diagrams and the leading log approximations	15
3.4 The K-factor and complete higher order computations .	18
3.5 Transverse momentum . . . . .	19
3.6 Angular distribution . . . . .	20
Chapter 4 Experimental program and detector guidelines . . . . .	23
4.1 Experimental goal . . . . .	23
4.2 Overview of the detector design . . . . .	24
4.3 Target . . . . .	27

4.4 Selection magnet . . . . .	27
4.5 Wire chambers . . . . .	31
4.6 Spectrometer magnet . . . . .	34
4.7 Scintillator banks . . . . .	34
Chapter 5 Detector trigger . . . . .	40
5.1 Trigger levels . . . . .	40
5.2 Level-1 trigger . . . . .	40
5.3 Level-2 trigger . . . . .	43
5.4 Level-3 trigger . . . . .	43
Chapter 6 Data collection and detector efficiency . . . . .	54
6.1 Beam line characteristics . . . . .	54
6.2 Beam composition . . . . .	56
6.3 Beam momentum measurement . . . . .	57
6.4 Intensity monitor . . . . .	58
6.5 Spill structure, detector dead-time and trigger time resolution . . . . .	58
6.6 Particle rates in the detector . . . . .	60
6.7 On-line tests and data acquisition . . . . .	61
6.8 Off-line trigger tests . . . . .	62
6.9 Scintillator efficiency studies . . . . .	63
6.10 Chamber alignment and calibration . . . . .	69
Chapter 7 Event reconstruction . . . . .	71
7.1 Overview of the data analysis . . . . .	71
7.2 Off-line trigger enforcement . . . . .	72
7.3 Cuts on record length . . . . .	74
7.4 Upstream chamber reconstruction . . . . .	74
7.5 Downstream reconstruction . . . . .	77
7.6 Global fitting . . . . .	80
7.7 Multiple scattering and transport in the selection magnet	84
Chapter 8 Event selection . . . . .	94
8.1 Elimination of beam-halo . . . . .	94
8.2 Further event selection . . . . .	99
Chapter 9 Montecarlo simulation and acceptance correction . . . . .	104
9.1 Description of the method . . . . .	104

9.2 Acceptance computation . . . . .	106	14.2 Comparison with expectations . . . . .	179
9.3 Features of the Montecarlo program . . . . .	108	Chapter 15 Overview of results . . . . .	180
9.4 Fluctuations in the center-of-mass energy . . . . .	110	References . . . . .	183
9.5 Detector acceptance and losses due to cuts . . . . .	111		
9.6 Measurement resolution . . . . .	114		
9.7 Contamination from resonance production . . . . .	115		
9.8 Data and Montecarlo detector illumination . . . . .	116		
Chapter 10 Cross section normalization . . . . .	120		
10.1 Chapter outline . . . . .	120		
10.2 Effective absorption cross section and acceptance . . . . .	120		
10.3 Beam intensity dependence . . . . .	122		
10.4 Beam flux normalization . . . . .	125		
10.5 Normalization uncertainty estimate and corrections . . . . .	128		
10.6 Secondary interactions . . . . .	130		
Chapter 11 Mass and longitudinal momentum fraction dependence of the cross section . . . . .	132		
11.1 Variables and method . . . . .	132		
11.2 Results . . . . .	133		
Chapter 12 Structure functions . . . . .	139		
12.1 Definition of variables and method . . . . .	139		
12.2 Results – Factorization . . . . .	142		
12.3 Shape of the pion structure function . . . . .	143		
12.4 Systematic effects in determining $F_{\pi}$ . . . . .	148		
12.5 Fit of the nucleon structure function . . . . .	150		
12.6 Systematic effects related to $F_N$ . . . . .	151		
12.7 Normalization of the structure functions and K-factor . . . . .	154		
12.8 Summary of results on the structure functions . . . . .	157		
Chapter 13 Angular distribution . . . . .	158		
13.1 Reference axes . . . . .	158		
13.2 Analysis procedure . . . . .	159		
13.3 Results . . . . .	160		
13.4 Summary and comments . . . . .	166		
Chapter 14 Transverse momentum distribution . . . . .	174		
14.1 Definition of variables and results . . . . .	174		

## ACKNOWLEDGMENTS

The experiment described in this dissertation has been performed with a collaboration of researchers from three Universities. I am particularly indebted to the persons who shared the collection of the data analyzed in this thesis: Kelby J. Anderson, Cristina Biino Palestini, John S. Conway, John F. Greenhalgh, Joel G. Heinrich, Bill C. Louis, Kirk T. McDonald, Jim E. Pilcher, Eli I. Rosenberg, and Frank C. Shoemaker.

Frank Shoemaker improved considerably my knowledge of hardware. Bill Louis was particularly helpful in the development of software. The analysis has been carried out with the collaboration of Cristina Biino. I also thank A.J. Stewart Smith, Jim Pilcher, Eli Rosenberg, Kelby Anderson, Chris E. Adolphsen and Jim P. Alexander for several helpful discussions.

My advisor Kirk McDonald has been of guidance throughout all the work, being always available for the discussion of my progress. I am also particularly grateful to him for the considerable effort he spent on the various drafts of this dissertation.

I wish to thank the technical staff of the Princeton University for the fast and competent construction of various parts of the detector. The Fermilab staff was also of great assistance.

During the last part of this work, I was personally supported by

the INFN, sez. Torino.

At the end of what appears to me as a long and intense stay, I wish to thank the Department of Physics at Princeton University for offering me the possibility of conducting research work in a very stimulating environment. I hope that new collaborations will be possible in the future.

Finally, I want to thank again my wife Cristina, who was particularly helpful during the analysis, and who shared all the efforts of completing this research project.

## LIST OF TABLES

	Page
I Target specifications . . . . .	28
II Map of the field integral of the spectrometer magnet . . . . .	35
III Length cuts applied to the event data string . . . . .	75
IV Parameters $I_n$ for track fitting in the fringe field of the spectrometer magnet . . . . .	82
V Parameters for multiple scattering $\chi^2$ in the hadron absorber	86
VI Parameters for the transport equations in the selection magnet . . . . .	90
VII Results of the ion chamber calibrations . . . . .	127
VIII Cross section $d^2\sigma/dx_F dM$ . . . . .	137
IX Pion structure function . . . . .	145
X Nucleon structure function . . . . .	145
XI Functional fits to the pion structure function . . . . .	146
XII Table of residuals between $d^2\sigma/dx_1 dx_2$ and the fit from the structure functions . . . . .	147
XIII Functional fit to the nucleon structure function . . . . .	151
XIV Parametrization of the quark densities . . . . .	153
XV Value of $K_f$ for different $F_\pi, F_N$ parametrizations . . . . .	156
XVI Value of the parameter $\lambda$ in $d\sigma/d\cos\theta \propto 1 + \lambda\cos^2\theta$ . . . . .	161
XVII Value of the angular distribution parameters . . . . .	163
XVIII Value of the parameter $\lambda$ vs. $x_1$ . . . . .	167
XIX Value of the parameter $\lambda$ vs. $x_1$ , in smaller bins . . . . .	170
XX Value of the parameter $\lambda$ vs. $x_F$ . . . . .	172
XXI Values of $\langle P_T \rangle$ and $\langle P_T^2 \rangle$ vs. $x_F$ . . . . .	178

## LIST OF FIGURES

	Page
2.1 Basic diagram for hadronic production of $l^+l^-$ pairs in the Drell-Yan Model . . . . .	6
3.1 Some higher order QCD subprocesses contributing to massive lepton pair production . . . . .	16
3.2 Higher twist contribution to lepton pair production at large $x_F$ in pion-nucleon interactions . . . . .	21
4.1 E615 detector layout . . . . .	26
4.2 Side view of the selection-magnet . . . . .	29
4.3 Top view of the selection-magnet . . . . .	30
4.4 Layout of the wire chambers; top view . . . . .	32
4.5 Scheme of the inclination and denomination of the wire planes . . . . .	33
4.6 Arrangement of the $C$ bank of scintillators . . . . .	36
4.7 Arrangement of the $D$ bank . . . . .	37
4.8 Arrangement of the $E$ and $F$ banks . . . . .	39
5.1 Flow chart of the trigger logic . . . . .	41
5.2 Illustration of the Level-3 trigger . . . . .	44
5.3 On-line display of pair multiplicity in the trigger processor . . . . .	47
5.4 Level-1 trigger logic scheme . . . . .	48
5.5 Summing network for Level-1 . . . . .	49
5.6 ECL circuitry for the scintillator latch modules . . . . .	50
5.7 ECL circuitry for the pad-latch modules . . . . .	51
5.8 Flow chart of the Level-3 track finder . . . . .	52
5.9 Flow chart of the memory look-up procedure . . . . .	53
6.1 Scheme of the secondary beam transport in the FNAL Proton-West area . . . . .	55
6.2 Secondary beam momentum spectrum for the 80 GeV/c data collection . . . . .	57
6.3 Efficiency profile of the scintillator banks . . . . .	65
6.4 Efficiency profile for the MWPC n. 8 and DC n. 9 . . . . .	66
6.5 Beam intensity dependence of the inefficiency in the $Cu$ and $Du$ banks . . . . .	67
7.1 Plot from the track reconstruction program . . . . .	73
7.2 Hit multiplicity distributions for wire chambers . . . . .	76
7.3 Spectrum of the time-offset for the DC track reconstruction . . . . .	79
7.4 Track fitting in the spectrometer magnet area: determination of the effective magnetic center . . . . .	81
7.5 Track fitting in the spectrometer magnet area: correction for magnetic field effects in the wire chamber regions . . . . .	81
7.6 Track fitting in the spectrometer magnet area: correction for effects in the the $y-z$ plane . . . . .	81
7.7 Difference between upstream and downstream track segments at the spectrometer magnet center . . . . .	83
7.8 Variables used in the multiple scattering formalism . . . . .	84
7.9 Mass spectra in the $J/\Psi$ region for different methods to estimate the trajectory parameters at the target . . . . .	88
7.10 Mass spectra obtained with different methods and momentum intervals . . . . .	91
7.11 Montecarlo simulated mass spectra for different methods . . . . .	92

8.1 Momentum vs. polar angle scatter plots, before beam-muon cuts . . . . .	95,96	13.6 $d^2\sigma/dx_1d\cos\theta$ , vs. $\cos\theta$ , in $x_1$ intervals . . . . .	168
8.2 Momentum vs. polar angle scatter plots, after all cuts . . . . .	97,98	13.7 $\lambda$ vs. $x_1$ in the $t$ -channel . . . . .	169
8.3 Track illumination of the DC plane n. 5 . . . . .	100	13.8 $\lambda$ vs. $x_F$ in the $t$ -channel . . . . .	171
8.4 Vertex probability distributions . . . . .	101	13.9 $\lambda$ vs. $x_1$ in the $t$ -channel, with superimposed curve . . . . .	173
8.5 Montecarlo plots for vertex probability distributions . . . . .	102	14.1 $\frac{1}{P_T}d^2\sigma/dx_FdP_T$ vs. $P_T$ , in $x_F$ intervals . . . . .	175
9.1–4 Detector acceptance vs. $M$ , $x_F$ , $x_1$ , $x_2$ . . . . .	112	14.2 $\langle P_T \rangle$ vs. $x_F$ . . . . .	177
9.5–8 Detector acceptance vs. $\cos\theta_t$ , $\phi$ , $P_T$ . . . . .	113	14.3 $\langle P_T^2 \rangle$ vs. $x_F$ . . . . .	177
9.9 Illumination of the detector by tracks with momentum 10 < $P$ < 25 GeV/c . . . . .	117	14.4 Detector efficiency vs. $P_T$ for $x_F > 0.9$ . . . . .	179
9.10 Illumination of the detector by tracks with momentum 25 < $P$ < 40 GeV/c . . . . .	118		
9.11 Illumination of the detector by tracks with momentum $P > 40$ GeV/c . . . . .	119		
11.1 $d^2\sigma/dx_FdM$ vs. $M$ for different $x_F$ intervals . . . . .	134		
11.2 $d\sigma/dM$ vs. $M$ , for $x_F > 0.2$ . . . . .	135		
11.3 $d^2\sigma/dx_FdM$ vs. $x_F$ , for different $M$ intervals . . . . .	136		
11.4 $d\sigma/dx_F$ vs. $X_F$ (for $M > 4$ GeV/c <sup>2</sup> ) . . . . .	136		
11.5 $M^3d\sigma/dM$ vs. $\sqrt{\tau}$ , for $x_F > 0.2$ . . . . .	138		
12.1 Scatterplot of the data in $x_1$ - $x_2$ . . . . .	141		
12.2 Pattern of the $x_1$ - $x_2$ cells used in the structure functions fit . . . . .	141		
12.3 Fit for $F_\pi(x_1)$ . . . . .	144		
12.4 Fit for $F_N(x_2)$ . . . . .	144		
12.5 Momentum distribution of beam-muons . . . . .	149		
12.6 Comparison of $F_N$ with parametrizations of quark densities . . . . .	152		
13.1 Definition of $t$ -channel (Gottfried-Jackson) axes . . . . .	159		
13.2 $d\sigma/d\cos\theta$ vs. $\cos\theta$ . . . . .	162		
13.3 $d^2\sigma/dx_1d\cos\theta$ , vs. $\cos\theta$ , in $x_1$ intervals— $t$ -channel . . . . .	164		
13.4 $d^2\sigma/dx_1d\cos\theta$ , vs. $\cos\theta$ , in $x_1$ intervals— $CS$ -channel . . . . .	165		
13.5 $\lambda$ vs. $x_1$ . . . . .	166		



## Chapter 1

### INTRODUCTION

The study of the fundamental constituents of matter has been a central issue in the history of Physics. This century began with the important discovery of the nucleus, which also represented a development of the methods of investigation: since the traditional tools were unable to provide information about systems smaller than the wavelength of light, subatomic particles themselves were used as a probe of the deeper structure of matter.

Quantum mechanics tells us that a system with momentum  $P$  is associated with a wave of wavelength  $\lambda = h/P$ , where  $h$  is the Planck constant, so that probes of large momentum are needed to observe small structures. Particle accelerators were developed, and new levels of fundamental constituents were discovered as higher energies became available.

Among the important discoveries which followed, I shall mention the measurement of the nuclear size and the study of its main constituents, protons and neutrons. More recently studies performed at higher energies showed that these particles have internal structure of their own. Furthermore, different kinds of new, unstable and resonant states of nuclear matter were identified.

The number of new particles became so large that physicists

started working on models where a small number of new, fundamental entities would explain the complex spectra of the states found in nature. The concept of **quarks** was introduced in 1964<sup>1</sup> as the fundamental representation of a unitary symmetry approximately satisfied by the **hadrons**—the particles subject to nuclear interactions. The quantum number which distinguishes one type of quark from another is called the **flavor**. At present 6 flavors are believed to exist. Quarks also have the unusual property of carrying fractional electric charge,  $1/3$  or  $2/3$  of the electron charge. Combinations of three quarks, or of a quark and antiquark, can reproduce the quantum numbers of any known hadron.

In the following years the concept of hadron constituents was also suggested by experimental observations which probed the structure of the hadrons. The study of inelastic scattering of electrons off protons showed that in the case of very large energy and momentum transfer the target particle behaves like a distribution of free, pointlike objects, which were called **partons**.<sup>2</sup> This discovery is of the same kind as finding the nucleus inside the atom or finding protons and neutrons inside the nucleus. Still, an important difference arises this time: the new constituents have never been detected as free particles, but they seem to exist only inside hadrons when we probe them with sufficiently high energy.

The theory of **Quantum Chromo-Dynamics (QCD)**<sup>3</sup> was formulated in the 1970's to describe the interaction between hadrons in terms of their pointlike constituents. QCD is a gauge theory based on the unitary symmetry  $SU(3)$ . Each flavor of quark exists in three kinds of **colors**, interacting with eight vector fields called **gluons**. Perturbative calculations show that the theory is characterized by **asymptotic freedom**:<sup>4</sup> the effective coupling constant becomes small at large energy and momentum transfers. In this region the results

of the free-parton model are reproduced and explained. On the other hand, QCD is expected to predict the confinement of quarks and gluons. This is a non-perturbative subject and no definitive answer has been given yet.

Today QCD seems to be very successful in explaining numerous and different aspects of the hadronic interactions at high energy. Nevertheless, we cannot exclude the possibility of different scenarios, both for lack of experimental information, and because of the computational complexity of the model. It is therefore very important to perform precise measurements of phenomena which can test our understanding of the dynamics of the interactions between quarks and gluons.

This thesis will describe an experimental study of the production of leptonic pairs in hadronic collisions, a phenomenon which in the 1970's gave strong support to the parton model and to the identification of partons as quarks and gluons.<sup>5</sup>

This inelastic scattering is known as **Drell-Yan Process**, from the authors who described it as the annihilation of a quark from one hadron with an antiquark from the other, producing a virtual photon that subsequently materializes into a  $l^+l^-$  pair.<sup>6</sup> The process is fundamentally electromagnetic, and in first approximation the only effect of the strong interaction is to determine the momentum distribution of the quarks bound inside the hadrons.

Most of the properties of lepton pair production are shown to be predicted by the **naïve parton model**. Still, effects of the strong binding between quarks have been predicted, and some departures from the simplest model have been measured.

This work will discuss the topic of  $\mu^+\mu^-$  production in pion-nucleon interactions. We shall study the case where the dimuon system carries away most of the available longitudinal momentum, to-

gether with a large fraction of the total invariant mass of the colliding system. We shall address the topics of quark distributions in pions and nucleons, spin alignment of the virtual photon, transverse momentum of the lepton pair, and absolute normalization of the cross section. Each one of these subjects provides information about quark dynamics beyond the approximation of free parton model, and therefore allows us to test more deeply our knowledge of the strong interactions.

## Chapter 2

### THE DRELL-YAN PROCESS

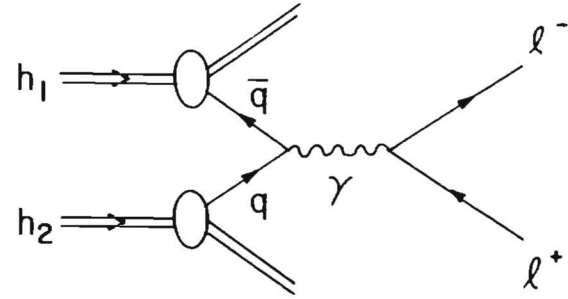


**Fig. 2.1** Basic diagram for hadronic production of  $l^+l^-$  pairs in the Drell-Yan Model.

#### 2.1 Lepton pair production in the approximation of free partons

The **parton model** describes deep inelastic hadronic scattering in terms of interactions involving quarks and gluons. It has been shown that a satisfactory and consistent description of the hard scattering phenomenology can be given in a reference system where the total momentum of the hadron is much larger than its mass.<sup>7</sup> The only effect of the quark binding interaction is contained in the quark density functions, which tell us the way partons share the total momentum of the hadron. To a first approximation, all the masses and the transverse momenta of the partons can be neglected.

Let us consider the production of a muon pair in the reaction  $h_1 h_2 \rightarrow \mu^+ \mu^- X$  (Figure 2.1).<sup>6,8</sup> Let  $m$  be the mass of the hadrons,  $P$  their momentum in the center-of-mass frame, and  $Q^2$  the square of the momentum transferred in the annihilation, equal to the square of the invariant mass of the pair. We shall indicate with  $s$  the **square of the center-of-mass energy**. The time scale of the annihilation process is determined by the lifetime of the virtual photon, which is related

to the invariant mass of the lepton pair:  $t_{DY} \approx 1/M_{l^+l^-} = 1/\sqrt{Q^2}$ .<sup>†</sup> This time scale must be compared to the typical time scale of the strong interactions, which is of the order of  $t_h \approx 1/m$ .<sup>‡</sup> Thus the approximation of quasi-free partons is satisfied as long as  $M_{l^+l^-} \gg m$ , in which case the annihilation can be described with the technique of the impulse approximation. In this regime, asymptotic QCD is approached, and it is conceivable to compute strong interaction effects with perturbative methods. Furthermore, the scattering is expected to take place incoherently among the different partons.

<sup>†</sup> We shall use units with  $\hbar = c = 1$ .

<sup>‡</sup> A third time scale is the one characteristic of the interaction among the constituents of each hadron before the collision takes place. This would be of the order of  $1/m$  in the rest frame of either hadron, but in the center-of-mass frame the relativistic transformation expands it to the order of  $\sqrt{s}/m^2$ . We conclude that we need  $\sqrt{s} \gg m$  for the parton model to hold.

## 2.2 The factorization hypothesis

The scattering probability for partons is computed assuming that they carry the same quantum numbers as quarks or gluons, that they are subjected to the electro-weak forces in the same way as leptons, except of course that quarks have different charges, and that they also interact according to ‘perturbative’ QCD. In order to compute the probability for the scattering between the parent particles, we need to know the **quark density functions**  $f(x)$ .<sup>7</sup> These are defined as the probability that a hadron contains a quark which carries fraction  $x$  of the longitudinal momentum of the hadron. The variable  $x$  is often called the **Feynman  $x$** . Note that the quark density functions are only well defined in situations where the momentum of the hadron is large compared to its mass. The parton model does not provide any systematic way of computing the quark densities. However they must satisfy the normalization condition that the total probability of finding a given type of quark is equal to the number of quarks in the hadron according to the static quark model.

Finally, the scattering is followed by the so called **fragmentation**, when the remaining quarks rearrange themselves to form detectable hadrons. This is again a non-perturbative topic, and the details are rather obscure. However, we shall deal with inclusive production of muon pairs at high energies, and we shall simply assign probability equal to one to the fragmentation process.

In the Drell-Yan literature, the approach we have just described is called the **factorization hypothesis**. In brief, the properties of the two initial hadrons are reflected only by their quark distributions, so that the differential cross section is simply their product times the quark scattering probability. Using the Feynman variables  $x_i$ , where  $i=1, 2$  refer to the two hadrons, the differential cross section can be

written in the following way:

$$\frac{d^2\sigma}{dx_1 dx_2} = \sum_{spins} \sum_q \left( \frac{d^2\hat{\sigma}_q}{dx_1 dx_2} \right) \left( f_1^q(x_1) \cdot f_2^q(x_2) + f_1^q(x_1) \cdot f_2^q(x_2) \right) \quad (2.1)$$

where the index  $q$  defines the quark-antiquark flavor, the  $f$ 's are the quark density functions, and  $\hat{\sigma}$  is the QED cross section for the annihilation of Dirac particles—the dependence on  $q$  comes from the quark charge.

We shall also use two other variables, which can be used in place of  $x_1$  and  $x_2$ . The first is the square of the ratio between the invariant mass of the lepton pair  $M$  and the center-of-mass energy:

$$\tau \equiv \frac{M^2}{s}. \quad (2.2)$$

In the limit that the transverse momentum and the mass of the quarks can be neglected then

$$\tau = x_1 x_2 \quad \text{and} \quad M^2 = x_1 x_2 s. \quad (2.3)$$

The second variable,  $x_F$ , is the ratio between the longitudinal momentum of the pair and the maximum value allowed for a given value of  $\tau$ . We first note that

$$P_L^{max} = \frac{\sqrt{s}}{2}(1 - \tau), \quad (2.4)$$

so that

$$x_F \equiv \frac{P_L}{P_L^{max}} = \frac{x_1 - x_2}{1 - \tau}. \quad (2.5)$$

This inverse relations are then

$$x_{1,2} = \frac{1}{2} \left( \pm x_F (1 - \tau) + \sqrt{x_F^2 (1 - \tau)^2 + 4\tau} \right). \quad (2.6)$$

Modifications to these relations for the case of finite transverse momentum will be given in Chapter 11.

The QED annihilation cross section between partons is the same as the cross section for  $e^+e^- \rightarrow \mu^+\mu^-$ , which is equal to  $(4\pi\alpha^2)/3M^2$ , but multiplied by the square of the parton charge. Inserting this expression into equation (2.1) and using equation (2.3) to eliminate  $M^2$  we obtain:

$$\frac{d^2\sigma}{dx_1 dx_2} = \frac{4\pi\alpha^2}{9s} \left( \frac{1}{x_1 x_2} \right)^2 \sum_q e_q^2 x_1 x_2 \left( f_1^q(x_1) f_2^{\bar{q}}(x_2) + f_1^{\bar{q}}(x_1) f_2^q(x_2) \right) \quad (2.7)$$

where  $e_q$  is the quark charge in units of the electron charge. Notice that the QED cross section has been multiplied by a factor 1/3 due to color: a quark of a given color has 1/3 probability of finding an anti-quark of the corresponding anti-color. This corresponds to the historical convention that the quark density functions  $f(x)$  are defined for a given flavor of quark by summing over all three colors.

Instead of using quark densities  $f(x)$  it is common to write parton cross sections in terms of **structure functions**  $F(x)$ , which are defined as momentum densities, and given by  $F(x) \equiv x \times f(x)$ .

The **strong factorization hypothesis** goes beyond what is written in equations (2.1) and (2.7) by stating the universality of the quark density functions: for each colliding hadron the same parton distribution enters the scattering probability for all conceivable parton scatterings. This is important for nucleons where the quark density is measured in deep inelastic lepton-hadron scattering experiments which are sensitive to the momentum distribution through the relation:

$$F_2(x) = \sum_i e_i^2 x f^i(x) \quad (2.8)$$

where the index  $i$  runs over all the quarks and antiquarks. The nu-

cleon quark distributions inferred from lepton pair production were indeed determined to be compatible with the ones obtained from electromagnetic and weak inelastic scattering experiments.<sup>9,10,17</sup>

### 2.3 Scale invariance

In equation (2.7) we can write  $x_1$  and  $x_2$  in terms of  $x_F$ ,  $M^2$ , and  $\tau$ , obtaining an equation of the form:

$$\frac{d^2\sigma}{dM^2 dx_F} = \frac{4\pi\alpha^2}{9M^4} \frac{1-\tau}{x_1+x_2} \sum_q e_q^2 x_1 x_2 \left( f_1^q(x_1) f_2^{\bar{q}}(x_2) + f_1^{\bar{q}}(x_1) f_2^q(x_2) \right) \quad (2.9)$$

or simply

$$M^3 \frac{d^2\sigma}{dM dx_F} = f(\tau, x_F). \quad (2.10)$$

The right side contains the information about the structure functions, and depends only on scale invariant quantities. This equation reflects asymptotic freedom, and it is experimentally verified to 10 % accuracy.<sup>11,12</sup> The new generation of lepton pair production experiments are expected to improve this sensitivity. We shall see in the next chapter how parton dynamics modify this picture.

### 2.4 Transverse momentum and quark mass

So far, we have always neglected the transverse momentum and the mass of quarks and gluons. The latter are the sources of the hadronic masses, and are therefore expected to be of the order of a fraction of a GeV. The **intrinsic transverse momentum** of the quarks and gluons might be

$$k_T \sim \frac{1}{\text{size of the hadron}} \sim \text{few hundred MeV}/c.$$

These effects can be ignored as long as the longitudinal momenta of the partons are large, that is for  $x_i > m/\sqrt{s}$ , where  $m$  is the proton

mass. This condition is more readily satisfied at large values of  $M_{l+l-}$ , noting the relation  $M^2 = x_1 x_2 s$ .

In the naïve Drell-Yan model the transverse momentum of the dimuon pair comes directly from the intrinsic transverse momentum of the partons. In the next approximation we could modify the quark density functions by introducing explicit dependence on the quark transverse momentum  $\vec{k}_T^i$ , and on the total transverse momentum of the pair as given by  $\vec{P}_T = \vec{k}_T^1 + \vec{k}_T^2$ .

## 2.5 Angular distribution

Additional information can be obtained from the angular distribution of the lepton pair in the rest frame of the virtual photon. It is natural to measure this angular distribution with respect to the axis defined by the direction of the annihilating quarks. If all the transverse momenta could be neglected, this axis would lie along the directions of the colliding hadrons. In practice an axis must be chosen based on the directions of the initial hadrons which only approximates the desired quark-antiquark axis. The angular uncertainty in the direction of the annihilation axis will be about  $P_T/M$ .

However, given any choice of axes in the virtual photon rest frame the angular distribution can be parametrized by the following expression involving four functions  $W_i$ :

$$\frac{d\sigma}{d\Omega} = W_T(1 + \cos^2 \theta) + W_L \sin^2 \theta + W_\Delta \sin 2\theta \cos \phi + W_{\Delta\Delta} \sin^2 \theta \cos 2\phi. \quad (2.11)$$

Functions  $W_T$  and  $W_L$  correspond to transverse and to longitudinal polarization of the virtual photon. § In the parton model the anni-

§ The case  $J_z = \pm 1$  is commonly said to correspond to **transverse polarization**, and  $J_z = 0$  to **longitudinal polarization**, where  $\vec{J}$  is the total angular momentum.

hilating quarks are on-mass-shell and their mass is neglected so that helicity is conserved at the electromagnetic vertex. Hence annihilation to a transverse photon is expected to dominate, while the other terms can contribute due to the imprecision as to the annihilation axis. We may expect that  $W_\Delta$  is of order of  $P_T/M$ , and  $W_L, W_{\Delta\Delta}$  are of order  $P_T^2/M^2$ . This prediction has been confirmed by experiment:<sup>12-16</sup> the bulk of the lepton pair distribution is well described by  $1 + \lambda \cos^2 \theta$  with  $\lambda \simeq 1$ , after the integral over  $\phi$  is performed.

## 2.6 Other predictions

Among the other features of lepton pair production successfully described by the Drell-Yan model, I shall mention one concerning the comparison of the yield using  $\pi^+$  and  $\pi^-$  beams. The annihilation involves a quark from the target nucleon and an anti-quark from the projectile, and at large  $\tau$  the yield turns out to be four times larger with negative pions,<sup>13,17</sup> in agreement with the charge assignment of the quark model.

The incoherent nature of parton scattering has been confirmed by the observation that in scattering off nuclei the cross section varies with the atomic number  $A$  such that  $\sigma_A = \sigma_0 A^1$ .<sup>18</sup> This lack of ‘shadowing’ is consistent with the idea that the quarks act as free particles during the Drell-Yan process.

On the other hand, some features of dilepton production in hadronic scattering have not been explained in the naïve model. First of all, the observed dimuon yield appears to be larger than that predicted by equations (2.7) or (2.9) by a factor in the range 2-2.5,<sup>10-12,15-17,19</sup> if quark densities are normalized according by the quark counting rules, which are found to be satisfied in deep inelastic electron and muon scattering.

Furthermore, the transverse momentum distributions appear to

extend to values larger than those expected for intrinsic  $\vec{k}_T$  distributions, and also exhibit dependence on  $M$  and  $\sqrt{s}$ .<sup>11,12,20</sup>

Some indications were also found that in the region of  $x_F$  close to 1 the angular distribution of the pair departs from the form expected for transversely polarized virtual photons.<sup>21</sup>

In the next chapter we shall briefly review how QCD affects the simple picture that we have examined. We shall recall the way the theory introduces a smooth scale breaking, and how sensitive experimental observations can reveal information about subnuclear dynamics by looking in more detail at the various aspects of dimuon production in hadronic collisions.

## Chapter 3

### QCD AND LEPTON PAIR PRODUCTION

#### 3.1 Overview of the chapter

The picture of lepton pair production presented in the previous chapter is corrected in various ways when the effects of strong interactions are considered more closely. We shall briefly review some of these aspects, trying to preserve the intuitive viewpoint provided by the Drell-Yan model without entering into complex formalism.<sup>8</sup>

The topics of scale breaking, leading-log formalism, and higher order corrections will be presented, and some consideration will be given also to effects involving the transverse momentum and anomalous spin alignment at large  $x_F$ .

#### 3.2 Scale dependence of the quark density functions

The scale dependent effects introduced by QCD<sup>3</sup> can be described in the language of the parton model.<sup>21</sup> A parton with longitudinal momentum fraction  $x$  has a large probability to emit a gluon of momentum fraction  $y$ , which it may later reabsorb. On a short time scale the original parton is effectively represented by a parton of momentum fraction  $x - y < x$ , plus a gluon. In the previous chapters we have discussed how the study of small scale systems requires a high energy probe. In the case of the Drell-Yan process the square of the invariant

mass of the lepton pair is the parameter that determines our sensitivity, and the ability to resolve a parton into two partons with smaller momenta is increased at larger values of  $M^2$ . Therefore the effective quark densities measured in an experiment are  $M^2$  dependent, and we must parametrize them as  $f(x, M^2)$ . For higher values of  $M^2$  the probability of finding a quark decreases at large  $x$  and increases at small  $x$ .

However, the strong coupling constant of QCD grows weaker with energy, according to the concept of asymptotic freedom. Hence the tendency for a parton to disassociate into lower momentum partons decreases with energy. This slows the rate of change of the observed quark density functions to a logarithmic dependence on  $M^2$ . Thus the scale independent relation (2.10) serves as a good first approximation, and only very sensitive experiments can detect the predicted scaling violations.

### 3.3 Higher order diagrams and leading-log approximation

In the model that we have described so far, the production of lepton pairs occurs through a quark-antiquark annihilation. The picture becomes more complex if we consider higher order corrections predicted by QCD. Figure 3.1 shows some of the Feynman diagrams relevant to the lowest perturbative orders.

Notice that contributions to lepton pair production come from all types of parton-parton collisions: quark-antiquark, quark-gluon, antiquark-gluon, and gluon-gluon. Nevertheless, it has been proven that in the perturbative QCD framework the process can still be expressed in terms of effective quark densities. In fact, at any perturbative order the differential cross section can be written in terms of a

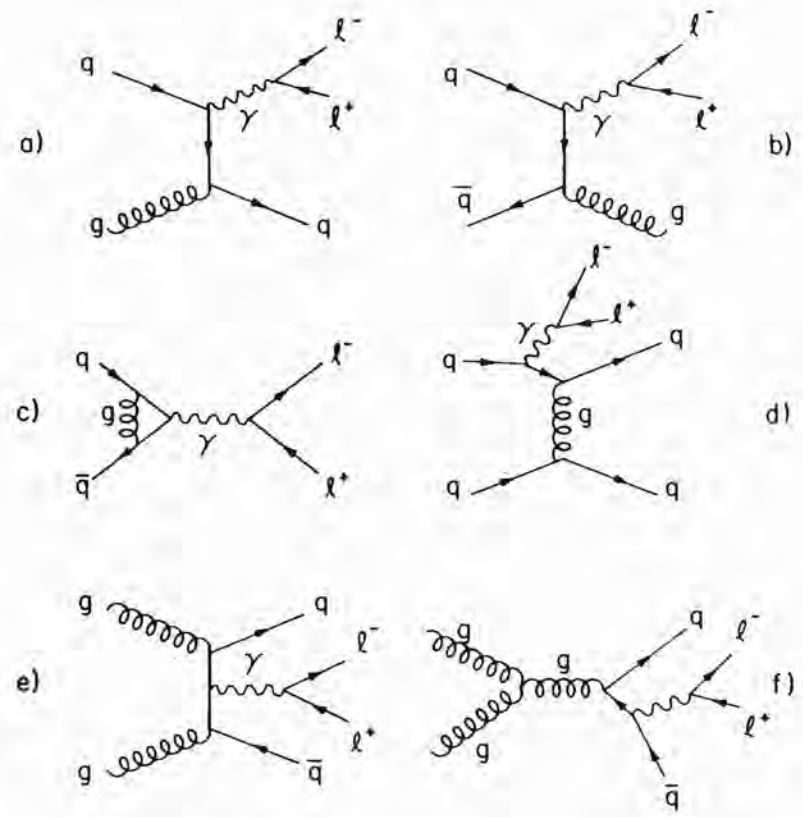


Fig. 3.1 Some higher order QCD subprocesses contributing to massive lepton pair production.

power series in  $\ln(M^2)$  :<sup>22</sup>

$$M^2 \left( \frac{d^2\sigma}{d\tau dx_F} \right)_n = \alpha_s^n \left( a_n \ln^n(M^2) + b_n \ln^{n-1}(M^2) + \dots \right) \quad (3.1)$$

where  $\alpha_s^n$  is strong coupling constant evaluated at order  $n$ , and the coefficients  $a_n$ ,  $b_n$  depend on  $\tau$  and  $x_F$  and contain the information about the quark densities of the two colliding hadrons. In the **leading-log approximation** only the term with the largest power in  $\ln(M^2)$  is retained. In that case, it was shown that substituting the explicit expression for  $a_n$  we obtain an expression similar to equation (2.9), with the modification that now the quark densities become mass dependent in the way discussed in the previous section:

$$f^q = f_n^q(x, \ln(M^2/\Lambda^2)) \quad (3.2)$$

where  $\Lambda$  is the scale parameter of QCD, and  $n$  indicates that the quark densities must be evaluated at the  $n^{\text{th}}$  perturbative order. Therefore QCD is expected to satisfy the factorization hypothesis at any order to good accuracy.

Furthermore, it was proven that the same leading-log corrections apply to the different cases of lepton pair production and deep inelastic scattering, so that the strong factorization hypothesis is also preserved.<sup>22</sup> Observe that the sign of  $Q^2$  is opposite in the cases of lepton pair production and deep inelastic scattering. The structure functions depend only on the absolute value of  $Q^2$  or  $M^2$  in the leading-log approximation, so results from the two classes of experiments may be directly compared.

It is interesting to consider the question as to what kind of higher order diagrams are summed together in the leading-log analysis. The answer is that this approximation collects the effects of collinear radiation of gluons. A massless, on-shell particle can couple to a system

of massless collinear particles, which are still on-mass-shell, therefore generating a logarithmic divergence in the amplitude. In QCD this divergence leads to the appearance in the formula of the scale parameter  $\Lambda$ . It turns out that among all the logarithmic terms, the ones due to collinear gluon radiation exhibit the largest scale dependence at any perturbative order.

Knowing the significance of computing only the leading-log terms, we can guess in which regions the approximation is more likely to fail. For instance, it will still be unable to produce transverse momentum  $\vec{P}_T$  of magnitude larger than the intrinsic  $\vec{k}_T^i$ .<sup>24</sup> Large values of transverse momentum are presumably generated in diagrams of the kind in Figure 3.1a, b, where the radiation of a stiff, transverse gluon or quark is required. We expect that in this case the leading-log approximation is not valid any more, and the effective Drell-Yan structure functions at large  $\vec{P}_T$  may be different from those measured in deep inelastic scattering.†

### 3.4 The K-factor and complete higher order computations

Another important departure from the leading-log approximation concerns the magnitude of the cross section. Experimentally, the cross sections for production of electron and muon pairs have been measured with different beam particles and energy, and there is a general agreement that the yield is about 2–2.5 larger than that predicted by equations (2.7) and (2.9).<sup>10–12,15–17,19</sup> This ratio is normally known as the **K-factor**.

† Another way to describe this situation is to observe that  $\vec{P}_T^2$  represents a new (mass)<sup>2</sup> scale, together with  $Q^2 = M^2$  and  $\Lambda^2$ , and so the computation is more complex than in the standard case, where only the ratio  $M^2/\Lambda^2$  is involved.

The leading-log approximation is not able to explain this effect, since the mass-dependent structure functions are normalized according to counting rules, in the same way as the naïve parton densities.

Some attempts have been made to improve the QCD prediction by including a larger number of Feynman diagrams. Today we know the result of the perturbative calculation at the first order beyond the leading-log, which consists in computing the amplitudes for the three diagrams in Figures 2.1 and 3.1.a,b, using mass dependent quark densities. Despite the fact that the correction is of order  $\alpha_s(M^2) \simeq (12\pi)/(25 \ln(M^2/\Lambda^2)) \approx 0.25$ , adding these two diagrams changes the overall cross section by a factor 1.8–2, in reasonable agreement with experiments.<sup>8</sup> Clearly, the reliability of the result is limited by the fact that this estimate could be substantially modified by calculations at higher perturbative orders.

Furthermore, in general the K-factor is expected to depend on  $\tau$  and  $x_F$ .<sup>25</sup> The first order calculation suggests that the bulk of the production takes place in a region where K is approximately constant, but departures are expected at large values of  $\tau$  and  $x_F$ , where the yield should grow.‡

### 3.5 Transverse momentum

QCD has also been used to compute the  $\vec{P}_T$  spectrum.<sup>24</sup> The problem here is the difficulty in dealing with both small and large transverse momenta, for which different physical processes are expected to dominate. Experiments<sup>11,12,20</sup> have shown that the average transverse momentum is generally larger than what is expected

‡ Another topic investigated in higher order QCD computations is the effect of gluon exchange between annihilating and spectator quarks. It has been argued that these diagrams might break the factorization hypothesis.<sup>8</sup>

for the intrinsic components  $\vec{k}_T^i$ . Moreover the average transverse momentum grows with  $M^2$  for fixed  $s$ , with some saturation at large masses, and grows with  $s$  at fixed  $M^2$ . This latter dependence is not easily explained in a free parton model, and it is normally considered as a clear indication of parton dynamics.

I shall not discuss further the subject of the large transverse momentum, despite the interesting theoretical work recently done in this field, but I shall consider the dependence of the transverse momentum on  $x_F$ .

The observed rise of the transverse momentum with the invariant mass of the lepton pair seems to suggest, in the context of the Drell-Yan model, a rise of the intrinsic  $\vec{k}_T$  with the Feynman variable  $x_i$  of each of the colliding hadrons. This happens simply because  $M^2 = x_1 x_2 s$ . A direct computation of the intrinsic  $\vec{k}_T$  distribution cannot be obtained with perturbative techniques as  $\vec{k}_T$  is related to the question of quark confinement. However, some predictions were based on rather general grounds.<sup>26</sup> One approach was to infer a plausible shape for the parton wave function, and to compute the  $x$  dependence of the intrinsic transverse momentum distribution noting that a parton at large  $x$  must be off-mass-shell in order to allow the spectator partons to decay into a massive final state system. Applied to lepton pair production, this leads to a rise of  $\vec{P}_T^2$  with both  $M^2$  and  $x_F$ .

Computations based on perturbative QCD<sup>24</sup> lead instead to the prediction that, at least for large  $x$ , the average transverse momentum must decrease linearly as  $(1-x)$ , a trend which should be reproduced in lepton pair production in the region of large  $x_F$ .

### 3.6 Angular distribution

A different class of higher order diagrams has been considered

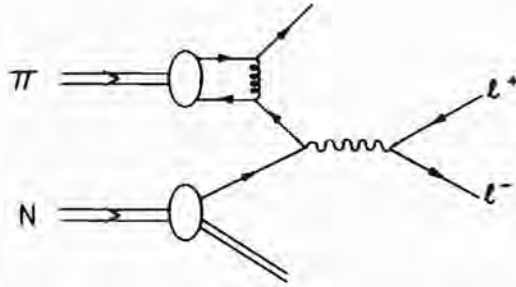


Fig. 3.2 Higher twist contribution to lepton pair production at large  $x_F$  in pion-nucleon interactions.

in which bound state effects are computed directly. An interesting prediction was made for pion-nucleon interactions at large  $x_F$  (Figure 3.2).<sup>27</sup>

In this region the effect of extracting a quark from a pion introduces a term proportional to  $1/M^2$ . This term, called the **higher twist** term, is characterized by a different spin alignment of the virtual photon. This is experimentally accessible by studying the lepton pair angular distribution in the rest frame of the virtual photon. While in the bulk of the production the spin alignment of the photon corresponds to transverse polarization, this higher twist term predicts a complete longitudinal polarization in the limit of  $x_F \rightarrow 1$ , or  $x_1 \rightarrow 1$ , for pion-nucleon scattering. No such effect is expected in the case of proton-proton scattering. The cross section can be written accordingly in the following way:

$$M^3 \frac{d^3\sigma}{dM dx_1 d\Omega} \propto (1-x_1)^2 (1 + \cos^2\theta) + \frac{4\langle K_T^2 \rangle}{9M^2} \sin^2\theta + \frac{2\sqrt{\langle K_T^2 \rangle}}{3M} (1-x_1) \sin 2\theta \cos^2\phi \quad (3.3)$$

with  $\langle K_T^2 \rangle \approx (1 \text{ GeV}/c^2)^2$ .

Notice the introduction of a scale parameter  $\langle K_T^2 \rangle$ , which is determined by the pion wave function, and represents the average transverse momentum of the annihilating anti-quark. The scale dependence of the terms containing  $\langle K_T^2 \rangle$  is expected to be larger than that predicted by the leading twist annihilation diagrams (Figures 2.1 and 3.1). Despite the technical difficulty in measuring an effect of very small size compared the total Drell-Yan cross section, this prediction is very interesting because it can be investigated in studies of both the pion structure function, and the angular distribution. Additionally, experimental study at two values of  $s$  and  $M^2$ , but at the same value of  $\tau = M^2/s$ , can reveal further evidence for the scaling violation.

The transition from transverse to longitudinal virtual photon polarization at large  $x_F$  was experimentally observed in a muon pair production experiment with about 2000 events above  $M=4 \text{ GeV}/c^2$  and  $x_F=0.2$ .<sup>21</sup> The observation was not confirmed by a second experiment of comparable sensitivity for  $x_1 > 0.8$ ,<sup>16</sup> while very recently the transition to longitudinal polarization is favoured by new sets of data,<sup>28</sup> including those presented in this thesis.

We shall discuss these subjects further in following chapters. The study of forward produced high mass muon pairs is the topic of this thesis. New results concerning the pion structure function,  $x_F$  dependence of transverse momentum and angular distributions will also be discussed.

## Chapter 4

### EXPERIMENTAL PROGRAM AND DETECTOR GUIDELINES

#### 4.1 Experiment goals

Fifteen years have passed since the first study of the process  $pN \rightarrow \mu^+ \mu^- X$ ,<sup>5</sup> and physicists have become familiar with the Drell-Yan model, and with the interpretation of hard scattering phenomena in terms of quarks and gluons. Nevertheless, we have seen in the previous chapter that the study of lepton pairs produced in hadronic collision can still tell us much about the dynamics of the fundamental constituents, allowing us to test our knowledge of the strong interaction in greater detail.

The Fermilab Experiment 615<sup>29</sup> was proposed to study the production of high mass muon pairs in pion-nucleon interactions, with particular emphasis on the production at large  $x_F$  values. In this region QCD predicts logarithmic scaling violation, while stronger scale dependence and anomalous spin alignment are predicted by models incorporating higher twist effects. Furthermore, the experiment allows the direct measurement of the pion structure function over a wide range of  $x$ .

The experiment was approved for running at two different beam momenta, 80 and 250 GeV/c, and with both positive and negative

pion beams. Comparison between data collected at different beam energies but the same value of  $\tau = M^2/s$  allows precise measurement of scale dependence.

In particular, the validity of the scaling relation 2.10, corrected by the small scale dependence predicted by QCD (equations 3.1,3.2),<sup>3,23</sup> will be tested in the interval  $\sqrt{\tau} = 0.33-0.41$ . The lower limit is set by the presence of the charmonium states  $J/\Psi$ ,  $\Psi'$  in the data taken at 80 GeV/c, and the upper limit is fixed by the  $\Upsilon$  resonance produced with the higher beam momentum. As we shall see below, the detector has been designed to cover the region  $x_F \simeq 1$ , allowing us to test the prediction based on the higher twist QCD calculation discussed in Section 3.6.

The comparison of the yield obtained with positive and negative pions allows a test the electromagnetic nature of the process (Section 2.6).

This thesis deals with data obtained at the lower beam momentum, which was collected entirely with a beam of negative pions, in a period extending from December, 1983 to February, 1984. At the time of writing, results also are available for a test run at 260 GeV/c conducted in 1982, which will be described in separate reports. The data collected with  $\pi^-$  and  $\pi^+$  at 250 GeV/c, which took place between April, 1984 and July, 1984 is presently undergoing track reconstruction and event selection.

#### 4.2 Overview of the detector design

The cross section for production of lepton pairs by the Drell-Yan mechanism is very much smaller than the typical hadronic cross section because of the electromagnetic nature of the process. Several other effects also reduce the observed rate. The Drell-Yan process must be observed for lepton pair masses larger than  $4 \text{ GeV}/c^2$  to

avoid backgrounds from lower mass resonance decay. Equation (2.10) shows that  $d\sigma/dM$  is proportional to  $1/M^3$ , and further suppression is due to the shape of the structure functions, which causes the scale independent term to decrease steeply with increasing  $\tau$ . The result is that in  $\pi^-N$  collisions, with a center-of-mass energy in the range 10–20 GeV, the cross section for producing pairs at positive  $x_F$  with at least 4 GeV/ $c^2$  of invariant mass is of the order of 100 picobarns per nucleon, which is 8 orders of magnitude smaller than the pion absorption cross section. Large beam intensities are therefore required to investigate details of lepton pair production, especially if the emphasis is on the large  $x_F$  region, where the cross section decreases further.

The need for high intensity determined the choice of muon pairs as the final state to detect. Muons are able to penetrate thick layers of material, which allows a ‘beam dump’ experiment where non-interacting pions and secondary hadrons are absorbed before reaching the active part of the apparatus.

The interest in angular distributions was another concern in designing the detector. Reasonable acceptance is needed for pairs formed by muons with very different momenta, generally more difficult to detect. This requires good efficiency in the region where non-interacting beam particles would go, since that area will be populated by the more energetic member of an asymmetric pair at large  $x_F$ . This consideration ruled out the options of toroidal spectrometers or the use of a heavier absorber in the beam region.

It is useful for the Drell-Yan events to have an easily recognized topology in the detector. Then a trigger for the experiment can be devised which minimizes recording of background events

These requirements were met with a two-magnet design (Figure 4.1).

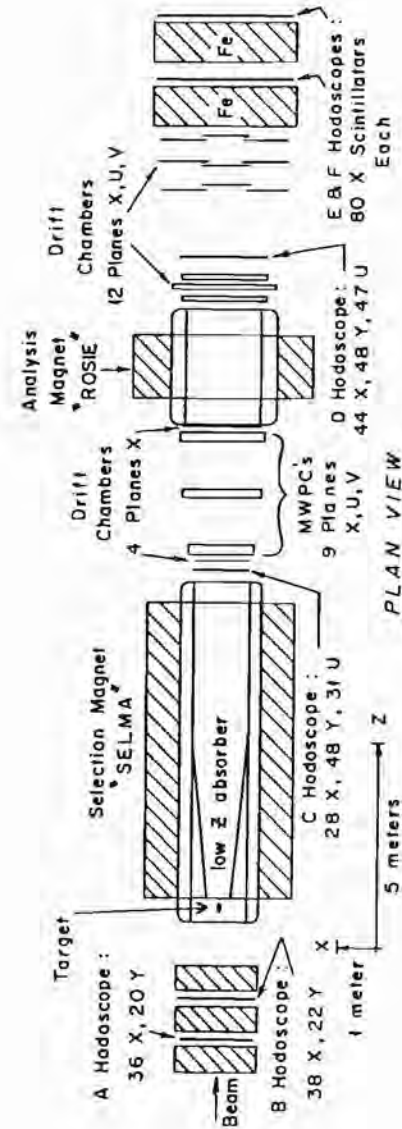


Fig. 4.1 E-615 detector layout.

The first magnet (**selection magnet**) is located close to the target, and contains the hadron absorber, which fills the gap between the magnet poles. The selection magnet had a 'kick' of 3.2 GeV/c, which bends the tracks of a high mass  $\mu^+\mu^-$  pair until they are nearly parallel, allowing a powerful trigger. It is followed by a **spectrometer magnet**, equipped with **wire chamber planes** in order to measure particle momenta.

With the aim of operating in a beam of about  $5 \times 10^8$  particles per second, the detector was equipped with a fast trigger based on **plastic scintillator counters**. A sophisticated **hardware trigger processor** was built to reject muon pairs with low invariant mass and pairs that did not originate in the target.

The various parts of the detector will be described in the following sections.

#### 4.3 Target

We used a cylindrical **tungsten target**, 8 inches long, corresponding to 1.7 inelastic interaction lengths for pions (Table I). The target was mounted immediately upstream of the beryllium absorber in the selection magnet (see next section), separated by a gap of only 2 cm.

The use of a heavy target optimizes the dimuon yield, since the Drell-Yan cross section in nuclei depends on the atomic number  $A$  as  $A^1$ ,<sup>18</sup> while the absorption cross sections grows as  $A^{0.76}$ .<sup>30</sup> Furthermore, a tungsten target is short for a given number of interaction lengths, which allows useful vertex constraints in event reconstruction and fitting (Section 7.8).

#### 4.4 Selection Magnet

The focussing magnet was a dipole of field integral 10.7 Tesla m,

**Table I** Target specifications:

TARGET	
Length	20.32 cm
Diameter	5.08 cm
Density	18.5 g/cm
Composition :	
	97.2 % (weight) W
	2.8 % Ni,Cu,Fe

corresponding to a momentum kick of 3.2 GeV/c. It was built by Fermilab for our experiment. The magnetic volume was 7.4 m long, 1.4 m wide, with height increasing from 14 cm to 65 cm in eleven steps, along the longitudinal direction ( $z$ -axis). A side view of the selection magnet is shown in Figure 4.2, and a top view in Figure 4.3.

The magnetic region was mapped using the Fermilab *ziptrack*, a system using three coils mounted on a moving cart. Field differences were measured by integrating induced currents and recording them on 12-bit encoders. The most upstream region of the magnet, not accessible to the ziptrack rail, was mapped with a hand-moved coil. The measurements showed that the transverse component of the field ( $x$ -axis) was everywhere smaller than 1 % of the main component of the field ( $y$ -axis). The integral along  $z$  of the transverse component was everywhere smaller than 0.1 % of the integral of the vertical component.

The selection-magnet was filled with the **hadron absorber**, consisting of 3.22 m of beryllium and 4.14 m of graphite. Additional 61 cm

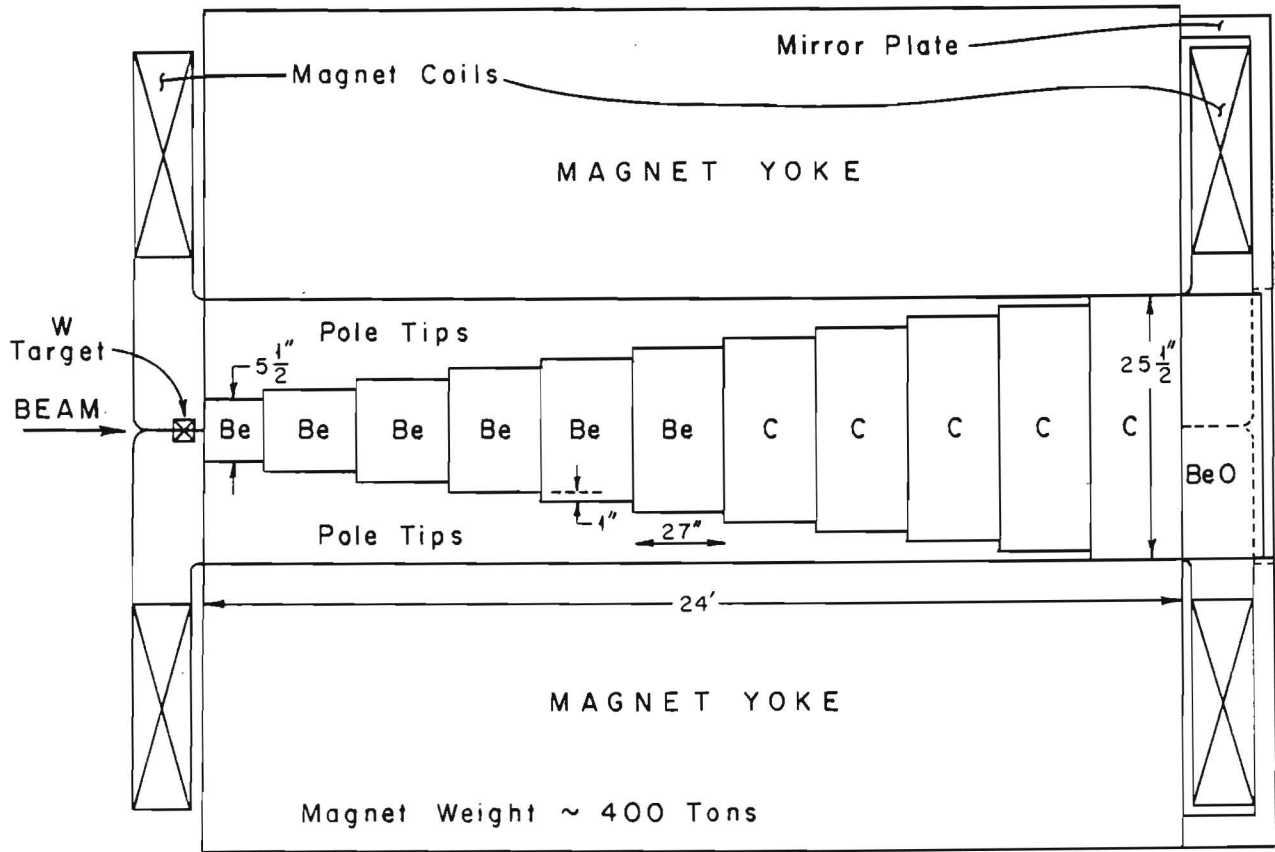


Fig. 4.2 Side view of the selection magnet.

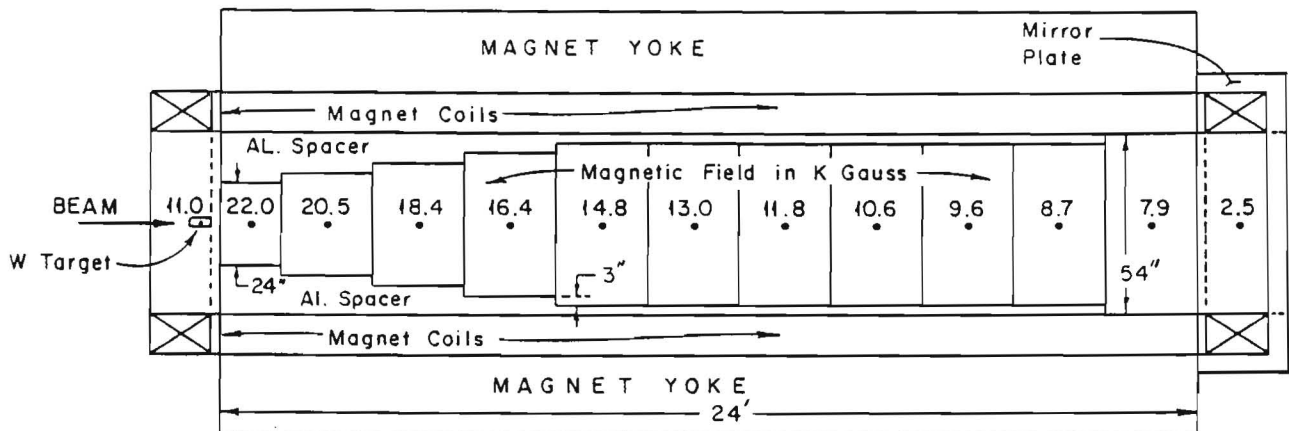


Fig. 4.3 Top view of the selection magnet.

of beryllium-oxide were located immediately downstream of the magnet. Altogether we had 14 absorption lengths for energetic pions, and 32 radiation lengths. The choice of low-Z materials was made to limit the amount of multiple scattering. This permitted good resolution in the initial track direction, and good rejection of muons not originating in the target. We shall discuss this topic in Chapter 7.

#### 4.5 Wire chambers

Nine planes of multi-wire-proportional chambers (MWPC) were located between the selection magnet and the spectrometer magnet. See Figures 4.1 and 4.4.

The planes were mounted in three modules, repeating the orientation scheme  $x-u-v$ , with the oblique planes at 15.5 degrees from the vertical direction. See Figure 4.5.

The planes were built with 25 micron anode wires, 2.1 mm apart, kept at zero voltage. The cathodes were aluminized mylar foils, operated at 3500 Volts. The voltage was ramped down between beam pulses in order to prevent the development of dark current. Each of the about 8000 anode wires was connected to a preamplifier mounted on the chamber itself, connected to the read-out modules through 500 nsec delay lines. The gas mixture was Argon-Isobutane-Methylal. The system worked well even at high intensities, where the average plane detection efficiency was 95%, with resolution of about .75 mm.

Sixteen planes of drift chambers (DC) completed the tracking system. Four planes with vertical wires were located upstream of the spectrometer magnet, where they were used to improve the tracking accuracy. Two groups of six planes measuring along  $x-x-v-u-x$  were located downstream of the spectrometer magnet. The most downstream six planes were mounted in 18 frames. See Figures 4.1, 4.4, and 4.5. The chambers were built and read out according to a

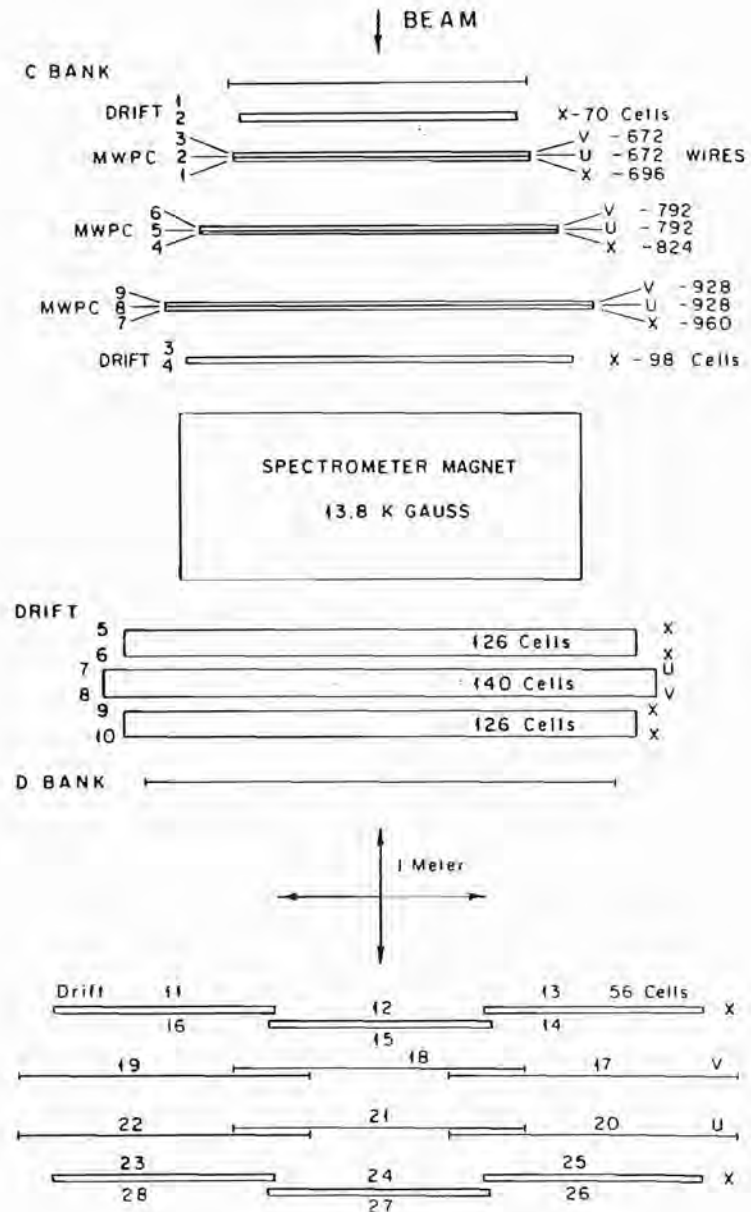


Fig. 4.4 Layout of the wire chambers; top view.

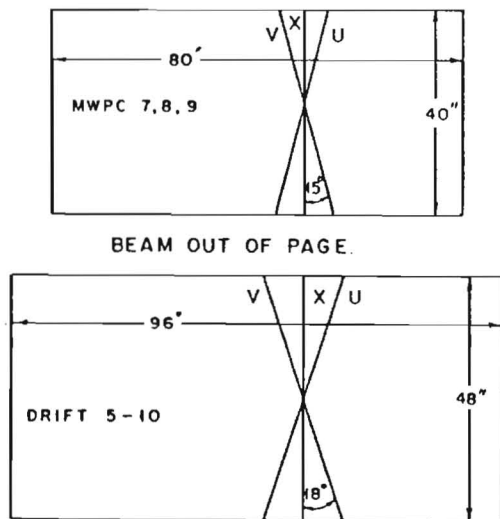


Fig. 4.5 Scheme of the inclination and denomination of the wire planes.

scheme used in a previous experiment.<sup>31</sup> The cells were 2 cm wide, with graded potentials on the cathode wires. We used a mixture of 70% Argon, 30% Isobutane, with all the Argon bubbling through Methylal at 10°C. The anode voltage was ramped with the accelerator cycle. The signal from each of the 2128 channels was discriminated in amplifiers mounted on the chamber frames, and transmitted to the digitizers through 300 foot ribbon cables. Groups of 8 channels were brought together on TDC modules, which were capable of recording up to four time intervals in any channel combination. The drift time was measured in 31 bins, each 8 nsec long.

The measured average position resolution at high intensity was 290  $\mu\text{m}$  in the drift chambers. The chamber alignments and time offsets were calculated on a day-by-day basis for each module. The time offsets were not measured for single channels, but were averaged

over groups of 56 wires. While it appears that a wire-by-wire calibration would have allowed us to reach about 200  $\mu\text{m}$  resolution, this would have not improved the system performance and overall resolution, which is dominated by the multiple scattering in the hadron absorber.

The average detection efficiency in the drift chambers at high intensity was 92%, reduced to 90% because of a limited number of channels which were not operational on any given day.

The use of MWPC's upstream of the spectrometer magnet and DC's downstream is a compromise between efficiency and resolution. The multi-wire chambers operated in the region of higher track rate and density, so their shorter sampling time (about 30 nanoseconds) resulted in smaller noise and faster track reconstruction. The disadvantage of their lower resolution was overcome with the four planes of upstream drift chambers.

#### 4.6 Spectrometer magnet

The second magnet used in the experiment was a wide aperture dipole of field integral 2.9 Tesla m (.86 GeV/c). The magnetic volume was 2.2 m long, 1.8 m wide, and .9 m high. The field was mapped with the ziptrack. The main component was vertical, and antiparallel to the field of the selection magnet. The field integral was found uniform over the cross section within 1% (Table II), with the component along the  $y$ -axis smaller than about 4 MeV/c.

#### 4.7 Scintillator banks

The detector was equipped with 6 banks of plastic scintillators, comprised of 14 planes.

The veto scintillators ( $A$  and  $B$  banks) were located upstream of the target (Figure 4.1). They covered a region of approximately 2

**Table II** Map of the field integral of the spectrometer magnet, on the  $x$ - $y$  plane.

FIELD INTEGRAL MAP OF THE SPECTROMETER MAGNET (GeV/c)					
	.846	.858	.860	.859	.846
Y ↓	.855	.856	.860	.857	.856
	.858	.858	.859	.859	.858
	.855	.860	.860	.856	.855
	.846	.858	.860	.859	.846
			X →		

$m^2$ , around the beam pipe, (which was 10 cm in diameter), and they were used to eliminate events associated with the muons outside the beam pipe. Both banks were formed by a plane of counters along  $x$  and a plane of counters along  $y$ . Iron absorbers separated the  $A$  and  $B$  banks, and the  $B$  bank from the target region.

The  $C$  bank was located immediately downstream of the selection magnet, and covered an area of 1.43 m along  $x$  and .59 m along  $y$ . It consisted of 28 vertical counters, 48 horizontal counters, each of them covering half of the aperture, and 31 oblique ( $u$ ) counters forming two planes (Figure 4.6).

The  $D$  bank was placed downstream of the spectrometer magnet, between the two groups of DC's. This bank was 2.23 m wide and 1.09 m high, and consisted of 44 full length vertical counters, 48 half length horizontal counters, and 47 oblique ones in two planes (Figure 4.7).

A 2 m thick iron wall was placed downstream of the drift chambers. This was designed to eliminate the non-penetrating particles

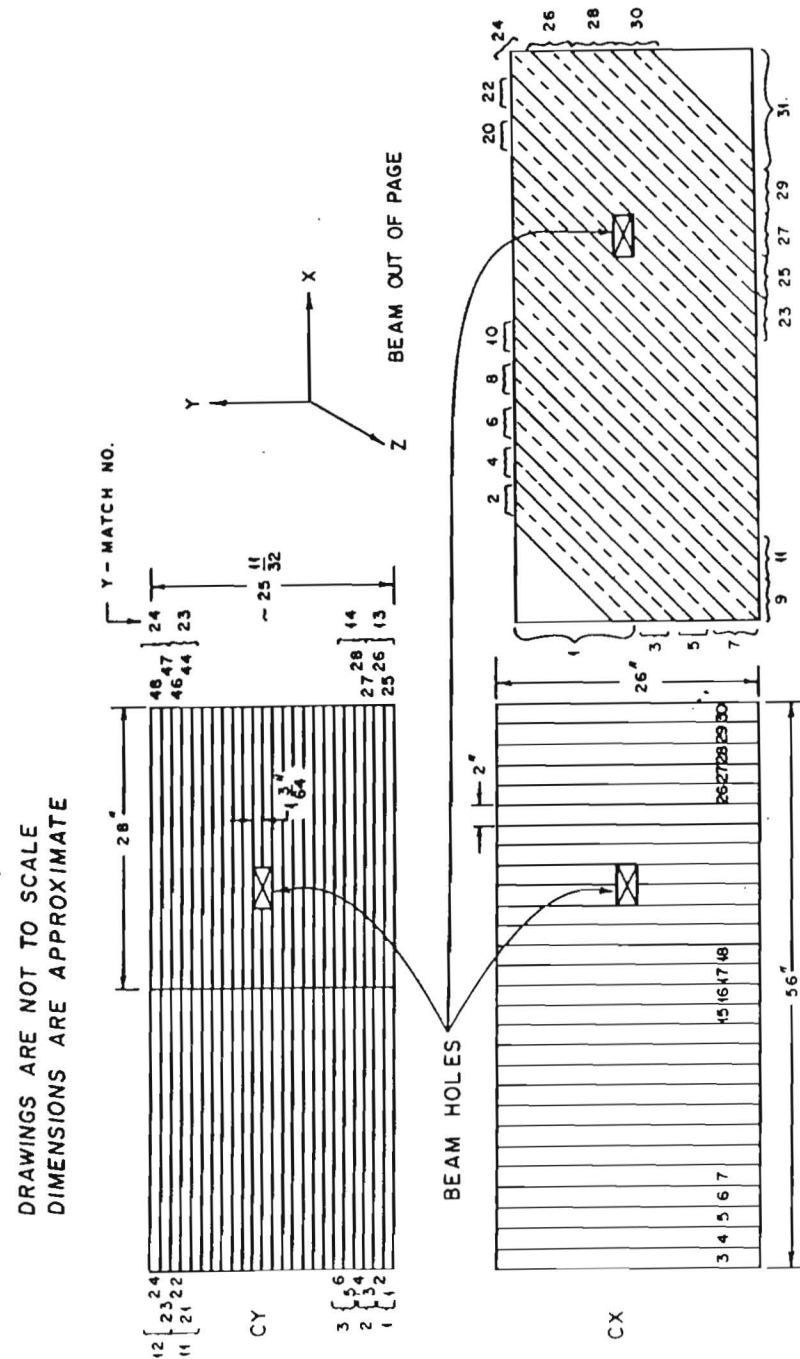


**Fig. 4.6** Arrangement of the  $C$  bank of scintillators.





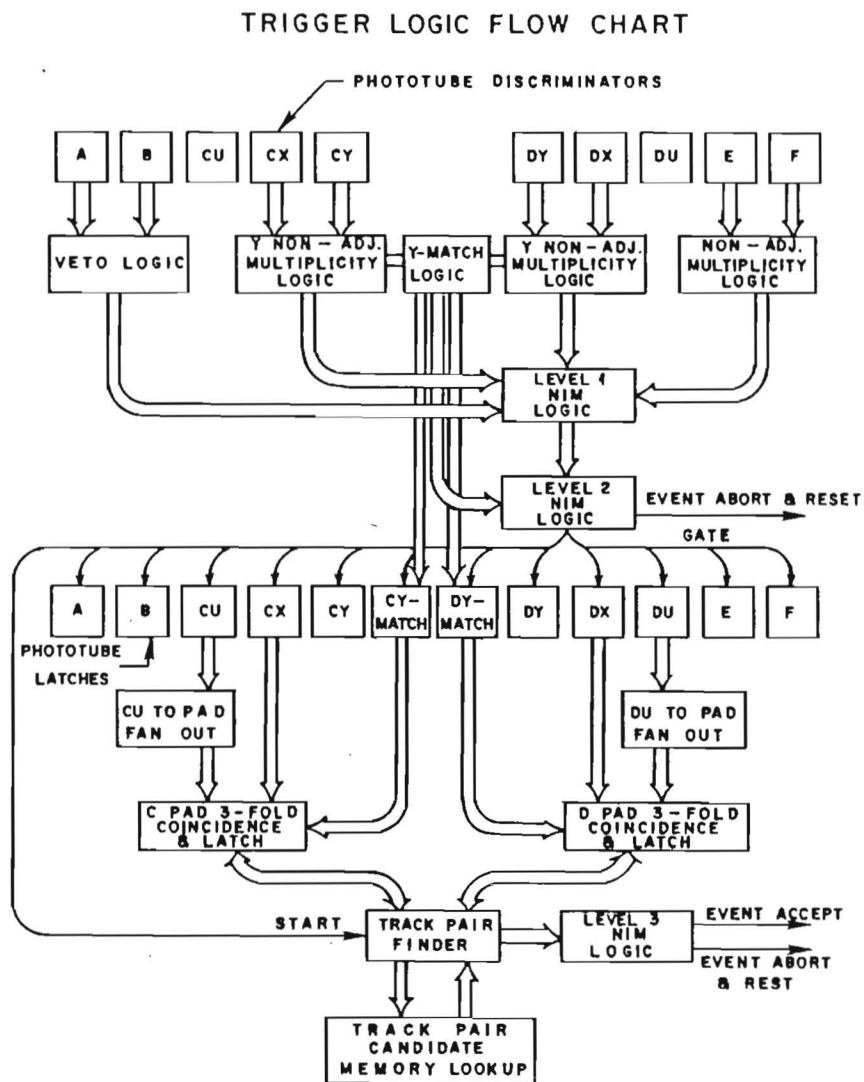


Fig. 5.1 Flow chart of the trigger logic.

pendently at this stage. A two particle pattern was required in each of the *C*, *D*, *E* and *F* banks. In order to reduce the chance of triggering on single particles accompanied by delta rays, at least two non-adjacent counters were required to fire in the *Cy*, *Dy*, *E* and *F* banks. The total number of logic channels was half the number of counters, because each half length counter was merged with the one on the other side. This information loss was recovered for the two upstream banks by requiring that each *y*-counter was overlapped by a struck *x*-counter.

In order to reduce the number of triggers due to muons from beam particle decays, a further requirement was devised for the *F* bank: at least one struck counter had to cover the region  $x < 0.36$  m. This allowed a large reduction of the number of triggers due to pairs of energetic negative muons, at a small cost in acceptance. The loss of high mass events is only 5%, while the gain in live time was about 50%.

The *A* and *B* counters were used in veto in the first level trigger. The veto requirement was a coincidence between any *x* or *y* counter in one bank, with a corresponding *x-y* coincidence in the other bank. To allow for small track inclinations, the counters in one bank were shifted by half of their width relative to the counters in the other bank. A match with either member of the corresponding pair was checked.

Further requirements were that the multiplicities of hits in the *Cy*, *Dy*, *E* and *F* banks each had to be less than eight. This was devised to eliminate noisy events, which probably would be analyzed incorrectly by the higher level triggers. The resulting loss of good events is estimated to be around 0.1% at high intensity.

The first level trigger rate was typically around 25000 triggers per beam spill, obtained with about  $3 \times 10^9$  incident pions in the 15

second spill. The Level-1 decision time was about 40 nsec.

### 5.3 Level-2 trigger

At this stage the information coming from the  $C_y$  and  $D_y$  counters was brought together to test the hypothesis that the track was generated in the target. For this purpose, the 48 counters forming each bank were paired twice to form 12 horizontal stripes. Each stripe was checked against two matching stripes in the other bank.

It only took about 10 nsec after the Level-1 to obtain the answer from Level-2. The number of accepted triggers was reduced by a factor of about 3.

### 5.4 Level-3 trigger

The third level compared the information from the  $C$  and  $D$  banks to analyze the track candidates in the magnetic bending plane.

All the scintillator signals were recorded in *scintillator latches* after a Level-1 trigger was issued. These modules could be read-out, as well as set, via CAMAC.

The latches also provided an output logic-level for each channel which was used in the subsequent Level-3 circuitry.

Each combination of an overlapping vertical ( $x$ ) counter and horizontal ( $y$ ) stripe made of 4 counters determined a rectangle (called a 'pad') which is overlapped by one oblique ( $u$ ) counter. Three-fold coincidences between the  $x$ ,  $y$  and  $u$  planes were formed and recorded in the *pad-latches*. A track candidate is made from one such rectangular pad in the  $C$  bank and one from the  $D$  bank. Figure 5.2 shows the scintillator information as organized into pads for a typical event.

Each pad latch module could be read-out or written into via CAMAC.

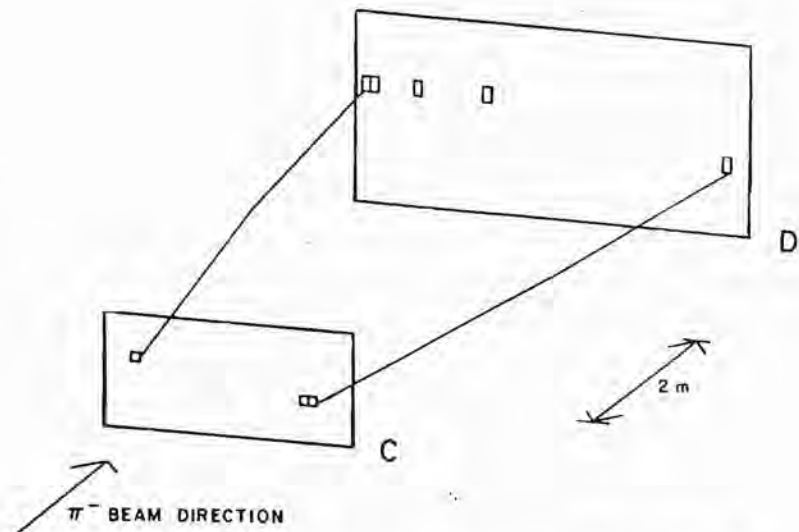


**Fig. 5.2** Illustration of the Level-3 trigger: within each bank, pads are determined by threefold coincidences between  $x$ ,  $y$  and  $u$  counters; track candidates are formed combining pads from the two banks.

After the pad coincidences had been stored in the latches, a hardware track finder looped through all the struck pads in the  $C$  bank, associating them with struck pads in the  $D$  bank with compatible vertical position. The process was done in parallel by two modules, looping through all the possible particle pairs.

Each track candidate was described by 15 bits, 5 of which specified the position in the  $Cx$  bank, 6 in the  $Dx$ , and 4 in the  $Cy$ . Assuming that the pattern represented a track generated in the target, the  $x$  information allowed measurement of the particle sign, momentum, and initial angle. It was therefore possible to reject the most common background of negative-negative pairs, associated with beam particle decays. The same algorithm allowed rejection of track candidates with anomalous or incompatible parameters. The actual

selection was made by comparing the 15 bits with the contents of programmable memory look-up modules built at Fermilab.

Combining the information on two track candidates we could have estimated all the parameters of the pair. However, the spirit of the look-up table method is to calculate in advance whether each possible pair is or is not a desirable trigger, and store that result as one bit. As we describe each track by 15 bits, the look-up table technique would require  $2^{30}$  bits of memory. This difficulty was overcome noticing that particular combinations of the available bits were strongly correlated with the invariant mass of the pair. This was mainly due to the bending imparted to the trajectories by the selection magnet, which was designed to give high mass pairs a readily identified topology.

The 30 bits of information about a track pair were reduced to 16 as follows. The  $Cx$  addresses of the two tracks were subtracted, reducing  $2 \times 5$  bits to 6 bits. The  $Dx$  addresses of 6 bits each were subtracted and truncated to 6 bits. And in parallel the  $Cy$  addresses were subtracted and only the absolute value kept, reducing 8 bits to 4. The resulting 16-bit pattern was compared with look-up tables loaded according to Montecarlo simulations, and uninteresting events were rejected. All of the subtractions were actually performed in other look-up tables to maximize speed.†

† This procedure resulted in very effective data collection with 250 GeV/c beam particles.<sup>32</sup> In that condition the detector acceptance extended down to about 1 GeV/c<sup>2</sup> in the invariant mass of the pair. The main source of background in the Level-2 trigger consisted of low mass dimuons, which were rejected with an efficiency of about 90%. Running with 80 GeV/c pions, the detector itself provided a natural cut-off below 3.0 GeV/c<sup>2</sup> pair mass, and the third level trigger was

We were able to evaluate the results of different trigger requirements by fully analyzing events recorded without the Level-3 trigger. At the time of the main data collection in 1983/1984 the chamber reconstruction programs had been fully developed and tested on the data collected in the 1982 test run. This enabled adjustments to be made to the Level-3 trigger on the basis of complete off-line analysis on a time scale of half a day.

The third level trigger required the two tracks to be vertically separated by at least two units. This was made necessary by spurious three-fold coincidences in adjacent vertical rows generated by tracks closely spaced in  $y$  but not  $x$ . This can happen because the  $u$  counters form two planes of overlapping counters, so that two of them are fired by each track. Since background triggers tended to have smaller vertical openings, the loss of acceptance was compensated in part by an increase in live time.

A further cut was applied on the track pair multiplicity, rejecting events having more than fifteen pair candidates in the Level-3 logic. The reason for this cut is that noisy triggers would eventually find their way through the third level trigger. We estimated that the related efficiency reduction was in the range 2-5 %, depending on the beam intensity. Figure 5.3 shows a typical distribution of the multiplicity of track pairs presented to the Level-3 logic.

The dead time introduced by processor was only about 2.5  $\mu$ sec per event. This is based on a processing time of 500 nsec per pair, and an average of 5 pair candidates per Level-2 trigger. Typically, one out of fifteen Level-2 triggers passed the third level, providing about

most effective in reducing the background due to negative-negative combinations associated with beam halo.

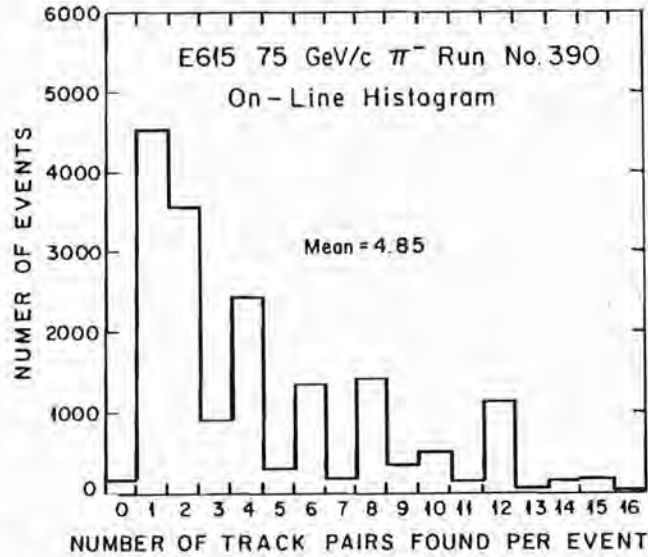


Fig. 5.3 On-line display of pair multiplicity in the trigger processor.

1200 triggers per beam spill of  $3 \times 10^9$  incident pions.

Further details about the trigger implementation can be found in reference 32. For completeness, we enclose various sketches of the circuitry developed at Princeton University.

Figure 5.4 sketches the implementation of the Level-1 trigger logic for the C or D banks in ECL circuitry.

Figure 5.5 shows details of the summing network which provided the signals for the non-adjacency hit logic in a given bank.

Figure 5.6 sketches the ECL circuitry for the scintillator latch modules.

Figure 5.7 shows the ECL circuitry for the pad latch modules.

Figure 5.8 shows a flow chart of the Level-3 track finder.

Figure 5.9 shows a flow chart of the memory look-up procedure.

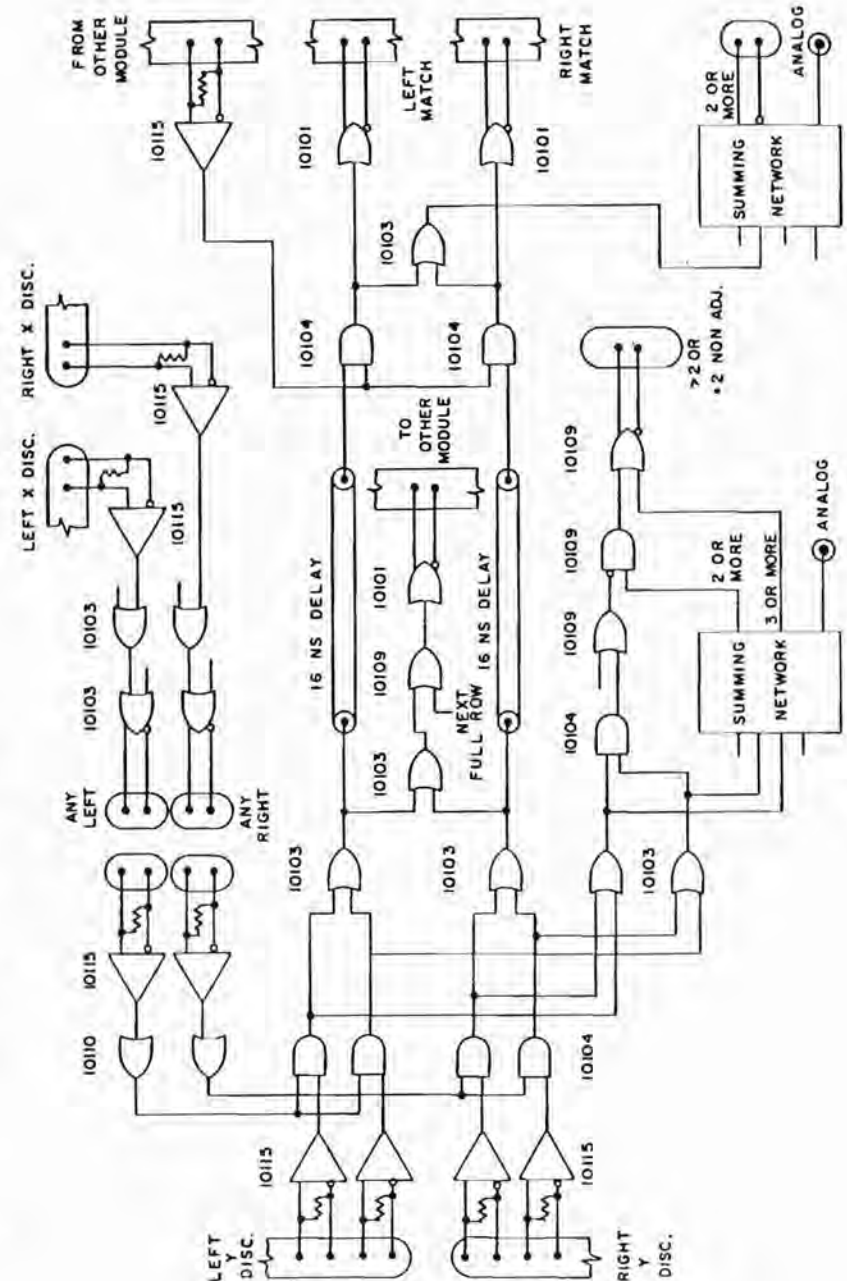


Fig. 5.4 Level-1 trigger logic scheme.

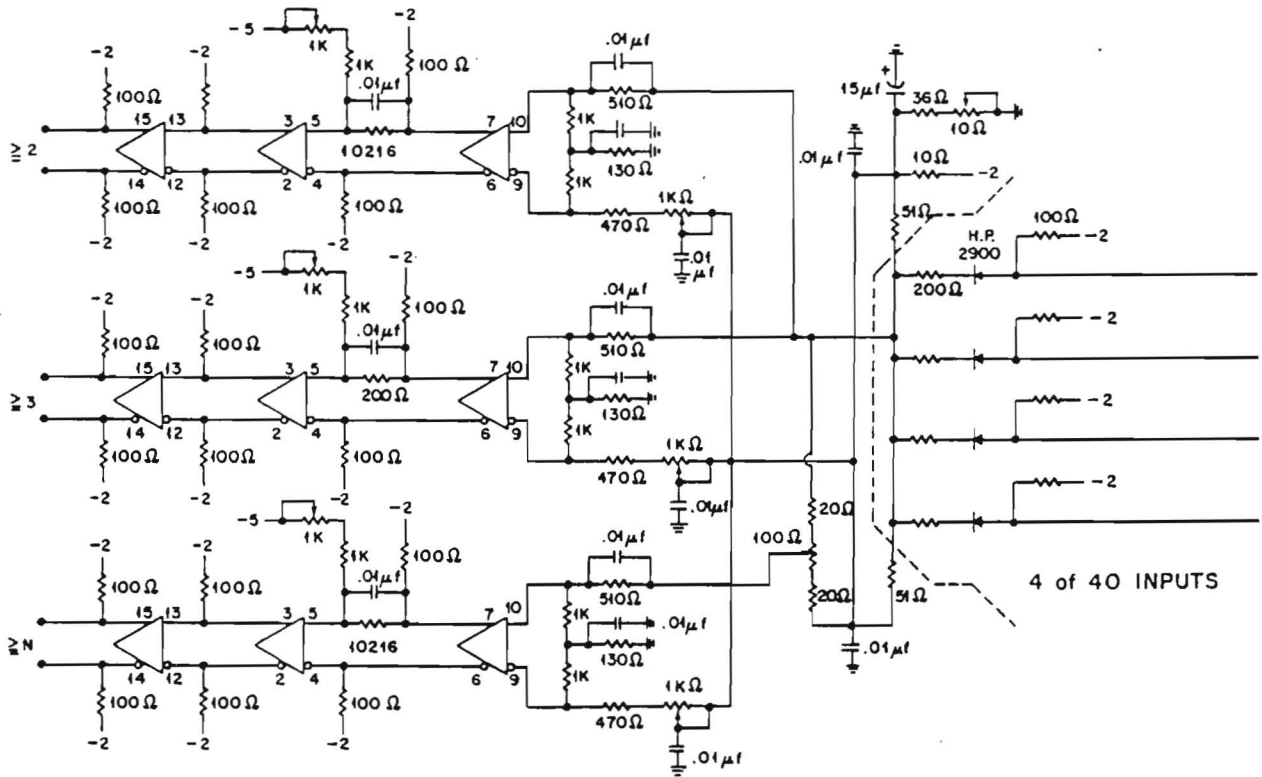


Fig. 5.5 Summing network for Level-1.

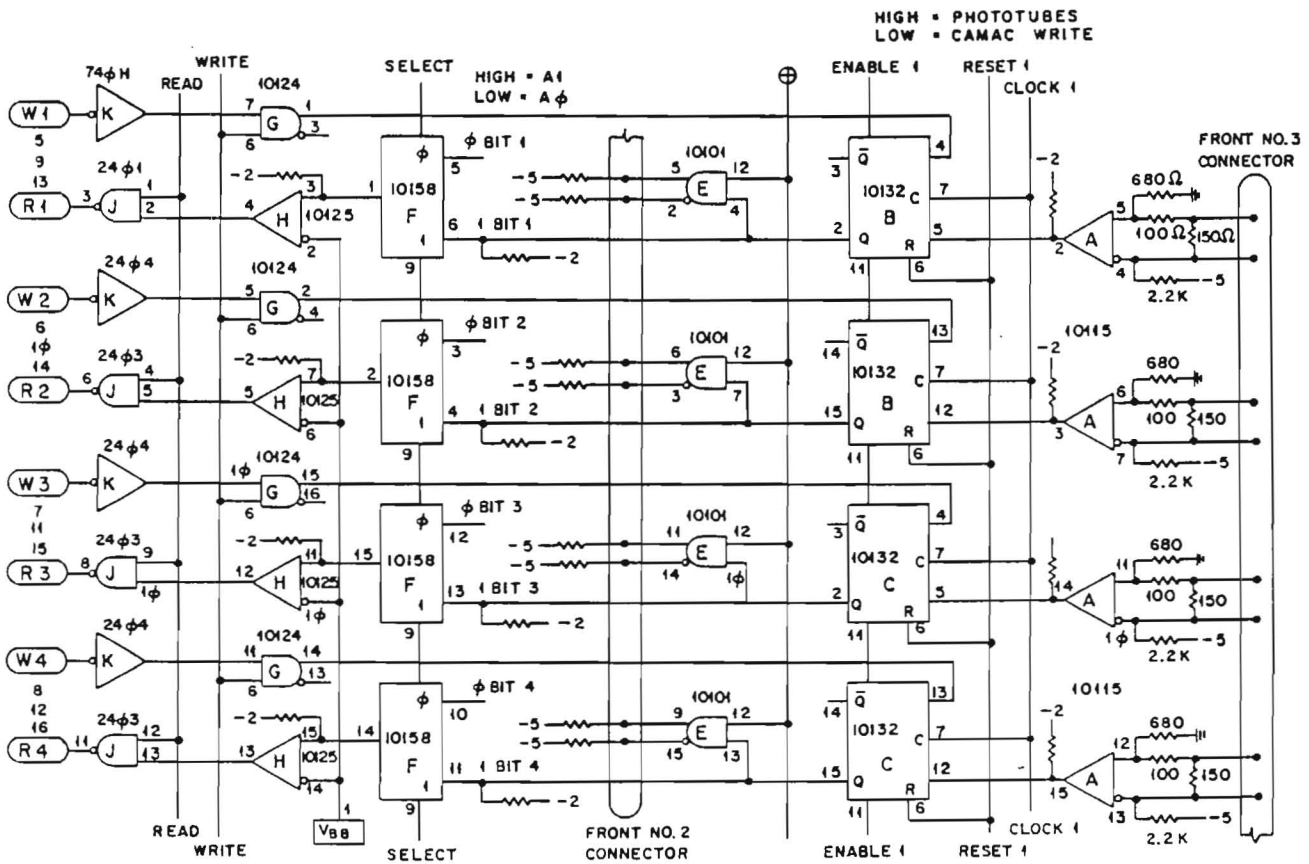


Fig. 5.6 ECL circuitry for the scintillator latch modules.

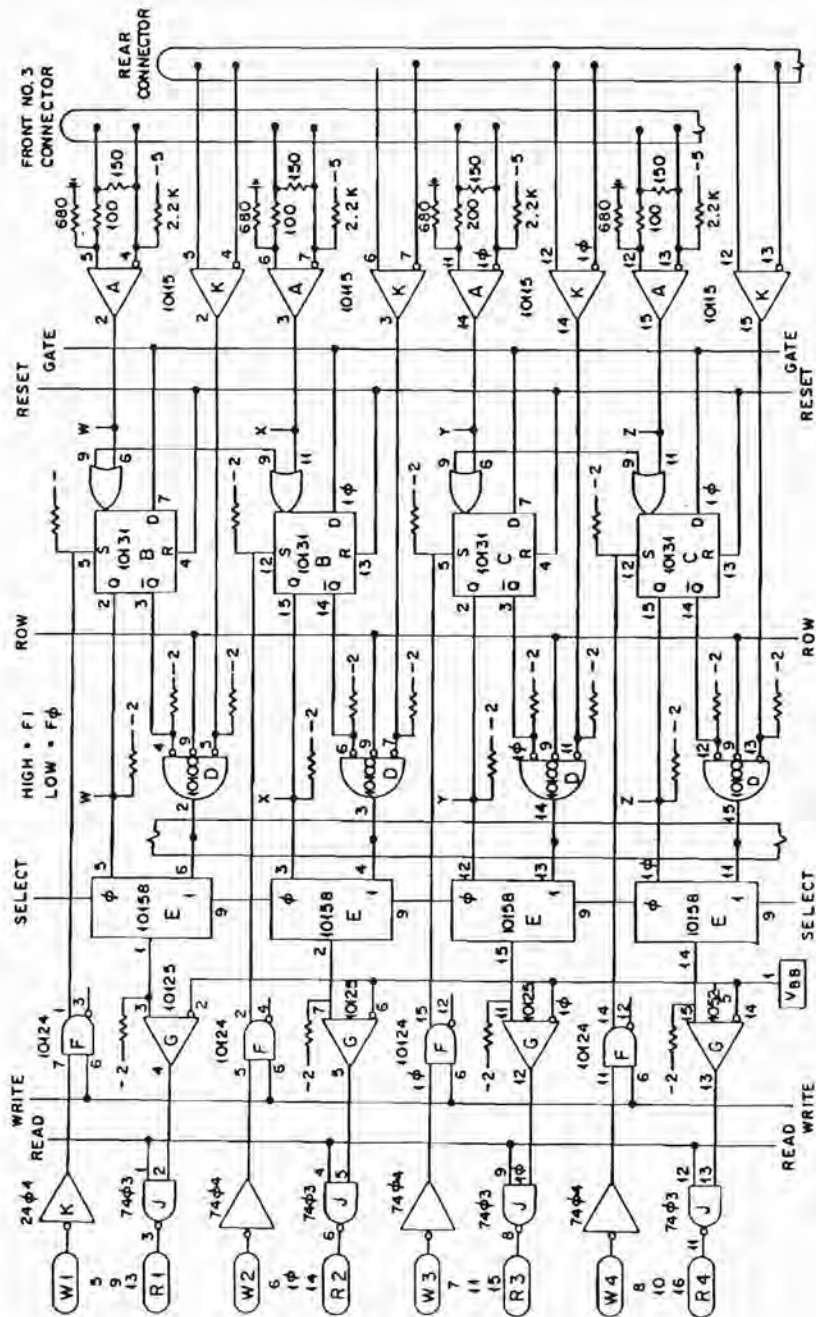
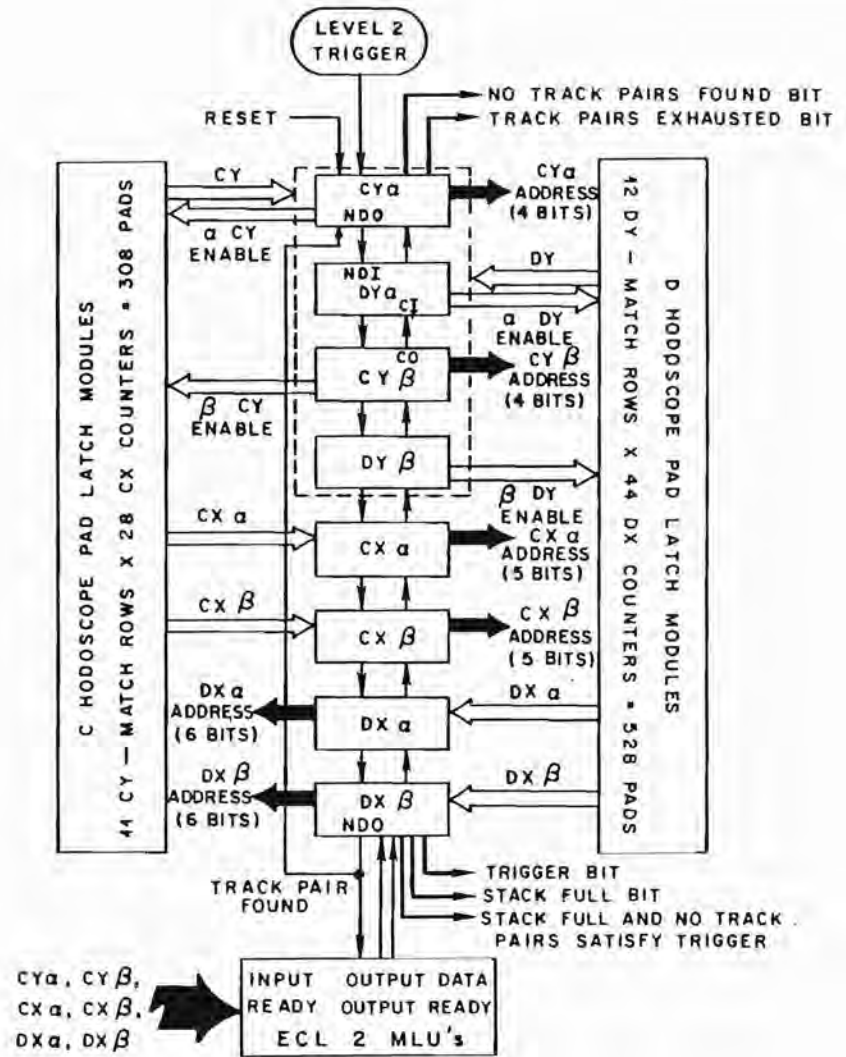


Fig. 5.7 ECL circuitry for the pad-latch modules.



TRACK FINDER & PAD LATCH FLOW CHART

Fig. 5.8 Flow chart of the Level-3 track finder.

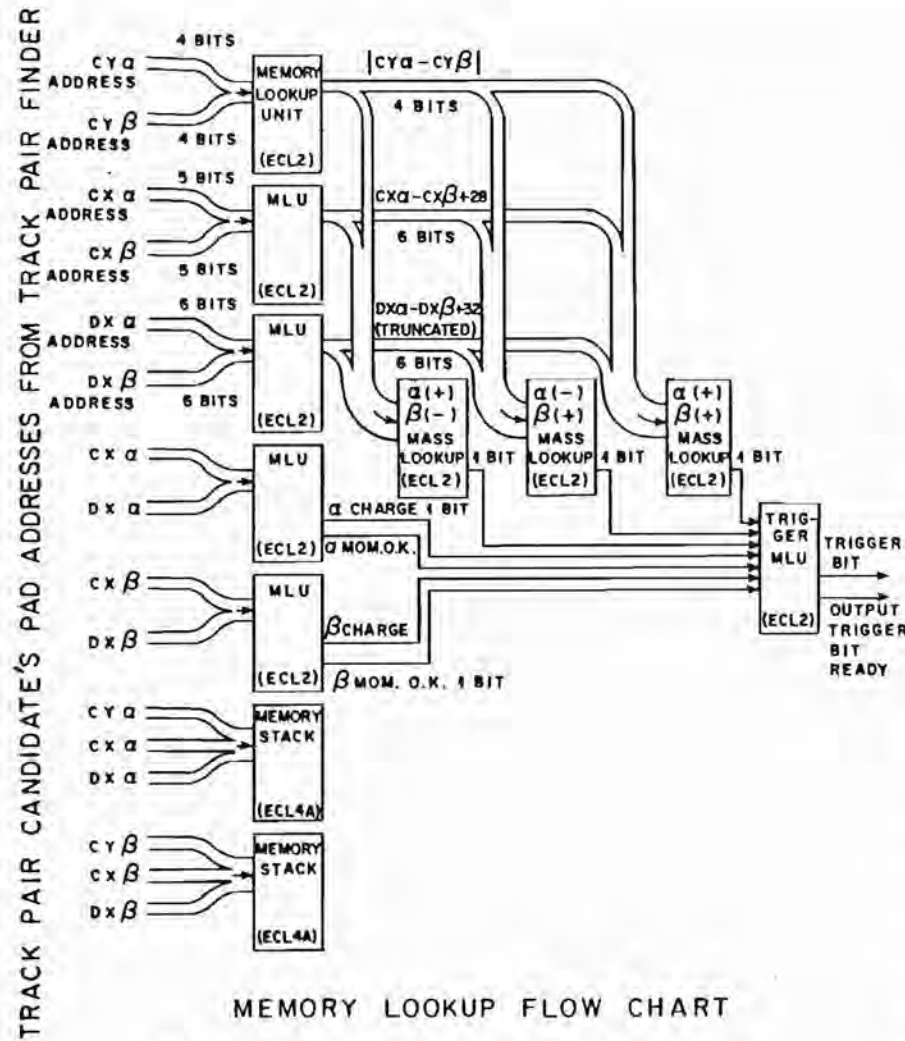


Fig. 5.9 Flow chart of the memory look-up procedure.

### 6.1 Beam line characteristics

The experiment was located in the High Intensity Lab in the Proton West Area at Fermilab, where we have been among the first users of the new superconducting accelerator.

During the period of data taking with 80 GeV pions, the machine accelerated protons to 400 GeV. The typical cycle time was about 50 seconds, with extraction time ('spill') of 10 or 15 seconds. In each spill about  $5 \times 10^{12}$  primary protons were delivered to a beryllium target in the Proton Area. See Figure 6.1.

The secondary beam was collected at  $0^\circ$ , and negative particles were selected by a dipole magnet and a collimator; the beam was then brought through a triplet of quadrupoles, and then bent into an adjustable horizontal collimator used for selecting the momentum range. The rest of the beam line consisted of a double focussing-defocussing station, horizontal bends to reduce the amount of muons from beam particle decays, and a final triplet for focussing on the experimental target. The resulting secondary intensity was  $3.6 \times 10^9$  particles per spill.

The size of the beam spot on the target was about 1.0 cm r.m.s. The collinearity between the beam direction and the laboratory z-

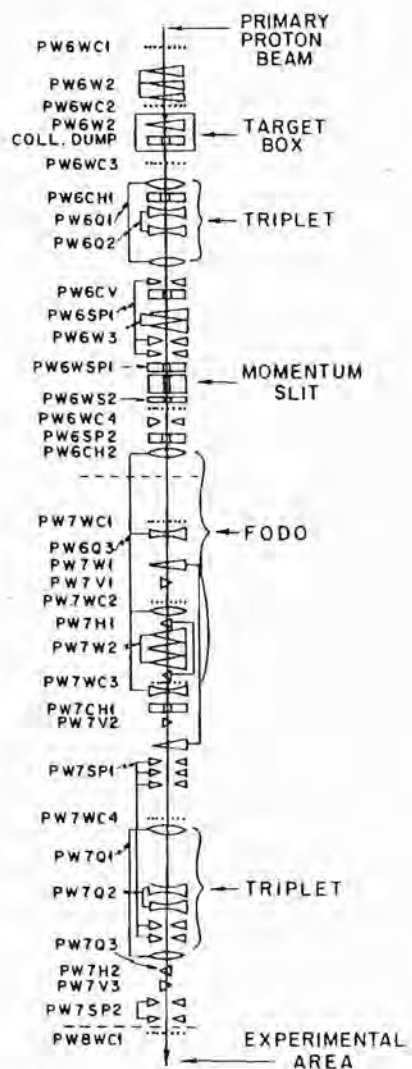


Fig. 6.1 Scheme of the secondary beam transport in the FNAL Proton-West area.

axis was verified by a study of the muons from  $J/\Psi$  decay, which measured the average beam direction to be  $0.0 \pm 0.1$  mrad in both horizontal and vertical planes. The beam traversed part of the fringe field of the selection magnet before reaching the target, so that the beam direction at the average interaction point was  $+1.0 \pm 0.1$  mrad in the  $x$ - $z$  plane.

## 6.2 Beam composition

The particle production by 400 GeV protons on beryllium targets has been measured at various secondary momenta.<sup>33</sup> Interpolating linearly between the values for 60 and 120 GeV/c we obtained the following percentages for negatively charged secondaries:

$$\pi^-: 74.3\%; \quad K^-: 6.1\%; \quad \bar{p}: 2.2\%; \quad e^-: 17.3\%.$$

We are interested in the hadronic composition of the beam, since electrons cannot produce any appreciable background. We have also to account for particle decays: the beam line was 597 m long, and 5.7% of the pions decayed, together with 35.2% of the kaons. The resulting hadronic composition of the beam at our target was:

$$\pi^-: 91.9\%; \quad K^-: 5.2\%; \quad \bar{p}: 2.9\%.$$

Kaons and anti-protons represent only a small contamination. In what follows, we shall speak of a *pion beam* and consider the contamination from other hadrons only when discussing sources of systematic errors.

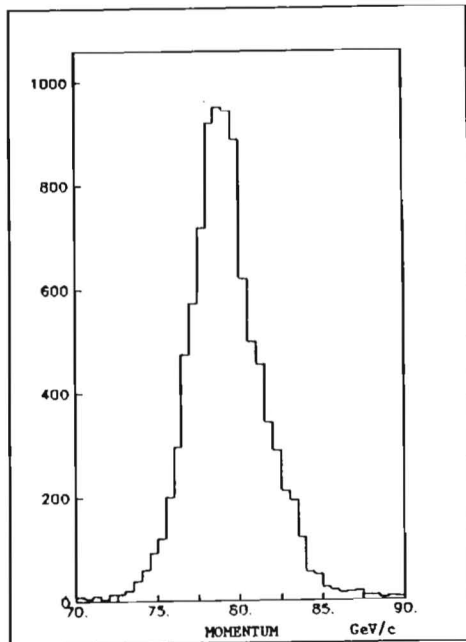


**Fig. 6.2** Secondary beam momentum spectrum for the 80 GeV/c data collection.

### 6.3 Beam momentum measurement

Our experiment used pion beams at two different momenta in order to study scaling violations, especially in the region of large  $x_F$ . To achieve unambiguous comparisons it was necessary to know the absolute beam momentum spectrum with good accuracy. A direct measurement of the beam energy was performed by mounting a spectrometer just upstream of our detector, and tagging each beam particle in low intensity runs. Four stations of three planes of drift chambers were used together with a dipole magnet capable of producing field integrals up to 1.35 GeV/c. The two lever arms were 17 and 12.5 m long. The measurement resolution was 0.4 GeV/c, with systematic error estimated to be 0.6 GeV/c (see Section 12.4.1). The result of the study is shown in Figure 6.2. The average of the distribution is 79.3 GeV/c. The width is 3.0% r.m.s..

### 6.4 Intensity monitors

The intensity was monitored by four ionization chambers; one of them measured the flux of primary protons, and three measured the pion yield. Two of these chambers were segmented into five concentric rings individually read out. The last measurement took place 1.5 m upstream of our target. The beam profile was monitored by several multi-wire ionization chambers, with wire spacing of one, or two millimeters.

Other intensity monitors were provided by two telescopes of scintillators at  $45^\circ$  from the target. Some special runs at low intensity made use of counters placed directly in the beam path.

### 6.5 Spill structure, detector dead-time and trigger time resolution

The RF structure of the Fermilab beam is characterized by *buckets* of particles separated by 18.6 nsec intervals. With an intensity of  $3 \times 10^9$  pions in fifteen seconds, the average number of particles per bucket is 3.7. The bucket population is subject to substantial variations of the beam intensity during the spill.

We used a Čerenkov counter operated at atmospheric pressure to monitor the variations of spill intensity. In order to use the Čerenkov counter as a beam structure monitor, we had to adjust its discriminator threshold to around 10-15 simultaneous particles, thus monitoring only the highly populated buckets. Intensity correlations over ranges of the order of 100 nsec were studied, and we concluded that the effective spill length was about 5-10 sec, therefore increasing by a factor of two the instantaneous average intensity.

The Čerenkov counter also provided a measurement of the detector dead-time. This was obtained by recording the number of Čerenkov counts in each spill as gated by logic levels describing the

status of the triggering and data acquisition systems. We collected the great majority of our data with detector live-time between 60 and 70%. The dead-time was due in equal amount to the beam muon veto from the *A* and *B* banks of counters, and to the time spent by the on-line computer in data acquisition.

The 18.6 nsec RF cycle determined the time scale in which triggering detectors must operate. The scintillator pulses were discriminated to logic signals with lengths between 25 and 35 nsec. This appeared to be a safe way to operate our trigger processors, since the Level-1 and 2 logic was tested to work at full efficiency with simulated signals of 15 nsec width when they arrived simultaneously. Real particle pulses were distributed with FWHM of about 5 nsec, but with tails extending to more than twice that interval.

Because of the large signal widths discussed above, the first two levels of triggers were not able to reject pairs formed by muons belonging to different, consecutive buckets. Notice that the difficulty is created by the large intensity of beam muons produced in pion decays. The single track rate measured in the *F* bank was 6% of the pion intensity, which averaged 3.7 pions per bucket. This implies that about one bucket out of 75 contained two penetrating particles, and there was the same chance of finding muons in consecutive buckets. The acceptance of the detector for such events was drastically reduced by the beam holes in the *C* and *D* banks (Figures 4.6 and 4.7), and by the special requirement for the *F* bank illumination discussed in Section 5.2. As a result less than one in  $10^4$  pairs of beam muons could trigger the detector, noting that the majority of the 1200 triggers per spill was due to such background.

The third level trigger was very effective in reducing the probability of triggering on muons from different buckets. Each Level-1 trigger was associated with a RF bucket and in case of adjacent-bucket

triggers the event was assigned to the second bucket with more than 99% probability. The scintillator latches (Section 5.4) exploited the long width of the signals to achieve a very efficient latch of the second muon, while discriminating strongly against the muon from the first bucket. Notice that this is possible because the latching modules required only three nanoseconds of overlap rather than fifteen as for the trigger logic. The third level trigger, based on latched information, therefore operated with better time resolution than the other parts of the trigger.

## 6.6 Particle rates in the detector

The scintillator discriminators were connected to scalers, which were recorded at the end of each spill. The observed rates in typical conditions were the following:

- 15 MHz in the *C* bank and in the MWPC's;
- 12 MHz in the *D* bank and in the downstream DC's;
- 18 MHz in the *E* bank;
- 12 MHz in the *F* bank.

Some of the counters were exposed to intensity much larger than the average; the highest individual counter rates are listed below:

- 2.5 MHz in the *Cx* bank;
- 2.3 MHz in *Cy*;
- 3.6 MHz in *Cu*;
- 2.3 MHz in *Dx*;
- 3.1 MHz in *Dy*;
- 4.0 MHz in *Du*;
- 2.7 MHz in *E*;
- 2.2 MHz in the *F* bank.

We already mentioned (Section 4.5) that the average efficiencies were 95% in the MWPC's and 90% in the DC's. The scintillator efficiency

will be discussed in Section 6.9.

### 6.7 On-line tests and data acquisition

The trigger logic was checked by event simulation programs executed every few hours. A thorough check was possible because every discriminator and latch could be loaded with computer generated patterns simulating the full complexity of signals to be processed by all three trigger levels. In addition the programs checked the contents of look-up tables for the third level of trigger. The performance of the chamber read-out was checked during the weekly shut-down periods.

The data acquisition program was a version of *Multi*, supported by Fermilab. Our version allowed event displays of scintillator and chamber information, and produced various other diagnostic histograms and scatter plots. The *Multi* histogramming package was rewritten in machine language which allowed a factor of 10 improvement in speed over the standard version. Several other cumbersome features of *Multi* regarding the beginning and ending of runs were circumvented by machine language subroutines. The program ran on a PDP 11/45 computer, equipped with a bipolar memory unit for fast program execution, as well as bulk memory modules for temporary event storage. The data acquisition electronics were interfaced to the computer via two CAMAC branches with a total of 14 crates.

The events were written onto high density tapes (6250 bpi), each containing about 160000 triggers collected in two hours of beam time. For each event, all the scintillator latches, pad-latches, and the track combination words issued by the third level processor were recorded on tape as well as chamber hits. End of spill records contained scaler and ionization chamber rates, together with records of the detector magnetic field intensities.

For diagnostic and calibration purposes, every 1000<sup>th</sup> Level-1

trigger (*pre-scaled trigger*) was also recorded.

### 6.8 Off-line trigger tests

The scintillator latches written on tape allowed us to monitor the trigger consistency within hours of the writing of the tape. The kind of information available in this way is comparable to that provided by the on-line diagnostic programs, with the advantage of using hits distributed with actual time spreads, and the disadvantage of testing only events that fulfilled all the hardware trigger requirements.

Three different tests were considered:

- a) use of the Level-1 latches ( $Cx, Cy, Dx, Dy, E, F$ ) to test the consistency of Level-1 and the output of Level-2 ( $Cy_{match}, Dy_{match}$ );
- b) use of the  $Cx, Cy_{match}, Cu, Dx, Dy_{match}, Du$  latches to test the three-fold coincidences recorded in the pad-latches;
- c) use of the pad-latches to monitor the Level-3 pattern reconstruction and consistency.

The results of these tests are the following:

- \* Typically 98.5% of the events written on tape satisfied the Level-1 and Level-2 logic, with 90% of the errors coming from the  $E$  and  $F$  trigger requirements, which were not enforced by Level-3.
- \* Discrepancies between the written and recomputed  $y$ -matches were present at a 2% rate. This indicates a discrepancy between the signals at the trigger boxes and the pattern which is actually latched. The errors were equally divided between the cases of too many or too few matches. Since the processors always worked correctly with simulated patterns, the problem is presumably connected to the time of arrival of the pulses. Triggers on muons belonging to different buckets can reproduce both effects, especially with multi-muon events, since the latches tended

to record delayed pulses, while the trigger logic was more sensitive to signals from early buckets. Given the small size of the effect, this was not considered a real trigger problem.

- \* The pad-latches were found consistent with the Level-2 latches and with the  $u$  ones to an accuracy of 0.1%. A small discrepancy is to be expected because of a peculiar design feature of the scintillator latches (Figure 5.6). These latches would pass the input signal to the Level-3 logic during the 5 nsec gate, and then latch the state of the signal at the end of the gate. If the input signal ended during the gate a short pulse was sent to the Level-3 latches where it was recorded. The scintillator latches will not have latched this signal however. This scenario could arise only when the scintillator was struck in the RF bucket previous to that which contained the triggering event.
- \* The Level-3 processor appeared to be very reliable: the off-line program verified all the reconstructed patterns for each event, and discrepancies with pad-latches were found in less than 0.1% of the triggers.

## 6.9 Scintillator efficiency studies

The voltages for the scintillation counter photomultipliers were set using the pulse height of signals from conversion of gamma rays emitted by  $\text{Co}^{60}$  sources. The signals were timed using the same radioactive source by comparing each scintillator with a test counter, exploiting the fact that two gammas are emitted simultaneously. This study was repeated twice before the data taking, and studies of the scintillator signals were made with real beam on many occasions.

Despite the great care in the scintillator calibration with radioactive sources, the use of a very intense beam required additional understanding of the scintillator efficiency both at high intensity, where

most of the data was collected, and at low intensity, where some runs were taken for normalization purpose.

The most effective method of measuring the efficiency at high intensity was provided by a set of special runs made with simplified versions of the trigger. We took data with Level-3 requirement but removing the  $E$  or  $F$  bank from the Level-1 trigger. In other runs we took data with only the first level requirement, but without the  $C$  or  $D$  banks. During part of each special trigger run the polarity of the selection magnet was changed in order to illuminate the whole detector evenly with tracks. After we performed the event analysis, reconstructed tracks were used to determine the efficiency in the banks not used in the trigger.

The results showed that while for most banks the efficiencies were rather good (better than 99% on the average), the efficiency was surprisingly low for the  $Cu$  and  $Du$  counters, with average values of 95% and 97%. The inefficiencies were not localized in single counters (with the exception of one bad  $Cu$  channel), but they were approximately uniformly distributed along vertical direction, and they were much more serious in the positive- $x$  side of the detector where the counting rates were higher because of negative muons from beam particle decays. See Figure 6.3.

The wire chambers were little affected by the high particle intensity. Figure 6.4 shows the efficiency measured for a MWPC and a DC plane, obtained using all the tracks reconstructed on a typical data tape. The MWPC efficiency plot shows a dip in the area of higher intensity. The DC plot shows a pattern of inefficient time digitizers, identified by the periodicity of seven wires characteristic of the relation between chamber cells and digitizer boards.

Various methods were devised to track the intensity dependence of this problem, and we took advantage of the fact that the worst

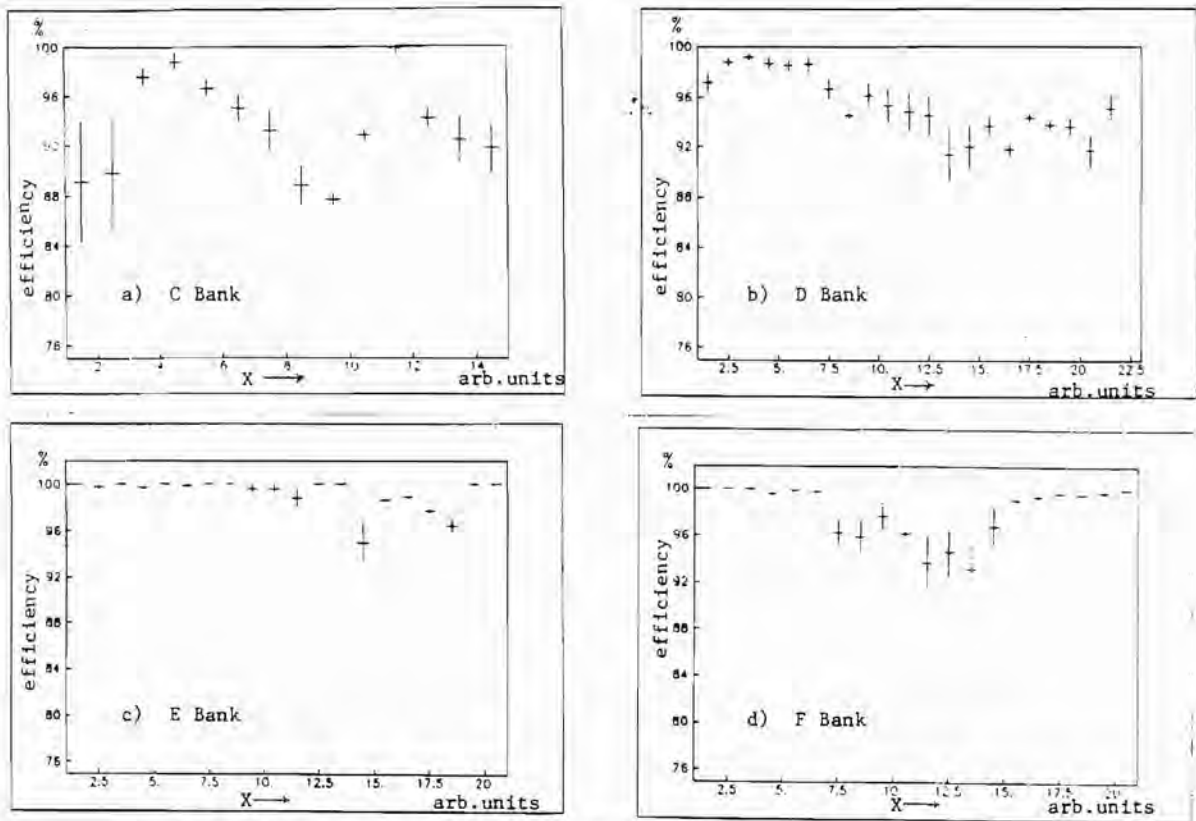


Fig. 6.3 Efficiency profile of the scintillator banks, projected on the x-axis:

- a) C bank
- b) D bank
- c) E bank
- d) F bank

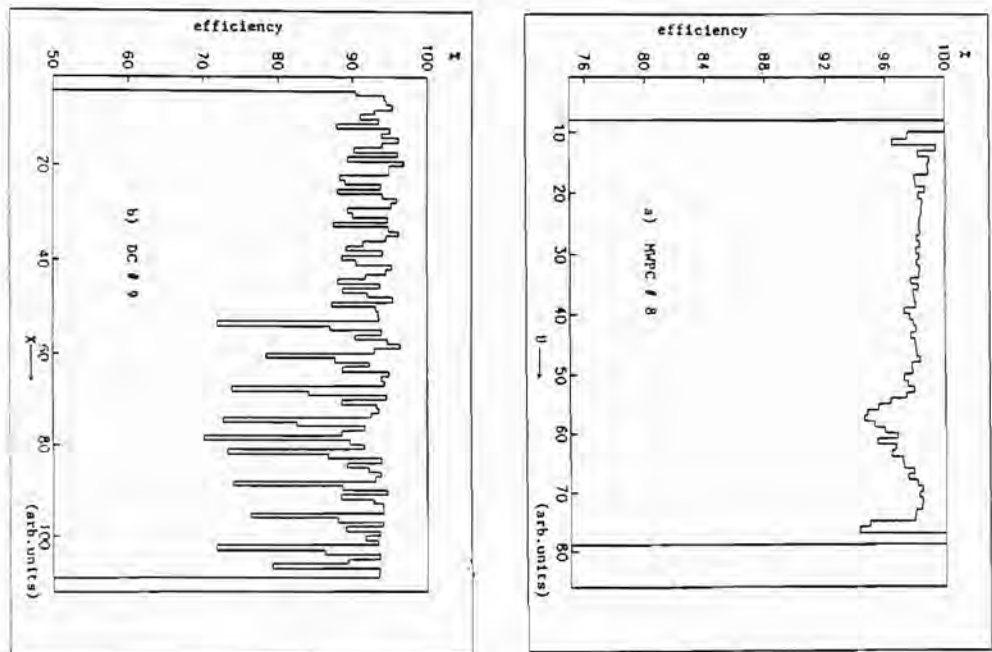


Fig. 6.4 Efficiency profile for the MWPC no. 8 (a), and DC no. 9 (b).

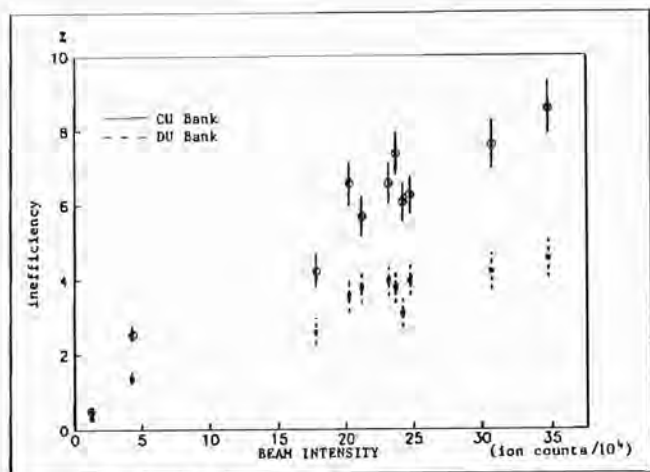


Fig. 6.5 Beam intensity dependence of the inefficiency of the *Cu* and *Du* banks. The intensity value at full scale corresponds to  $4.8 \times 10^9$  pions per spill.

counters were the ones which could be continuously monitored using the pre-scaled Level-1 triggers. The inefficiency turned out to increase linearly with the intensity, almost disappearing in the runs taken at low intensity, as shown by Figure 6.5.

The inefficiency was therefore primarily due to 'pile-up' of pulses. The uniformity along the vertical direction is due to the fact that the *u* counters extended approximately along that direction. The areas of the *Cu* and *Du* counters were almost twice those of counters in the corresponding *x* and *y* banks, and so these banks would have the worst pile-up problems. They were subject to average rates as large as 3-4 MHz per counter, and instantaneous rates which were probably more than twice as large during short time intervals, because of the spill structure. It is quite conceivable that the phototube bases 'sagged' during peak intensities.

Another mechanism might have participated to some extent in reducing the latching efficiency in these banks. Since they were not used in the lower trigger levels, the signals were brought to the counting room with normal rather than foam coaxial cables, producing somewhat longer pulses. The *u* signal widths at the discriminator output were set to 25 nsec, while the *E*'s and the *F*'s were set to 29 nsec, and the other *C* and *D* banks to longer values. It was not uncommon to have muons in two consecutive buckets cross the same counter (14% chance in the most unfavourable cases, with 50% duty cycle), and the discriminators were probably scarcely efficient in firing on the second bucket. This in turn induced a latching inefficiency, because of the bias against latching on a signal coming in an earlier bucket which was made in the timing of the latches. Observe that both reasons point to conceivable inefficiencies in the *u* banks: their higher counting rate and the shortness of the discriminator pulses.

To conclude this section, I would like to mention another kind of efficiency study which produced somewhat ambiguous results as to the scintillator efficiency, the so-called 'analysis of the third muon.'

The event trigger was based on two particles. Thus whenever more than two muons were recorded, we had the possibility of studying particles not subject to trigger bias, by using those tracks that could be eliminated without altering the presence of triggering conditions. Most of our multi-muon events were not useful, because they typically contained out-of-time tracks produced in buckets different from the one in which the trigger was satisfied, and because they were characterized by anomalous DC patterns, and low MWPC and scintillator efficiencies. Still, each of our 230 data tapes contains a sample of a few hundred *real* multi-muon events, which could be used for efficiency studies. Even with the preceding cautions the method

unfortunately turned out to be strongly biased. In fact it suggested very low efficiency values, incompatible with those determined with the special trigger runs at high intensity or with the prescaled Level-1 events. It was important to note that the limit of 15 allowed Level-3 pair candidates (Section 5.4) was a strong constraint on the number of scintillator latches in multi-muon events, and biased the trigger towards events with higher scintillator inefficiencies. This effect was small in normal, two-muon data, but became important in the kind of studies we are now discussing.

### 6.10 Chamber alignment and calibration

Initial measurements of chamber positions were obtained with direct surveys, with estimated resolutions in the range of  $50\text{--}100\mu\text{m}$ . The alignment was checked and improved using special runs with the spectrometer magnet field off. Undelected muon tracks established transverse positions for each plane of wires to about  $20\mu\text{m}$  for the DC's, and  $60\mu\text{m}$  for the MWPC's. The longitudinal positions were obtained with about four times larger errors, and planarities and tilt angles were measured to better than 1 mrad accuracy for all 31 chamber frames.

The alignment was further routinely checked during the primary analysis of the data tapes. We discovered that the forces due to the fringing field of the spectrometer magnet were large enough to move the nearby chamber frames by as much as a few millimeters—despite their being constructed out of stainless steel. The magnets were shut down weekly together with the whole accelerator, and the chamber equilibrium positions after turning on the fields were in many cases changed by measurable amounts, requiring the determination of new alignment constants.‡

‡ New alignments were required more often. The spectrometer mag-

Together with the alignment, a periodic calibration of the time offsets of the DC's was performed. Changes in the offsets were probably related to variations in the drift velocity due to occasional problems with the gas mixture, and to the replacement of faulty preamplifier or time-digitizer modules, rather than being due to variations of the trigger timing. The necessary adjustments were always very small, and satisfactory results were obtained by correcting an overall time offset for each of the 28 drift chamber modules. The calibration was done systematically after first revising the chamber alignment. For each frame, the residual between the reconstructed point and the fitted track was multiplied by a factor  $\pm 1$  according to the point being on the positive or negative  $x$  side of the sense wire. The center of the resulting residual distribution indicated the necessary time offset correction. As in the case of the alignment, the method was sensitive to about  $20\mu\text{m}$ , corresponding to 0.4 nsec. For the 210 data tapes collected in seven weeks of running, we used 30 different sets of calibration constants.

net turned out to be one of the weakest elements of the beam line. Cooling problems forced many unwelcome power trips, not to mention a fire in the magnet coils which occurred at the early stages of data taking but which fortunately did not involve other parts of the detector.

## Chapter 7

### EVENT RECONSTRUCTION

#### 7.1 Overview of the data analysis

About 40 million muon pair triggers were collected in 400 hours spread over 7 weeks of beam time. The data analysis was organized in several steps performing the following tasks:

- a) Enforcement of an off-line scintillator trigger. This used a more powerful algorithm than that implemented in the hardware trigger processor, and also utilized the signals from the  $F$  bank which were not available to the on-line Level-3 trigger.
- b) Track reconstruction of the events passing the off-line scintillator trigger requirement. Effects of the fringe field, vertical focussing, and effective magnetic center in the spectrometer magnet were taken into account. Global fitting routines were able to eliminate unlikely hits from the fit, and/or replace them with hits not found in earlier stages of the reconstruction.
- c) Fitting for the event parameters at the interaction point, taking into account the multiple scattering in the hadron absorber. Loose cuts to the probability of production in the target were also applied.
- d) Final analysis, including rejection of background from decays of

beam particles, application of fiducial cuts, and requirement of a full match between chamber tracks and scintillation counters. Tighter  $\chi^2$  cuts for the fit to the target were applied.

The requirements in a) reduced the number of events to about 16 million; after c) we were left with 1.7 million events with mass larger than  $2.0 \text{ GeV}/c^2$ ; and the final sample consisted of 103000  $\mu^+\mu^-$  events with  $M > 2.5 \text{ GeV}/c^2$ ,  $x_F > .3$ , and 4060 pairs with  $M > 4.0 \text{ GeV}/c^2$ ,  $x_F > .15$ . A typical reconstructed event is shown in Figure 7.1.

The Montecarlo study of the detector acceptance, the normalization and the results of the experiment will be discussed in the next chapters. Some details of the reconstruction algorithms will be considered in the following sections.

#### 7.2 Off-line trigger enforcement

In Section 5.4 we discussed how the third level trigger had the ability to select certain patterns. In particular we rejected  $\mu^-\mu^-$  pairs, and pairs characterized by unlikely momentum-angle combinations or low mass topologies. Off-line we had the advantage of comparing the pattern found in the  $C$  and  $D$  banks with the signals detected in the most downstream banks. In this case an additional test of the hypothesis that the event was produced in the target was possible using a third position measurement in the bending plane.

We required that at least one member of the pair candidate had a match in the  $F$  bank. Multiple scattering and limited resolution were accounted for by allowing a wide and momentum dependent difference between projected track and center of a struck  $F$  counter. The match enforced the requirement on the  $F$  illumination discussed in Section 5.2. The method turned out to be very effective in eliminating triggers

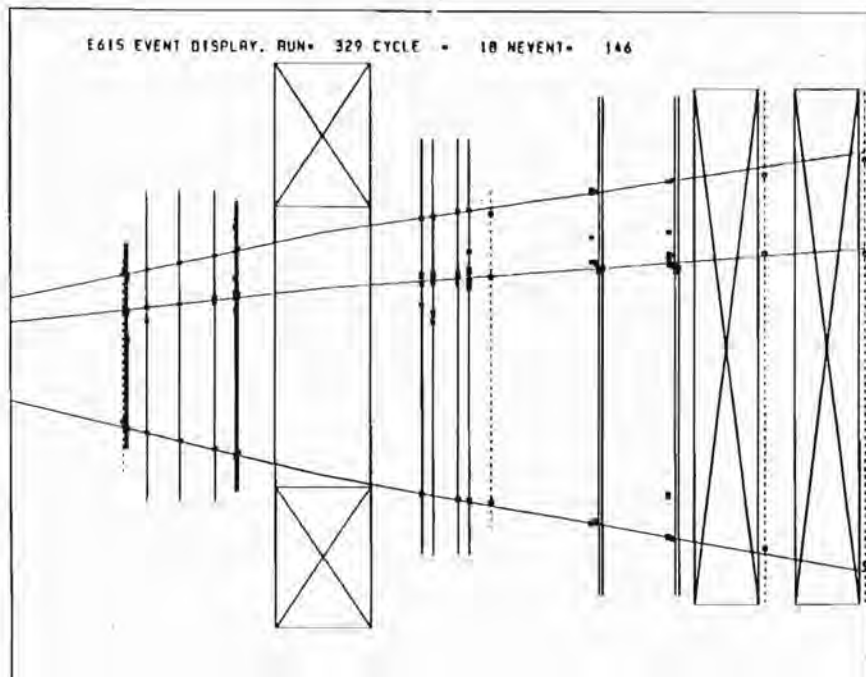


**Fig. 7.1** Plot from the track reconstruction program. The spectrometer region and the downstream *E* and *F* banks are shown. Only the  $x$  planes of the wire chambers are displayed.

where this requirement had been satisfied by a track which could not have been produced in the target.

We also used all the information from the scintillator banks to estimate the invariant mass for each pair candidate. The resolution in the mass value in the  $J/\psi$  region was about  $.25 \text{ GeV}/c^2$  r.m.s., to be compared with  $.14 \text{ GeV}/c^2$  obtained using the wire chambers. This result shows the benefit of the mass selection magnet in providing event topologies which were easy to identify in the trigger. The  $.25 \text{ GeV}/c^2$  mass resolution includes a component of  $\sim .14 \text{ GeV}/c^2$  from multiple scattering and  $\sim .2 \text{ GeV}/c^2$  from the granularity of the scintillator banks. Therefore, cutting all the events with scintillator-based mass smaller than  $2.0 \text{ GeV}/c^2$  had negligible effects on the mass spectra obtained with the wire chambers, for  $M > 2.6 \text{ GeV}/c^2$ .

### 7.3 Cuts on record length

Before passing to track reconstruction, events were selected by cuts designed to reduce the necessary computer time. The requirements are listed in Table III.

About 10% of the triggers were eliminated due to anomalous record lengths or read-out errors. Most of the losses were due to events containing showers in the upstream detectors.

The loss of real muon pairs has been estimated to be of the order of 1%. This was inferred by studying the record length distribution for events passing all reconstruction cuts (See Figure 7.2).

### 7.4 Upstream chamber reconstruction

The reconstruction of tracks between the selection magnet and the spectrometer magnet was based on the nine planes of MWPC's. The algorithm searched for line segments in space by combining struck wires in the MWPC's, which measured  $x$ ,  $u$  and  $v$  coordinates. Four

**Table III** Length cuts applied to the event data string.

1) Number of MWPC hits	$\leq 150$
2) Number of DC words	$\leq 300$
3) Number of MWPC hits	$\leq 100$
or	
Number of DC words	$\leq 250$
4) Number of Upstream DC words	$\leq 100$
5) Number of Midstream DC words	$\leq 250$
6) Number of Downstream DC words	$\leq 250$

levels of complexity were considered, and the program would enter a more complex level only if no more than 50 msec had been spent in the reconstruction. The different levels are the following:

- all 9 point tracks were searched for, followed by the 8 point, the 7 point and the 6 point tracks distributed like 3-3-0 in the three projections;†
- search for 6 point tracks distributed as 1-2-3;
- search for the remaining 6 point tracks—of the kind 2-2-2;
- search of the tracks with five points.

In the track search, roads with 3 mm half width were used when matching a third point in one projection, or comparing the three projections. Tracks with more points would be preferred to ones with less in cases of common points. The program did not look for more

† We use the word **point** to mean the coordinate measured by a struck wire in a chamber plane. Only one point per chamber plane could be used on each track.

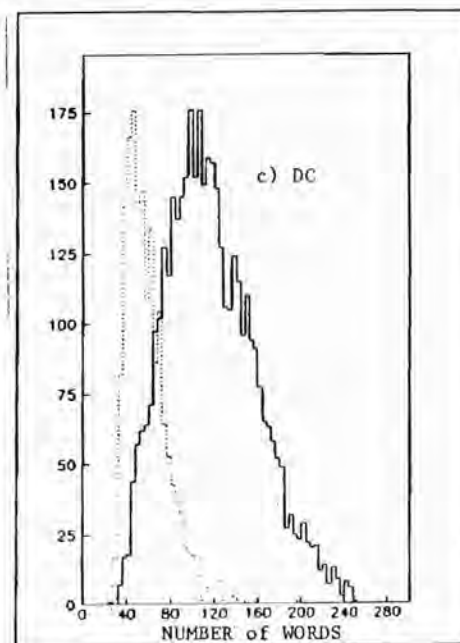
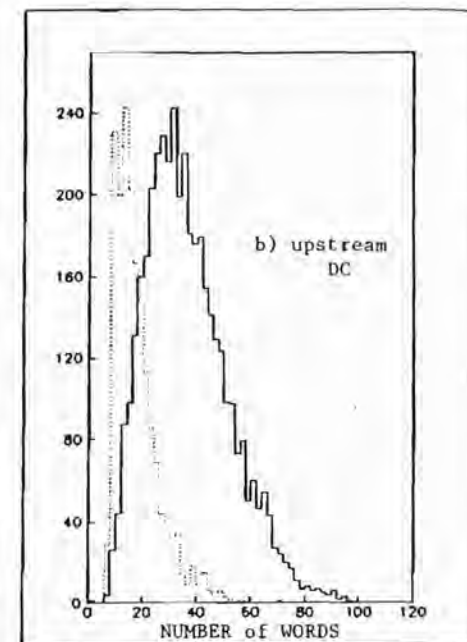
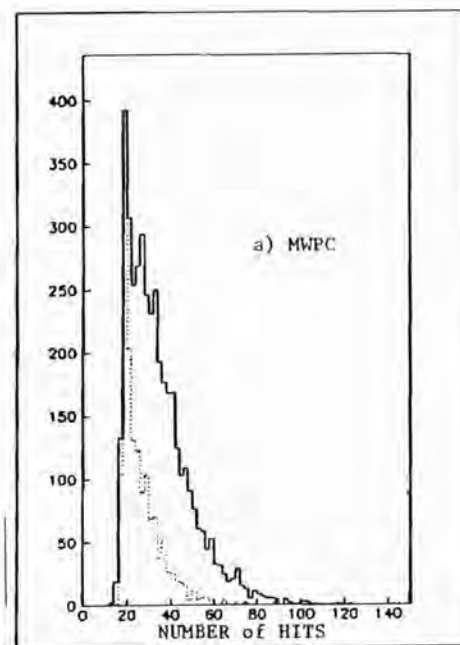


**Fig. 7.2** Hit multiplicity distributions for various groups of wire chambers.  
**a)** MWPC's;  
**b)** Upstream DC's;  
**c)** All DC's.  
 The dotted lines correspond to special low intensity runs.

than 20 tracks in each projection. A match with struck scintillators in 2 out of 3 of the  $Cx$ ,  $Cy$  and  $Dy$  banks was required, together with a loose alignment in the non-bending plane with the target position.

The efficiency of the reconstruction depended on the time spent in the reconstruction, which was monitored by the program itself. At high intensity, step d) was executed 87.1% of the time, and step b) was reached in 98.8% of the cases. Steps a) and c) were rather fast, and 98.5% of the events completed step c). Given the average plane efficiency of 95%, the MWPC track finder is estimated to have found muon pairs in 99% of the cases.

For each found track in the MWPC's, a search was made for matching points in the 4 planes of upstream drift chambers. In over 99% of the tracks this improved the accuracy of the upstream track reconstruction by a factor of 2 due to the increased resolution of the drift chambers.

A further fit was then performed, correcting for small departures from orthogonality to the  $z$ -axis of the chamber planes, and eliminating points which contributed greatly to the  $\chi^2$  of the fit. The minimum number of MWPC points was still kept at 5, and the fit was iterated up to 5 times, if the fit probability remained smaller than 2%.

### 7.5 Downstream reconstruction

The program looped first through the 8 planes of  $x$  drift chambers. (For this drift chambers 11, 12 and 13 of Figure 4.4 are grouped into a single plane, *etc.*) The method was similar to the one used in the MWPC's, but with roads 1.5 mm wide. One of the pivot points was chosen in the upstream group of six planes (shown as Drift 5-10 on Figure 4.4), and one in the downstream group (Drift 11-28 on Figure 4.4). A match with two out of three scintillators in the  $Dx$ ,  $E$

and  $F$  banks was required. Also the  $x$  drift track must match with some MWPC track when projected to the center of the spectrometer magnet.

The efficiency for the reconstruction of a particle pair was estimated to be equal to 99%.

The search for corresponding points in the downstream  $u$  and  $v$  chambers was performed starting with the projection of the MWPC track which matched the  $x$  drift track. Very wide roads were used — up to 9 cm in the  $y$  direction. If any drift  $u$  or  $v$  point matches were found new roads were defined based on these drift points as well as the MWPC track, and the search was iterated. While the presence of drift  $u$  and  $v$  points was not an absolute requirement for a reconstructed track, only 0.3% of the tracks failed to have at least one.

A tridimensional fit of the downstream pattern was then performed after correcting for the small tilt angles of the planes. Tracks with low  $\chi^2$  probability were examined for possible improvement by eliminating the point with the largest contribution to the  $\chi^2$ . Also the quality of the fit was checked when each point was replaced by the ambiguous or *ghost* point reconstructed on the other side of the drift chamber cell. This iteration was performed up to 10 times, if the  $\chi^2$  probability remained below 5%. The elimination procedure was modified by a correction to the probability which tended to maintain the observed average point multiplicity. A point would be restored if the probability after eliminating it was worse than the initial one. The number of  $u$  and  $v$  points could not be reduced below 2.

The drift chambers were also used to test for out-of-time tracks. If a track had a reasonably high number of hits distributed on both the negative  $x$  and the positive  $x$  sides of the cells, a new parameter was let free to vary in the fit, determining the time offset. Figure 7.3 shows the distribution of the time offset for a typical data tape.

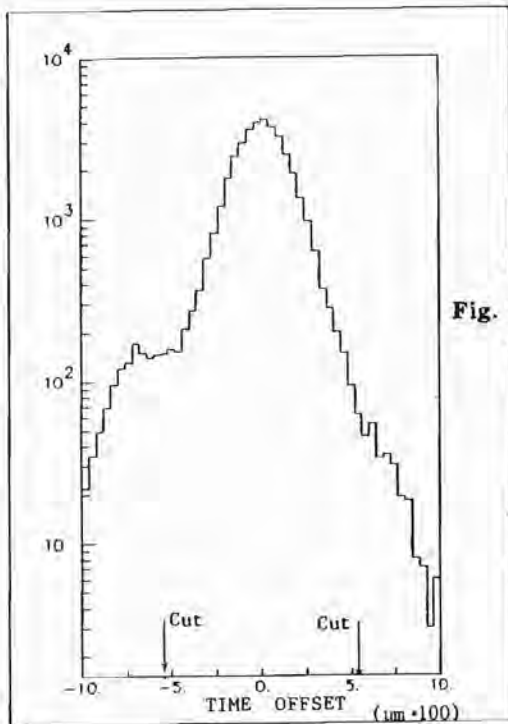


Fig. 7.3 Spectrum of the time-offset for the DC track reconstruction. Notice the shoulder corresponding to particles produced in an earlier RF bucket. (1 nsec  $\approx$  50  $\mu$ m)

A resolution of about 2.3 nsec was obtained in this way, allowing us to distinguish tracks from the neighboring RF buckets, which were 8 standard deviations away. A cut was placed at 5 standard deviations. Tracks failing this cut were flagged, and were not subjected to the global fitting described below. About 10% of the reconstructed track could not be analyzed in this way, as not enough information is available to determine the time offset if most points lie to only one side of the drift cells.

## 7.6 Global fitting

In the final part of the track reconstruction the two segments upstream and downstream of the spectrometer magnet were used together in a global three-dimensional fit.

The bend in the magnetic field was accounted for by requiring two segments to meet at an effective 'magnetic center.' The latter was determined such that the two segments had the same length within the magnetic field (Figure 7.4).

The shift in the magnetic center from the geometric center of the magnet was typically of the order of 1 mm, small enough to produce very little effect on the fitted slopes.

To account for the fringe field in the region occupied by the wire chambers, we corrected the chamber points before using them in the global fit. We shifted their transverse coordinate according to the formula:

$$\delta x = \frac{I_n \cos \theta_{zx}}{P_{zx}} \quad (7.1)$$

where  $\theta_{zx}$  and  $P_{zx}$  are respectively the track angle and momentum in the bending plane, and  $I_n$  is a coefficient determined for each chamber plane. See Figure 7.5 and Table IV. The largest correction occurred for the last upstream drift chamber (no. 4 on Figure 4.4), where the coefficient was found to be equal to 4070  $\mu$ m GeV/c. These shifts turned out to be typically much smaller than the resolution provided by the chambers, but nevertheless neglecting the correction would have produced a systematic error in the reconstructed momenta.

In the non-bending plane we corrected for effects due to the  $z$  component of the field present in the fringe region. This component causes a difference in the slopes between the upstream and downstream segments, and a difference in the intercept at the magnetic

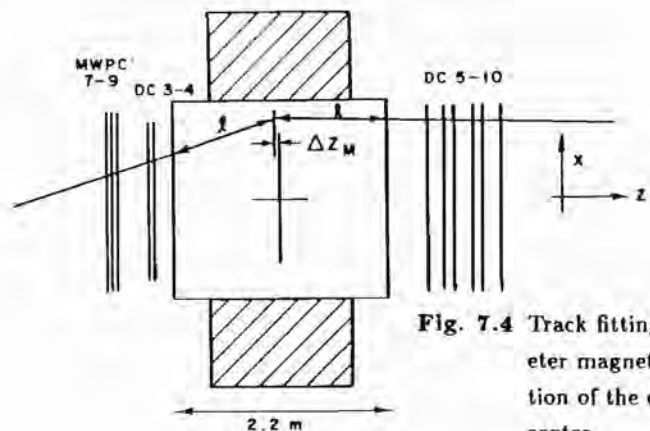


**Fig. 7.4** Track fitting in the spectrometer magnet area: determination of the effective magnetic center.

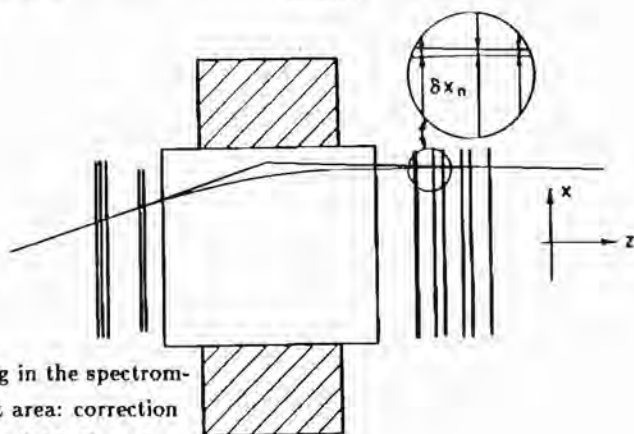


**Fig. 7.5** Track fitting in the spectrometer magnet area: correction for magnetic field effects in the wire chamber regions.

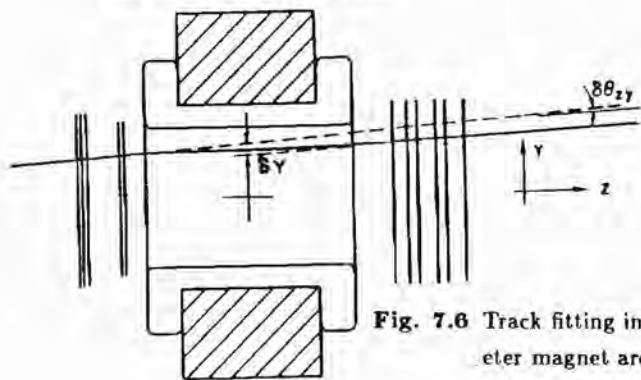


**Fig. 7.6** Track fitting in the spectrometer magnet area: correction for effects in the the  $y$ - $z$  plane.

**Table IV** Parameters  $I_n$  for track fitting in the fringe field of the spectrometer magnet.

FRINGE FIELD PARAMETERS (m GeV/c)		
	upstream	downstream
MWPC # 9	.000982	DC # 5 .002020
8	.001094	6 .001074
7	.001163	7 .000857
DC # 3	.003543	8 .000405
4	.004069	9 .000244
		10 .000128

center (Figure 7.6), given by the following expressions:

$$\delta \tan \theta_{zy} = \frac{0.03 B}{P_z} (y_{IN} \tan \theta_{zx,IN} - y_{OUT} \tan \theta_{zx,OUT}) \quad (7.2)$$

$$\delta y = \frac{0.03 B}{P_z} (y_{IN} \tan \theta_{zx,IN} + y_{OUT} \tan \theta_{zx,OUT}) \frac{L}{2} \quad (7.3)$$

where  $B=13.8$  KGauss is the field intensity at the center of the magnet,  $L$  is the effective length of the magnetic volume—set equal to 2.2 m—at the edge of which we take the values of the track intercepts and slopes. As for the previous correction these shifts turned out to be typically much smaller than the chamber resolution.

Following the same method as in the upstream and downstream fitting routines, the global fitting procedure checked the quality of the points used in the fit and rejected poor ones or looked for substitutes. Up to fifteen iterations were performed if the global fit probability remained smaller than 3%. The procedure did not to eliminate downstream  $u$  or  $v$  points if there were less than three of them.

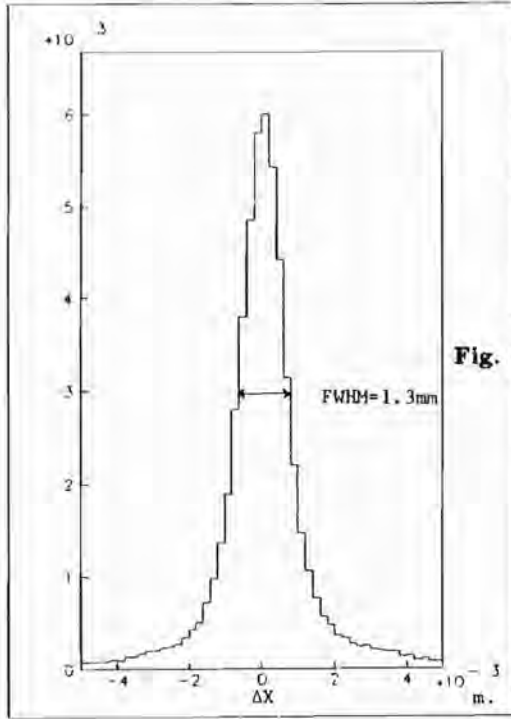


**Fig. 7.7** Difference between upstream and downstream track segments at the spectrometer magnet center.

Figure 7.7 shows the difference between the upstream and downstream segments at the center of the magnet, just before the global fit procedure is applied.

The width is  $550\mu\text{m}$  r.m.s.. Our resolution in measuring particle momenta is given by:

$$\sigma(P_{zx})/P_{zx} = .02 \cdot P_{zx} \%,$$

with the momentum given in GeV/c, while the slopes of the tracks leaving the absorber were obtained with accuracy

$$\sigma(\theta_{zx}) = .1 \text{ mrad}, \quad \sigma(\theta_{zy}) = .3 \text{ mrad}.$$

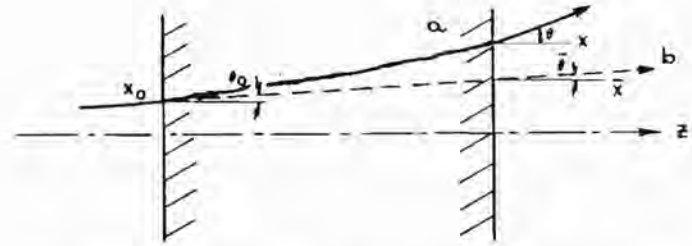


**Fig. 7.8** Variables used in the multiple scattering formalism:  
a) scattered trajectory (solid curve);  
b) unscattered trajectory (dashed curve).

### 7.7 Multiple scattering and transport in the selection magnet

Charged particles passing through material are affected by small angle elastic scattering due to Coulomb interactions. On the macroscopic scale, the process is described in, say, the  $x-z$  scattering plane by a probability distribution written in terms of the deflection  $\theta - \bar{\theta}$  and the displacement  $x - \bar{x}$  between the final track parameters and the most probable parameters, *i.e.* those of the unscattered trajectory (Figure 7.8).<sup>34</sup>

The probability distribution depends on the thickness of the material and on its radiation length. For small scattering angles, it becomes gaussian and can be expressed by a two-dimensional  $\chi^2$ :

$$\chi_{ms}^2 = A(\theta - \bar{\theta})^2 + 2B(\theta - \bar{\theta})(x - \bar{x}) + C(x - \bar{x})^2. \quad (7.4)$$

The coefficients are given by

$$A = \frac{8P_{in}P_{out}}{(.021\text{GeV}/c)^2} \frac{X_0}{Z}, \quad B = -1.5A/Z, \quad C = 3A/Z^2 \quad (7.5)$$

where we make use of the initial and final track momenta, the radiation length  $X_0$  and the thickness of the material  $Z$ . A similar expression can be written for the scattering in the orthogonal plane,  $y$ - $z$ .

We wish to use expression (7.4) to extract the most probable values of  $x$  and  $\theta$  before the particle passed through the absorber. For this we need the transport equations

$$\bar{\theta} = \bar{\theta}(x_o, \theta_o), \quad \bar{x} = \bar{x}(x_o, \theta_o) \quad (7.6)$$

for the unscattered trajectory in terms of the initial values  $x_o$  and  $\theta_o$ . Assume for the moment that we know the form of these equations, which are discussed later in this section. We are also aided by the knowledge that the beam spot at the target has an approximately gaussian shape with mean  $\bar{x}_o$  and spread  $\sigma_x$ . Thus we can form a combined probability distribution with

$$\chi^2(x_o, \theta_o) = \chi_{\text{ms}}^2(x, \theta; x_o, \theta_o) + \frac{(x_o - \bar{x}_o)^2}{\sigma_x^2}. \quad (7.7)$$

This could be used to solve for the best estimates of  $x_o$  and  $\theta_o$  given the measurements of  $x$  and  $\theta$  after the absorber, and the 'measurement' of  $\bar{x}_o$ . Furthermore the  $\chi^2$  method provides a measure of the probability of the hypothesis that the particle was actually produced at the point  $(x_o, y_o, z_o)$ .

In our experiment we have two tracks emanating from the same vertex. We can combine the measurements of the  $x$  and  $y$  projections of both tracks into a single vertex- $\chi^2$  which has 6 terms:

$$\chi_{\text{vertex}}^2 = \sum_{4 \text{ terms}} \chi_{\text{ms}}^2 + \frac{(x_o - \bar{x}_o)^2}{\sigma_x^2} + \frac{(y_o - \bar{y}_o)^2}{\sigma_y^2} \quad (7.8).$$

**Table V** Parameters for the multiple scattering  $\chi^2$  in the hadron absorber.

MULTIPLE SCATTERING COEFFICIENTS
$A_0 = 356.2 \times (p^2/\text{GeV}^2/c^2)$
$B_0 = -48.94 \times (p^2/\text{GeV}^2/c^2) \text{ m}^{-1}$
$C_0 = 8.303 \times (p^2/\text{GeV}^2/c^2) \text{ m}^{-2}$

There are 10 measured quantities (4 final slopes, 4 final intercepts, and 2 average vertex intercepts), and we fit for 6 parameters (4 initial slopes and 2 initial intercepts).

We could also fit for the  $z$ -coordinate of the vertex, but this is not useful, since the achievable resolution in this quantity is worse than the geometrical length of the target. It is therefore better to assume  $z_o$  to be equal to the effective target center, obtained weighting with the pion beam attenuation along the target. The multiple scattering coefficients  $A$ ,  $B$ , and  $C$  were computed considering all the materials between the weighted target center and the position of the  $C$  bank. The resulting values are given in Table V.

The effect of chamber resolution on coefficients  $A$ ,  $B$  and  $C$  is always a factor of  $10^3$  lower than that due to multiple scattering, and has been ignored.

Before discussing details of the transport equations (7.6) it may be useful to give some illustration of the merits of the vertex fit procedure using actual data from  $J/\Psi$  events. A simpler procedure would be to calculate the muon pair mass using only the momenta and angles measured downstream of the selection magnet, ignoring all position measurements when correcting for the effect of the selection magnet.

This would yield the mass spectrum shown in Figure 7.9.a.

Another simple procedure might be to ignore the measured slopes and use only the measured positions plus the known target position when determining this initial angles. This would yield the mass spectrum which is shown in Figure 7.9.b, which is already 1/3 narrower than that found with the first simple method. The vertex- $\chi^2$  method combines all available information in an optimal manner, and yields a mass resolution better than either of the simple methods, as shown in Figure 7.9.c. In addition it provides a basis for rejecting events not produced in the target.

Another measure of the quality of the vertex fit procedure is that the r.m.s. error in the reconstructed slopes at the target is  $94/P$  mrad, for momentum measured in GeV/c. This result is dominated by the effect of multiple scattering in the target and absorber and is much larger than the angular resolution of the tracking chambers.

We now turn to the determination of the transport equations

$$\bar{x} = \bar{x}(x_o, \theta_o, P) \quad , \quad \bar{\theta} = \bar{\theta}(x_o, \theta_o, P) \quad (7.6a)$$

which describe the average trajectories across the absorber inside the selection magnet. We first determined a suitable functional form for these equations with the aid of a Montecarlo computer simulation program of the transport through the magnet. Details of this program are given in Chapter 9. Then we used data events in the  $J/\Psi$  peak to determine the parameters of the transport equations.

We started from the measured maps of the magnetic field obtained at 1700 and 2000 Amps (Section 4.2), and extrapolated to the field values for a current of 2500 Amps as actually used in the 1983/84 data collection. The Montecarlo simulation of the transport was based on the average field values in 14 regions along the longitudinal axis

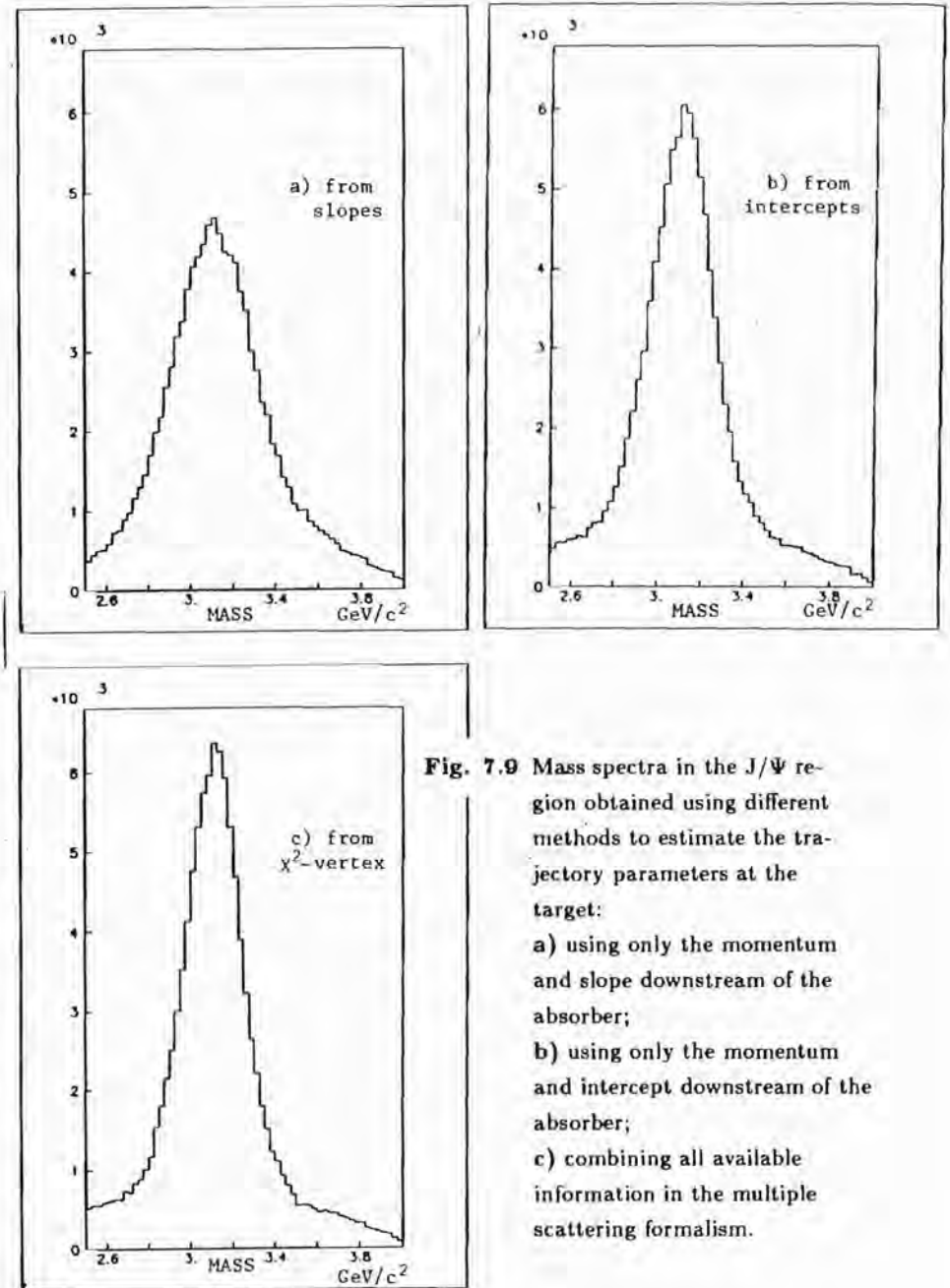


**Fig. 7.9** Mass spectra in the  $J/\Psi$  region obtained using different methods to estimate the trajectory parameters at the target:  
**a)** using only the momentum and slope downstream of the absorber;  
**b)** using only the momentum and intercept downstream of the absorber;  
**c)** combining all available information in the multiple scattering formalism.

(Figure 4.3). The 11 regions inside the magnet correspond to the sections of uniform gap height. We then established a satisfactory form for the transport equations using the simulation program:

$$\bar{x} = x_o \mp \frac{J}{P - \Delta P_J} + \tan \theta_o \Delta z \quad , \quad \sin \bar{\theta} = \sin \theta_o \mp \frac{K}{P - \Delta P_K} \quad (7.9)$$

where  $P$  is the initial track momentum,  $\Delta z$  is the distance between the target and the measurement plane, and the  $\mp$  is used with positive/negative muons. This functional form allowed us to fit the simulated transport with an error smaller than one tenth of the spread due to multiple scattering. The transport equations in the  $y$ - $z$  plane are unaffected by the magnetic field, and are straightforward.

The parameters  $J$ ,  $\Delta P_J$ ,  $K$ ,  $\Delta P_K$  were then optimized using  $J/\Psi$  events from our data sample. It would appear that the goal is simply to determine the parameters in equations (7.9) so that a good mass, and narrow width for the  $J/\Psi$  are obtained using the  $\chi^2$  of equation (7.8). However it turns out that this only requires a good value for a particular linear combination of the parameters  $J$  and  $K$ . We feel that it is very important to have good values for both  $J$  and  $K$  separately, so that equations (7.9) can also be used in the Montecarlo studies of other features of the experiment than fitting the vertex. Each of the two equations (7.9) provides an estimate of the initial angle  $\theta_o$  in terms of the measured quantities  $\bar{x}$  and  $\bar{\theta}$ , to the extent that  $x_o$  is nearly zero. To optimize the parameter  $J$  a study of the  $J/\Psi$  events was made using only the first of the equations (7.9) to determine the initial angle  $\theta_o$ . This of course does not yield a narrow width for the mass peak, but it does determine the parameter  $J$  independently of the parameter  $K$ . A similar study was made to determine  $K$  via the second equation (7.9) only. The resulting values of the transport parameters are given in Table VI.

**Table VI** Parameters for the transport equations in the selection magnet.

TRANSPORT PARAMETERS	
$J = 15.71$	GeV/c m
$\Delta P_J = 1.10$	GeV/c
$K = 3.115$	GeV/c
$\Delta P_K = 1.33$	GeV/c
$\Delta Z = 8.22$	m

The study of the transport equations is illustrated in Figure 7.10. We have selected the events requiring  $|\cos \theta_t| < 0.15$ , in order to deal with pairs formed by tracks of similar momentum. Subsequently, we have formed three groups of different particle momentum: 10–20, 20–30 and 30–40 GeV/c. Figure 7.10.a shows the mass spectra obtained using the second of equations (7.9), which estimates the initial track angle in the bending plane by using the average rotation of the track direction. The good quality of the fit is proven by the absence of any measurable momentum dependence. The mass spectra in Figure 7.10.b were obtained by estimating the initial track angle from the final track intercept, correcting for the magnetic displacement according to the first of equations (7.9), and fixing  $x_o$  to the average beam position. Figure 7.10.c shows the mass spectra obtained with the  $\chi^2_{vertex}$  method. The same study was performed on tracks generated by the Montecarlo program, and analyzed according to the same transport equations. Figure 7.11 shows the mass spectra for simulated events, without selecting symmetric pairs or dividing into momentum

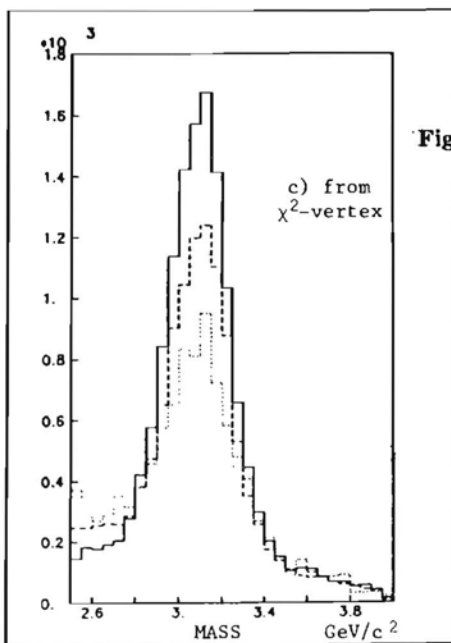
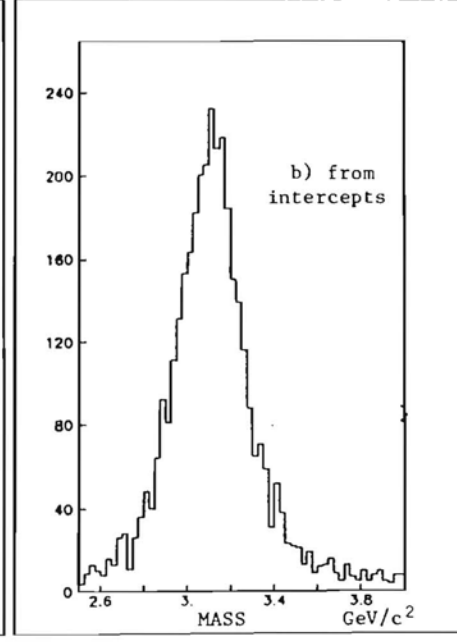
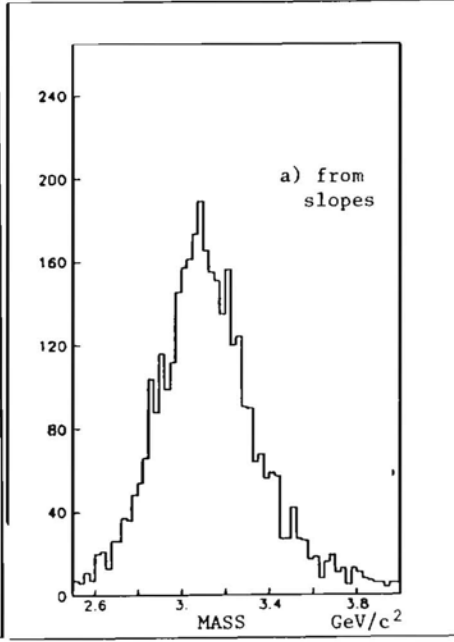
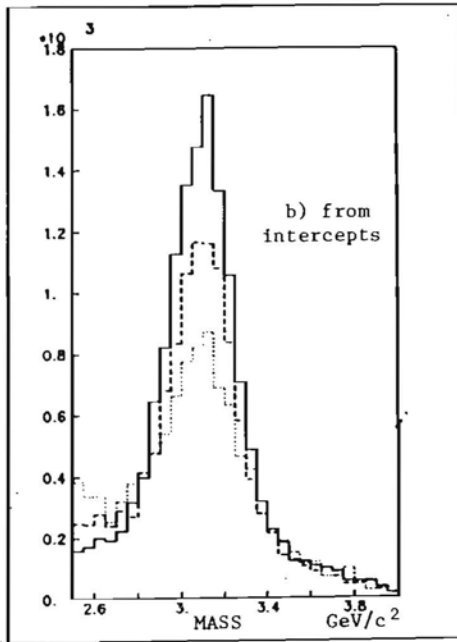
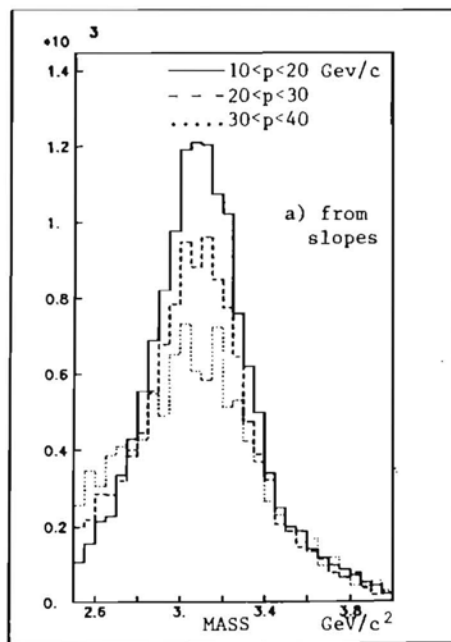


**Fig. 7.10** Mass spectra obtained with the three different methods of estimating the initial trajectory slopes, described in the text and in the caption of Fig. 7.9. Only symmetric events ( $|\cos \theta_i| < 0.15$ ) are used. Within each plot different momentum intervals are shown separately.

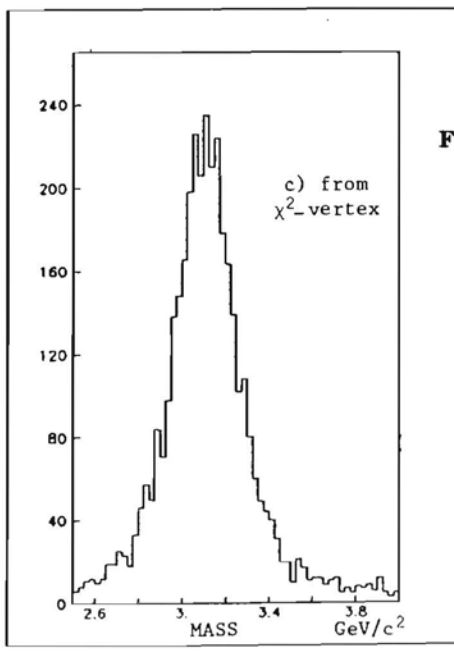


**Fig. 7.11** Mass plots from the Monte-carlo simulation, obtained with the three different methods of estimating the initial trajectory slopes.

intervals. Compare with corresponding spectra for real data shown in Figure 7.9.

A further check on the transport equations was obtained by computing the vertex coordinate separately for each of a pair of tracks, and plotting the difference between the two resulting values. This allowed us to exclude the presence of a wide class of possible transport biases.

At this point we have determined all the parameters needed to make optimal fits to the event vertex in data events. But in addition we can improve a weakness in the Montecarlo simulation, namely the 14 values which represent the field in the selection magnet, which were obtained by a large extrapolation. The parameters  $J$  and  $K$  are in fact certain field integrals for the selection magnet, so that the 14 field steps can be adjusted to reproduce these integrals.

## Chapter 8

### EVENT SELECTION

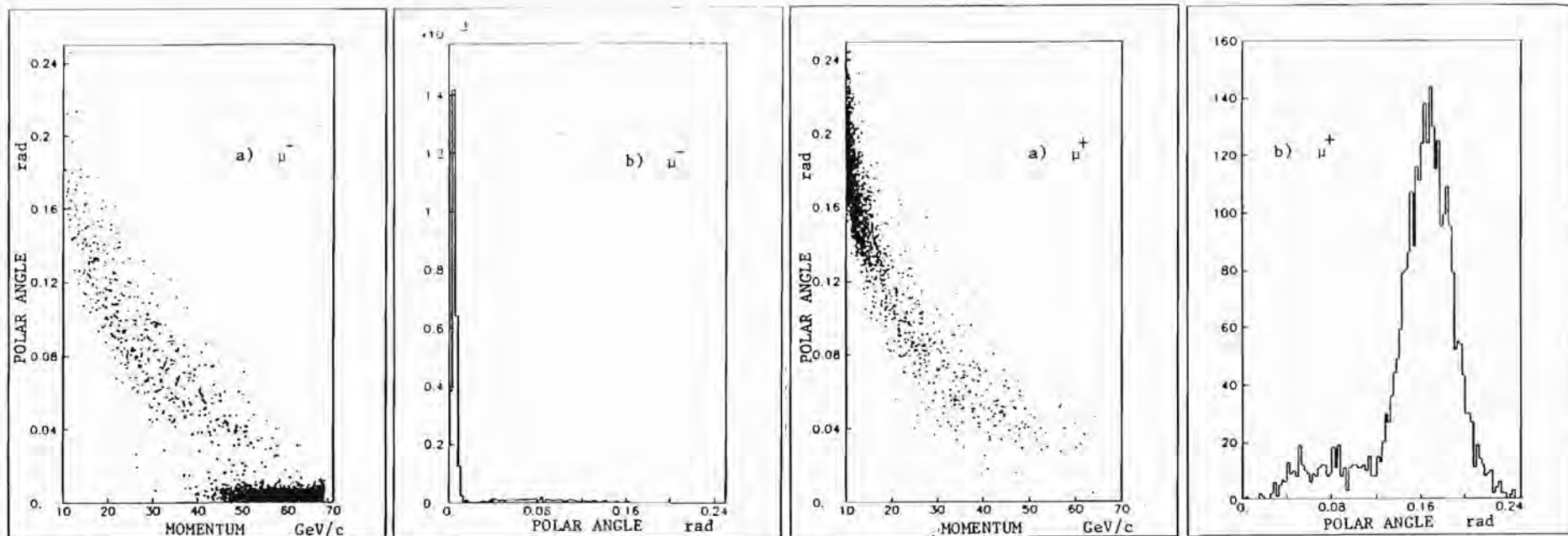
#### 8.1 Elimination of beam-halo

The largest background was due to muons produced in the decay of beam pions. These particles were characterized by a uniform momentum spectrum between 45 and 79 GeV/c, and by angles of the order of 1 mrad from the beam direction. The beam magnets partially suppressed the contribution from low momentum beam muons, while our detector was biased against high momentum muons because of the holes in the  $C$  and the  $D$  scintillator banks (Figures 4.6 and 4.7).

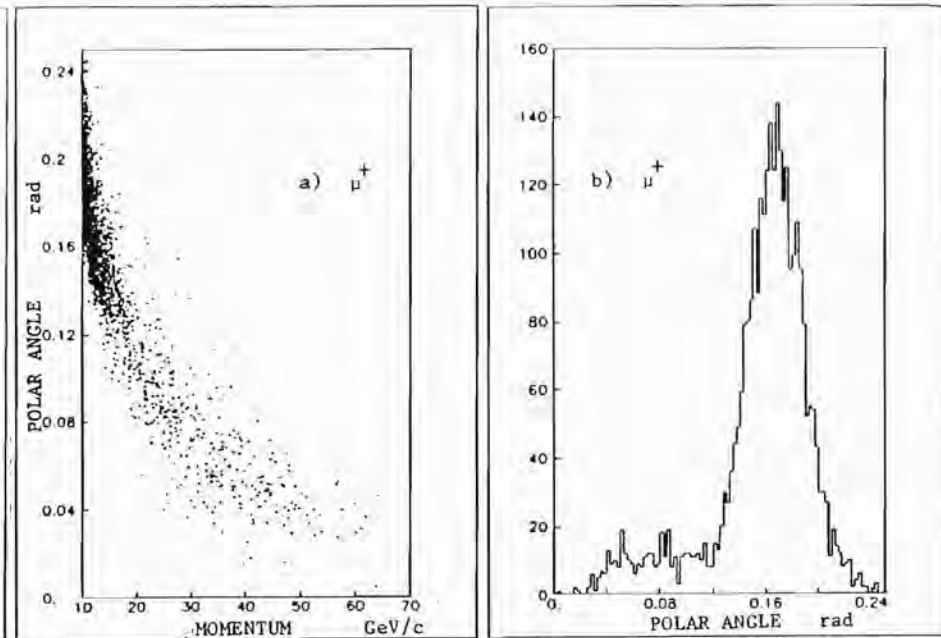
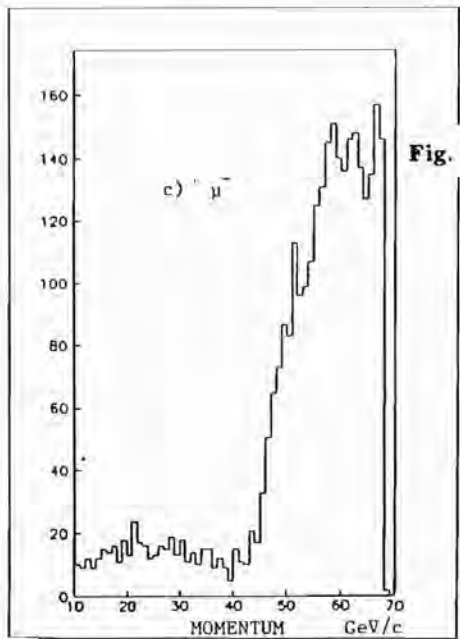
Figure 8.1 shows the scatter plot of the polar angle vs. momentum, with projections, for negative and positive muons from 12% of the collected data. We required  $M_{\mu^+\mu^-} > 4 \text{ GeV}/c^2$ ,  $x_F > 0.15$ , and the other cuts described in the following section. The contamination from large momentum, small angle negative muons (the beam-halo) coupled with low momentum, wide angle positive muons is clearly visible.

The excess low momentum positive muons are presumably due to decays from secondary particles in the hadron absorber. Since the momentum is low, the multiple scattering is large and the vertex fit is not very efficient in rejecting the track.

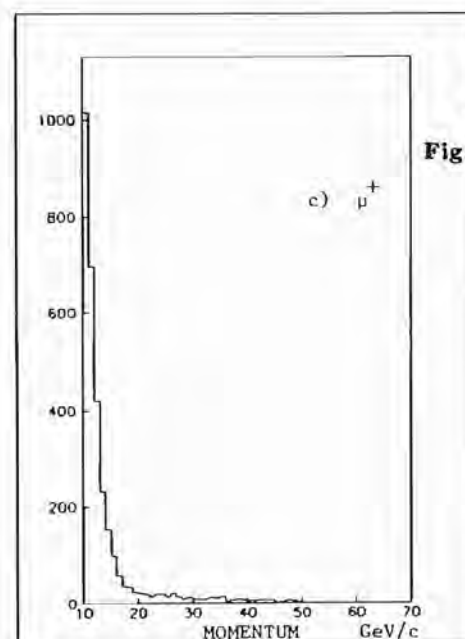
To eliminate this background, we required the initial polar angle



**Fig. 8.1 a,b,c** Momentum vs. polar angle scatter plot, with projections, for **negative muons**, before applying the beam-muon cuts. The sample shown corresponds to 12% of the full data sample.



**Fig. 8.1 d,e,f** Momentum vs. polar angle scatter plot, with projections, for **positive muons**, before applying the beam-muon cuts. The sample shown corresponds to 12% of the full data sample.



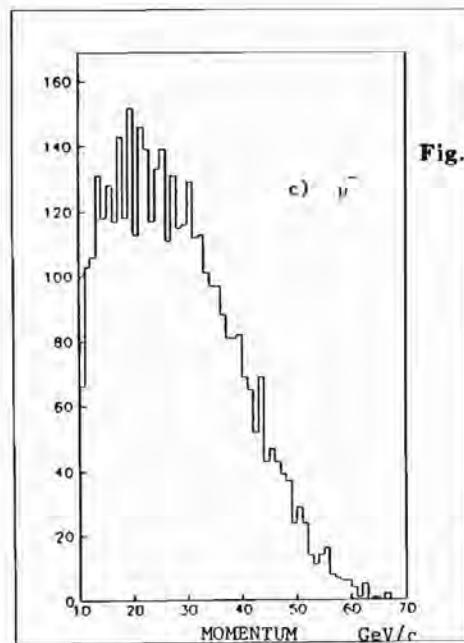
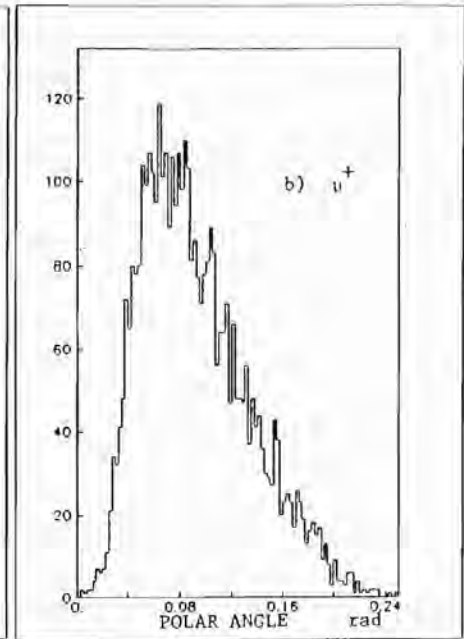
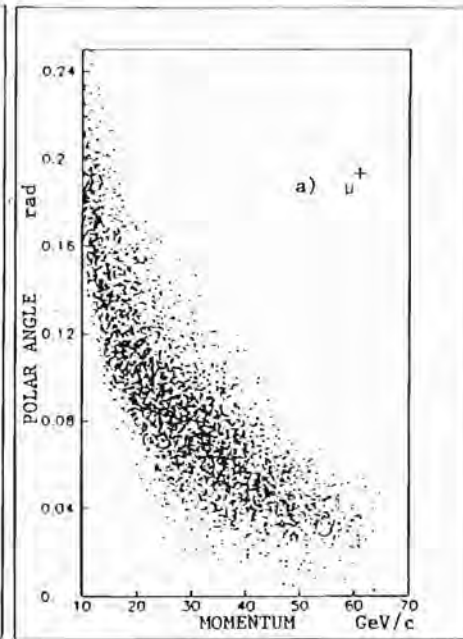
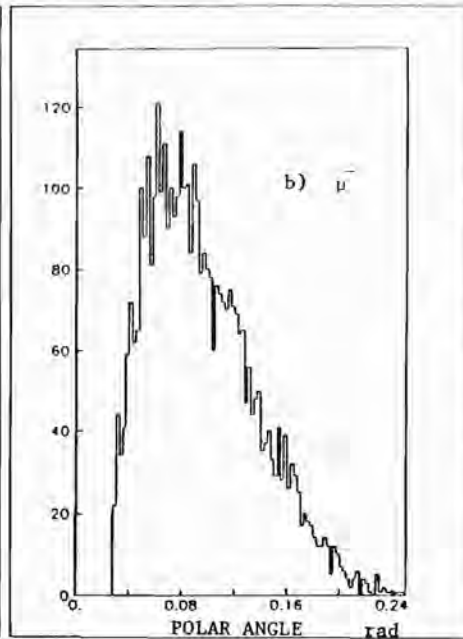
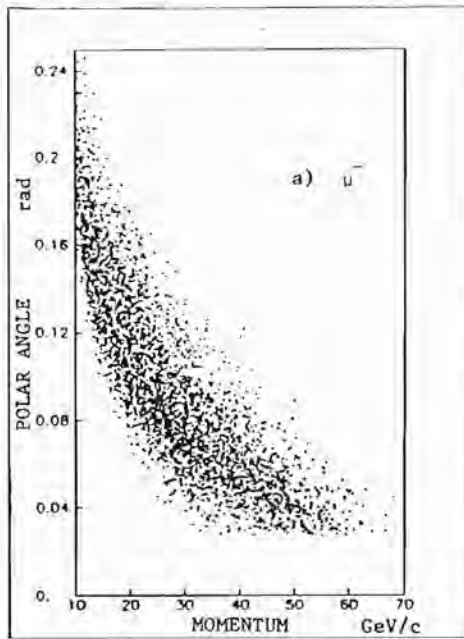


**Fig. 8.2 a,b,c** Momentum vs. polar angle scatter plot, with projections, for **negative muons**, after applying all cuts. The full data sample is shown.

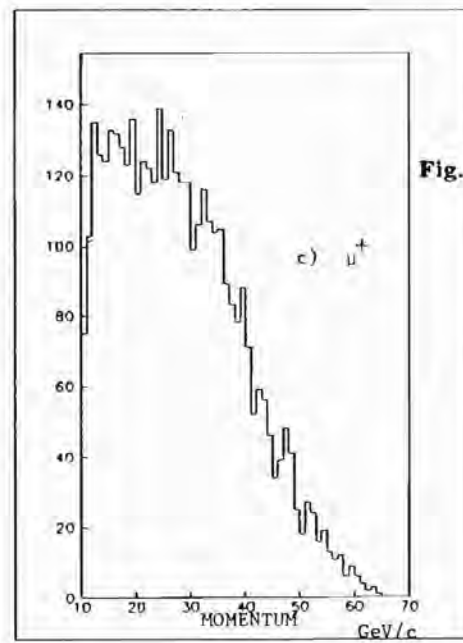


**Fig. 8.2 d,e,f** Momentum vs. polar angle scatter plot, with projections, for **positive muons**, after applying all cuts. The full data sample is shown.

of negative muons to be larger than 28 mrad.

Figure 8.2 shows the polar angle vs. momentum distributions for the full data sample, after adding the halo cut to the other requirements discussed below.

## 8.2 Further event selection

The reconstructed pairs were also selected by the following requirements:

- Track momentum contained in the interval  $10 < P < 68$  GeV/c.
- Vertex fit probability in the bending plane  $P(\chi_{\text{vertex-x}}^2) > 1\%$ .

The reason for using two vertex probabilities is that equation (7.8) can be divided into two independent parts dealing with the track projections onto the two planes  $x-z$  and  $y-z$ . The pair opening angle in the vertical plane was usually about 30–40 mrad, compared to an opening angle in the horizontal plane of the order of 150 mrad. It was therefore much easier to recognize pairs not emanating from the target by looking at the  $x-z$  track projections, and we applied the tighter vertex requirement on  $\chi_{\text{vertex-x}}^2$ .

- Vertex probabilities satisfying:

$$P(\chi_{\text{vertex-x}}^2) > 2\% \quad \text{or} \quad P(\chi_{\text{vertex-y}}^2) > 2\%.$$

- Global fit probabilities for each track larger than 0.1%. This mostly eliminated tracks determined to be out-of-time, which were assigned zero probability by the global fit.
- Each track was required to be matched by hits in all the active banks— $C_x, C_y, C_u, D_x, D_y, D_u, E, F$ . The match between reconstructed tracks and counters took account of limited position resolution and multiple scattering. For each bank we determined a maximum allowed distance between a latched scintillator and the track intercept. That is, if a track crossed the counter very

close to an edge, the scintillator match was still considered valid if the intercepted counter was off, but the neighboring one was on. The allowed distances were small for the upstream  $x$  counters—of the order of 1 mm—, larger for the  $y$  counters, and wide, and momentum dependent, for the  $E$  and  $F$  banks where the multiple scattering was most important. Notice that there were no resolution or alignment problems with the  $u$  counters: following the logic of the trigger, once a pair of  $x$  and  $y$  counters was determined, we required the presence of the only matching  $u$  counter.

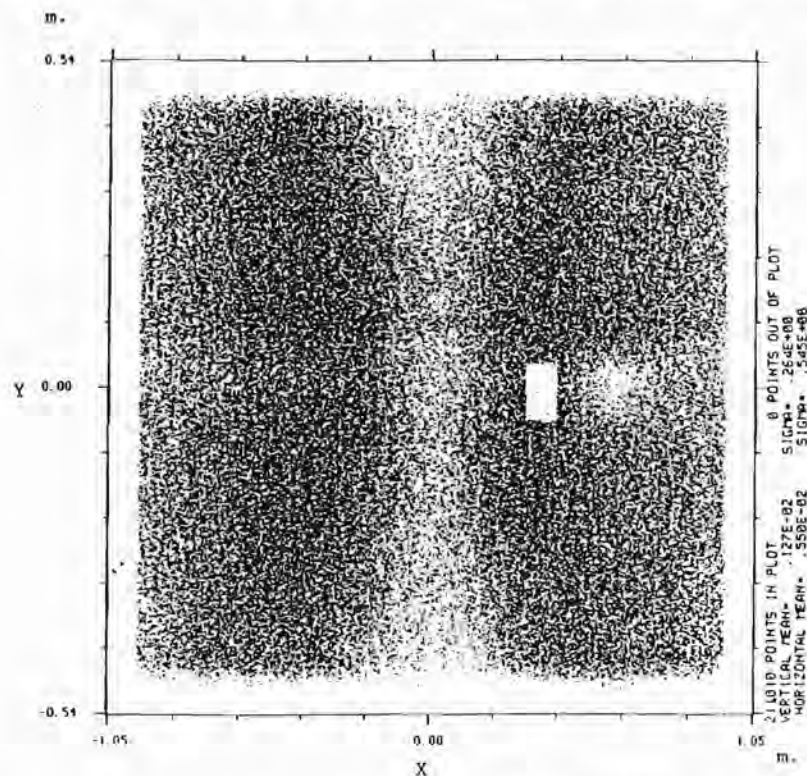
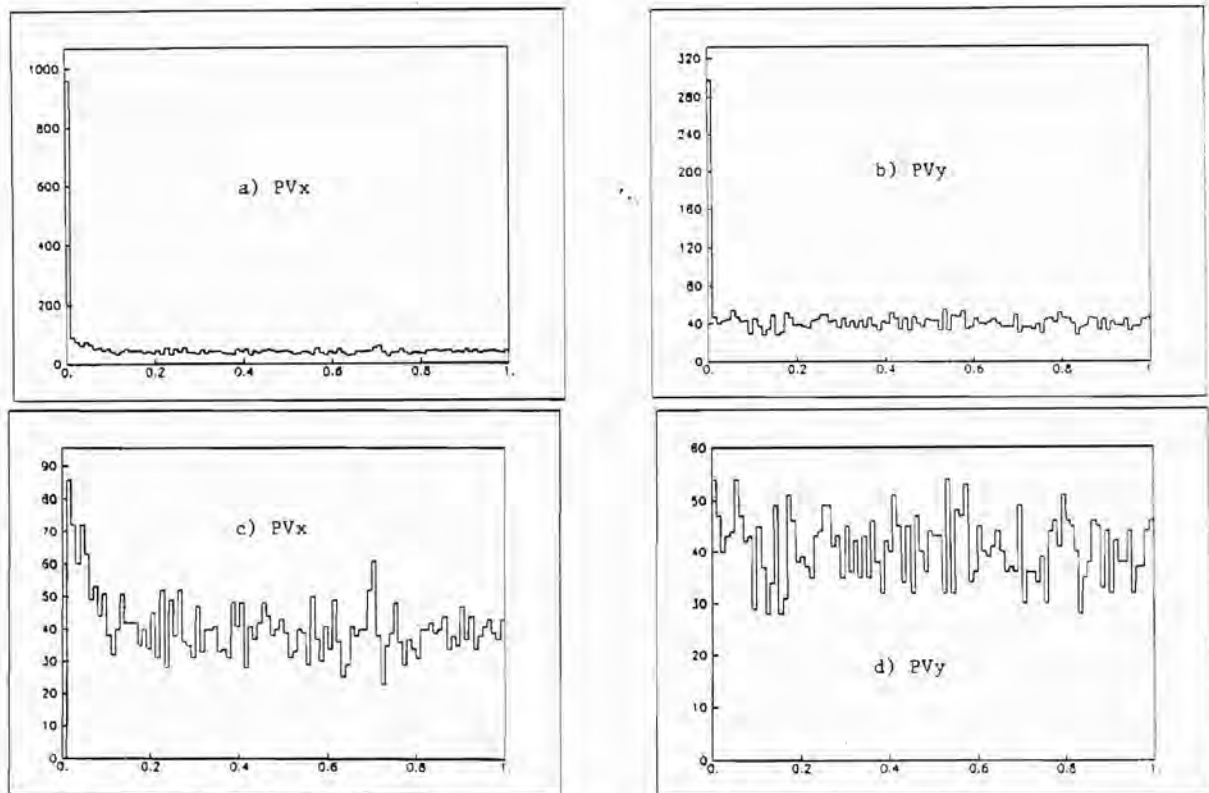
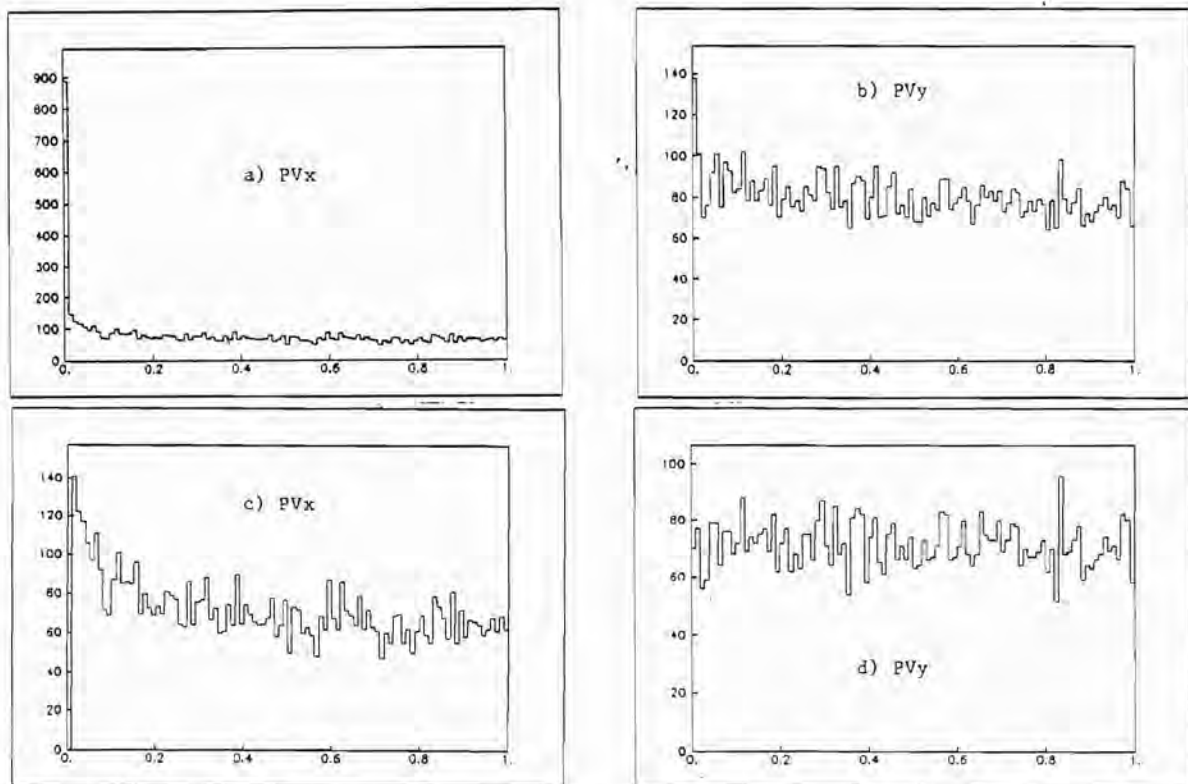


Fig. 8.3 Track illumination of the DC plane no. 5, including all the events with mass larger than  $2.5 \text{ GeV}/c^2$ .



**Fig. 8.4** Vertex probability distributions, in the planes  $x-z$  and  $y-z$ , before (a,b) and after (c,d) applying the  $\chi^2_{vertex}$  cuts.



**Fig. 8.5** Monte Carlo plots for vertex probability distributions, in the planes  $x-z$  and  $y-z$ , before (a,b) and after (c,d) applying the  $\chi^2_{vertex}$  cuts. Compare with Fig. 8.4.

Chapter 9  
MONTECARLO SIMULATION  
AND ACCEPTANCE CORRECTION

- f) Fiducial volume cuts were applied in the magnetic volumes, and fiducial area cuts were made close to the scintillator beam-holes, which were considered larger by 0.5 cm in both directions. Figure 8.3 shows the track distribution on the plane of the DC no. 5, using all the events with  $M > 4 \text{ GeV}/c^2$ . Notice the shadows of the scintillator beam-holes.
- g) The trigger requirements involving the track opening in the vertical plane and the intercept at the  $F$  bank were enforced using the reconstructed pair.

The cuts a), d), f), g) had very limited effects. Each of them alone would eliminate less than 0.5% of the events. Figure 8.4 shows the distribution of the vertex probabilities in the  $x$ - $z$  and  $y$ - $z$  projections, before and after applying the requirements b) and c). Compare with Figure 8.5, obtained from the analysis of events generated by the Montecarlo program.

In order to analyze our data in terms of the Drell-Yan Process, the following requirements were also applied:

- h) Large invariant mass:  $M_{\mu^+\mu^-} > 4.0 \text{ GeV}/c^2$ .
- i) Feynman variable  $x_F > 0.15$ .

These cuts were applied to remove the contamination from resonance production— $J/\Psi$ ,  $\Psi'$ , discussed in Chapter 9—, while the low  $x_F$  region is eliminated because there the acceptance is very low, and the background from pairs produced in interactions of secondary particles is expected to become noticeable.

### 9.1 Description of the method

A Montecarlo simulation was used to compute the geometrical acceptance of the detector and to correct for the effects of detector inefficiency and resolution. We will use the term ‘acceptance’ to mean the combination of these three effects.

The Drell-Yan cross section changes very rapidly within the invariant mass and  $x_F$  range of our geometrical acceptance. The acceptance itself, as shown below in Figures 9.1 to 9.8, is strongly dependent on  $x_F$  and the virtual photon decay angle  $\theta$  (Section 3.6). Under these circumstances, measurement error tends to move events from more populated regions of the phase space into less populated ones. To compensate for this effect, the acceptance correction must satisfy the following two requirements:

- a) high precision in simulating the detector efficiency and resolution;
- b) accuracy in simulating the dependence of events on relevant physical parameters.

In order to satisfy the first requirement, the Montecarlo program simulated the propagation of muons through the apparatus and the detection of tracks in scintillators and wire chambers in great detail.

A data string completely equivalent to the one written by the on-line computer was formed, and subsequently analyzed by the same programs which processed real data.

The second requirement cannot be met with a direct approach, since it apparently requires knowledge of the ultimate result of the acceptance correction before any calculation is actually done. The solution was found by iterating the computation of the acceptance. The first approximation was obtained by generating Montecarlo events according to an extrapolation of previously measured cross sections. The acceptance computed in this way was used to correct our data, which was then used as a better approximation to the cross section in performing a second acceptance calculation. This procedure was repeated several times until the parameters describing the corrected data distributions were equal to the ones used in the acceptance calculation. The consistency of the method was proven by the rapidity of the convergence and the stability of the final result.

The iteration of the acceptance calculation was also made necessary by another aspect of the method we used. This was related to the technical question of how many cells in dimuon phase space could be analyzed in a reasonable amount of computer time. A complete calculation could be obtained by binning events in cells defined in the five-dimensional space of  $M$ ,  $x_F$ ,  $P_T$ ,  $\cos\theta$  and  $\phi$  (or other independent combinations of these variables—involving  $x_1$  and  $x_2$ , for instance).<sup>‡</sup> This method would require a large number of simulated events, and vast amounts of computer memory. Rather than following this approach, we generated events according to the measured distri-

<sup>‡</sup> To describe a pair, we also need a sixth variable, which could be chosen to be the azimuthal angle of  $\vec{P}_T$ . However, since our target was not polarized, the cross section cannot depend on this variable.

butions in all variables, and kept track of the resulting acceptances in various histograms or scatter-plots which did not involve more than three variables.

The results contained in this thesis are the outcome of six iterations of the acceptance computation and cross section calculation. The first Montecarlo program was run with what appeared to be the most reasonable choice of distributions: the events were generated according to differential cross section deduced from scaling, with an angular distribution generated according to complete spin alignment of the virtual photon, and without any  $x_F$  dependence of the transverse momentum. The results of the first iteration showed changes in the angular distribution and average  $P_T$  at large  $x_F$ . The corrected angular and  $P_T$  distributions, together with minor tuning of the mass and  $x_F$  dependence, were used as the input cross sections for the second iteration. Only small corrections were necessary in the following iterations. No meaningful differences in the corrected data were found between the third and fourth steps. The fifth Montecarlo run contained the results of an improved study of the scintillator efficiencies, and also introduced off-shell kinematics for the Fermi motion of the nucleons in the target. Both corrections had minor effects on the cross sections. The sixth Montecarlo run explored the effects of ignoring the nuclear Fermi motion.

## 9.2 Acceptance computation

Following the program described above, we computed the detector acceptance in two or three-dimensional projections of the five-dimensional phase space describing the dimuons. To explain the procedure, let us consider the how the method was applied in the case of a two-dimensional distribution.

We indicate by  $G^n(i, j)$  the number of events generated in the

cell  $(i, j)$  of the  $n$ -th distribution. The Montecarlo program wrote fake data tapes for events within the geometrical acceptance which also satisfied the trigger requirements. The analysis program reconstructed the events, performed cuts according to the criteria discussed in Chapter 8, and filled a corresponding distribution,  $A^n(i, j)$ , with the fully accepted events. Note that the indices describing the reconstructed event need not be the same as those of the generated event due to simulated measurement error.

The analysis program also produced the distribution  $N^n(i, j)$  when applied to real data tapes. The acceptance corrected differential cross section is given by

$$\sigma^n(i, j) = k \times N^n(i, j) \times G^n(i, j) / A^n(i, j) \quad (9.1)$$

We shall discuss the normalization constant  $k$  in Chapter 10. The statistical error is given by:†

$$\Sigma^n(i, j) = \sigma^n(i, j) \times \sqrt{\frac{1}{N^n(i, j)} + \frac{1}{A^n(i, j)}} \quad (9.2)$$

considering fluctuations in both real and simulated data. Notice that the effects of detector resolution such as smearing of the parameters  $i$  and  $j$  are corrected for, since  $N^n$  and  $A^n$  are binned according to reconstructed quantities, which are affected by distortion in the same way in both cases.

The validity of the method depends on a correct parametrization of the cross section in the space orthogonal to the two variables  $(i, j)$ . In order to verify this condition, in each Montecarlo iteration we studied the detector efficiency in many projections, covering the whole phase space with large redundancy. We generally included the

† See item a) in Section 9.3 below.

variable  $x_F$ , or the closely related variable  $x_1$ , among the explicit variables of each distribution. This was done because of the strong dependence of the cross section and of the detector acceptance on these two variables. Integration over  $x_F$  or  $x_1$ , if desired, was performed with cross sections rather than in the acceptance calculation. As a result we obtained rapid convergence of the iterations.

### 9.3 Features of the Montecarlo program

The most important details of the simulation program are listed below.

- a) There was no use of weight functions. Rather the number of events generated was proportional to the probability distribution of each parameter. This allowed a direct estimate of the statistical uncertainties, as in equation (9.2).
- b) The momentum of the beam particles was generated according to the measured spectrum (Section 6.3).
- c) The position of the dimuon production vertex was generated according to the absorption of energetic pions in the target and in the hadron absorber, assuming linear dependence of the Drell-Yan cross section on the atomic number. (See also Section 10.2.)
- d) Fermi motion in nuclei was simulated according to the model of reference 33. The maximum generated momentum was 400 MeV/c. Events were generated with a spectrum of center-of-mass energies taking in account the combined effects of Fermi motion and the energy dependence of the Drell-Yan cross section (Section 9.4).
- e) Multiple scattering and energy loss due to ionization and bremsstrahlung were accounted for in the transport of each particle. Landau-Vavilov fluctuations were simulated.
- f) The magnetic field of the selection magnet was simulated with

14 sections of uniform field, ordered along the longitudinal axis (Figure 4.3). The motion of particles in the spectrometer magnet was approximated by two line segments and a 'kick' of 0.86 GeV/c at the magnet center.

- g) Detection inefficiencies were simulated in each part of the apparatus.

For the wire chambers we used the observed efficiencies averaged over each plane. We also corrected for single channels or groups with anomalous efficiency—about 3% of the total. We corrected for the bias due to the fact that only reconstructed tracks from real data could be used in the measuring the chamber efficiency. Figures 6.4 and 6.5 show the measured efficiency for two chamber planes. As mentioned in Section 4.5, the track reconstruction efficiency was scarcely affected by the small dependence of the chamber efficiency on the particle intensity.

The scintillator efficiency was obtained according to the results of the special-trigger runs described in Section 6.9. The Montecarlo program simulated the inefficiency in the *C*, *D*, *E* and *F* banks using two-dimensional efficiency tables, with 12 horizontal rows and 14 to 22 vertical columns. The values in these tables were based on the observed inefficiencies in runs taken with typical beam intensity.

- h) The simulation program wrote fake data tapes which were analyzed by the same programs which performed the real data analysis.
- i) The physical quantities describing the pair are generated according to the measured spectra. In particular, the angular distributions are generated in the *t*-channel (Gottfried-Jackson frame)

according to:

$$\frac{d\sigma}{d\Omega} \propto 1 + \lambda \cos^2 \theta \quad (9.3)$$

where  $\lambda$  is function of  $x_T$ , as discussed in Chapter 13. The transverse momentum is generated with the spectrum:

$$\frac{d\sigma}{dP_T} \propto \frac{P_T}{(1 + (P_T/A)^2)^6} \quad (9.4)$$

where the parameter  $A$  depends on the generated  $x_F$  (Chapter 14).

- j) To allow for smearing due to limited detector resolution and variations of the total energy and momentum due to Fermi motion, the Montecarlo program was generally used to simulate events with mass larger than 3.5 GeV/c<sup>2</sup> and  $x_F$  larger than -0.2. As noted in Section 8.2, our final sample considered only events with  $M > 4.0$  GeV/c<sup>2</sup> and  $x_F > 0.15$ .

#### 9.4 Fluctuations in the center-of-mass energy

The Fermi motion of nucleons in the target introduced fluctuations in the center-of-mass energy, which were taken into account by the simulation program.

The cross section dependence on the mass of the lepton pair was parametrized using the empirical relation

$$\frac{d\sigma}{dM} \propto e^{-\alpha M} \quad , \quad (9.5)$$

which is well approximated by our data, with  $\alpha \simeq 1.4$ . The dependence on the center-of-mass energy  $\sqrt{s}$  can be found by comparing with the scaling relation:

$$\frac{d\sigma}{dM} = \frac{1}{M^3} f(\tau) \quad (9.6)$$

which is obtained by integrating equation (2.10) over  $x_F$ . Then recalling that  $\tau = M^2/s$  we may write

$$\frac{d\sigma}{dM} \propto \frac{s_0^{1.5}}{s^{1.5}} e^{-\alpha\sqrt{s_0}\tau} \Rightarrow \frac{d\sigma}{d\tau} \propto \frac{1}{s} e^{-\beta\tau} \quad (9.7)$$

where  $\beta = \alpha\sqrt{s_0}$  and  $\sqrt{s_0}$  is the average center-of-mass energy used in the event analysis. The cross section for  $M > M_0$  is given by the integral:

$$\int_{M_0/\sqrt{s}}^{\infty} \frac{1}{s} e^{-\beta\tau} d\tau = \frac{1}{\beta s} e^{-\beta M_0/\sqrt{s}} \quad (9.8)$$

The simulation program folded this expression with the distribution of beam momentum and of the nuclear Fermi motion, obtaining a probability distribution used for generating events.

### 9.5 Detector acceptance and losses due to cuts

The acceptance for events with mass larger than 4 GeV/c<sup>2</sup>,  $x_F$  larger than 0.15 is shown in Figures 9.1 to 9.8. The acceptance is given in units of 10<sup>-3</sup>.

The acceptance calculation simulates events generated both in the target and in the hadron absorber. Particular studies established that events from the two sources are characterized by a very similar geometrical and trigger acceptance, about 2%, but the vertex cut (Section 7.7) is able to reject about 80% of the absorber events. The resulting loss of events generated in the target is estimated to be 4%, which is larger than the nominal 1% cut (Section 8.2b) because of the target's finite length, its location in the magnetic fringing field, and because of large fluctuations in the energy loss. These effects reduce the quality of the transport equations (7.9), and produce a larger  $\chi_{vertex}^2$ . This causes the increase in population at low  $\chi^2$  probability seen in Figures 8.4.c and 8.5.c.

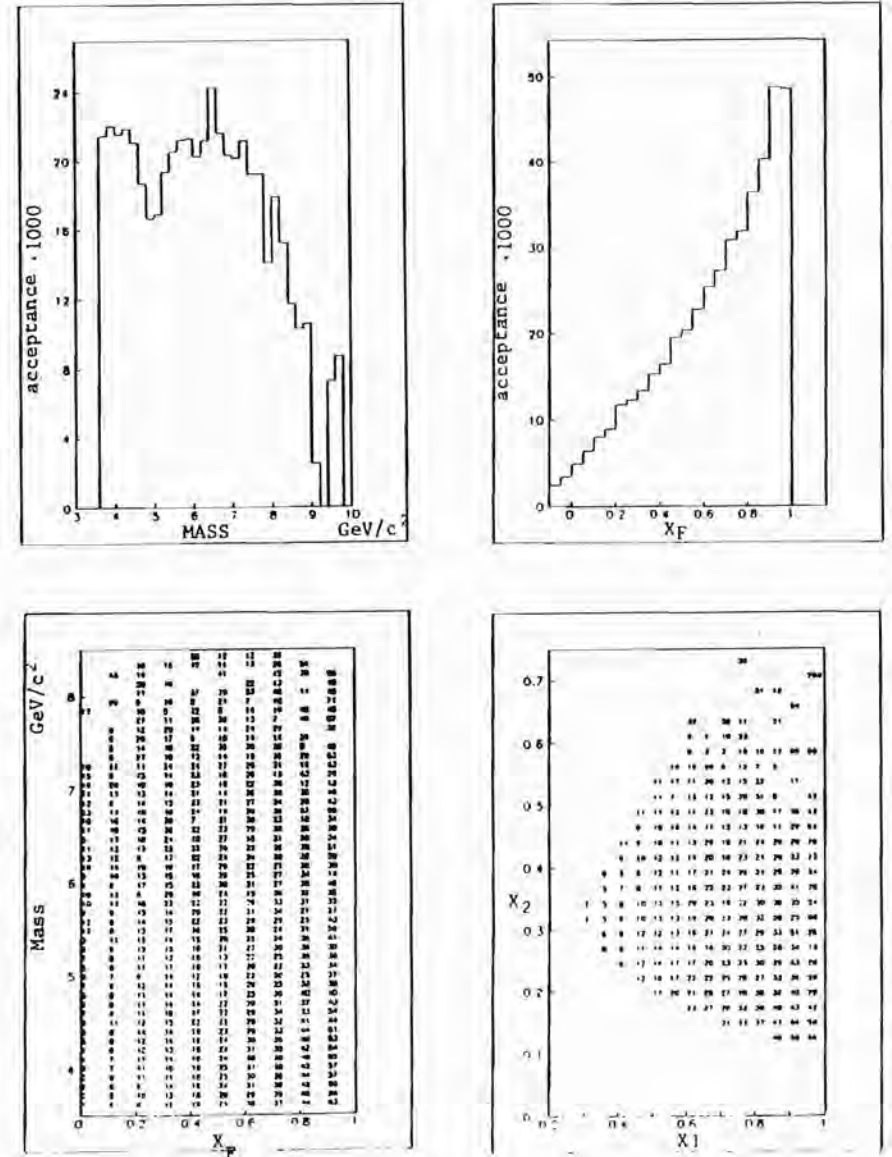


Fig. 9.1-4 Detector acceptance in units of 10<sup>-3</sup>:

- 9.1)  $\epsilon$  vs. mass                      9.2)  $\epsilon$  vs.  $x_F$   
 9.3)  $\epsilon$  vs.  $x_F$ , mass                9.4)  $\epsilon$  vs.  $x_1, x_2$

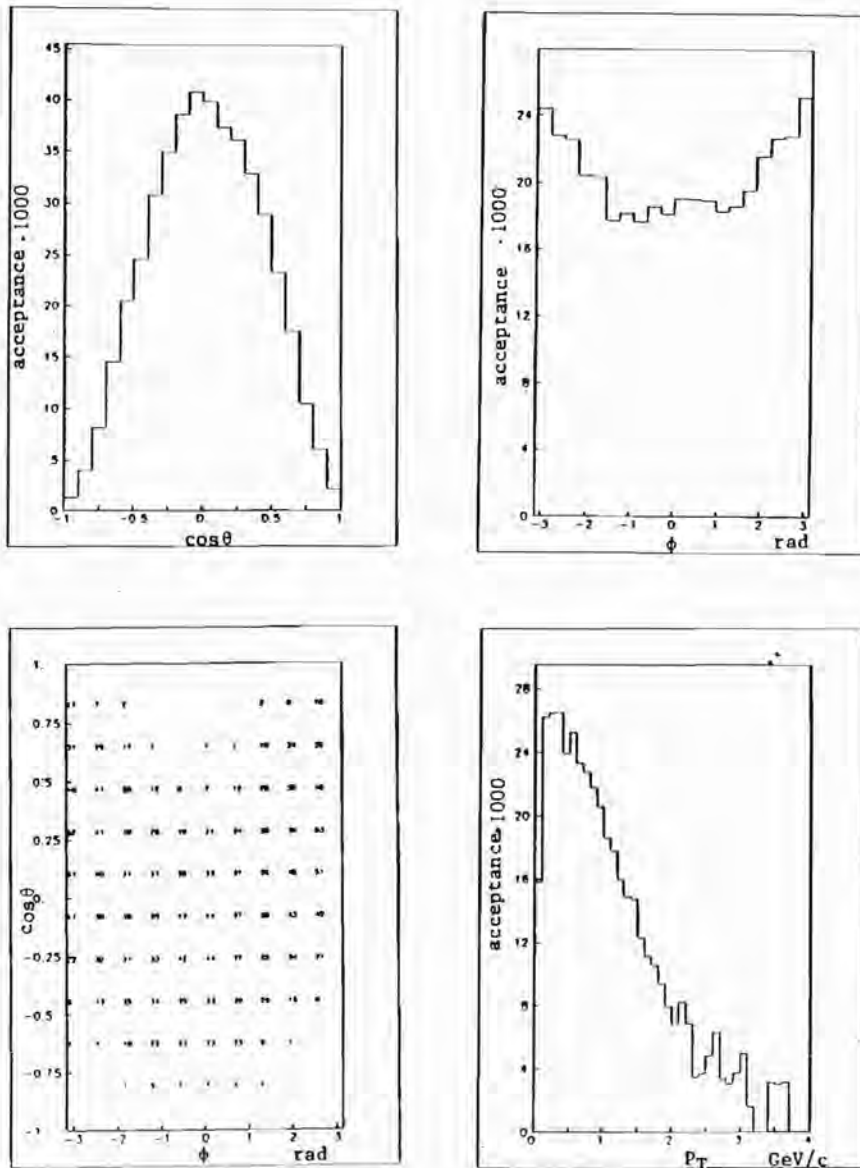


Fig. 9.5-8 Detector acceptance in units of  $10^{-3}$ .

9.5)  $\epsilon$  vs.  $\cos\theta_t$       9.6)  $\epsilon$  vs.  $\phi_t$   
 9.7)  $\epsilon$  vs.  $\phi_t, \cos\theta_t$       9.8)  $\epsilon$  vs.  $P_T$

The Montecarlo program evaluated the loss of Drell-Yan events due to the beam-halo cuts to be about 2%; the same fraction was lost due to the fiducial volume cuts (Section 8.2f).

The loss due to scintillator inefficiency is beam intensity dependent, as discussed in Chapter 5. A similar, but smaller intensity dependence affects the track reconstruction. § We shall discuss how to deal with these effects in Chapter 10.

### 9.6 Measurement resolution

The Montecarlo program was also used to estimate the resolution in measuring the parameters describing a lepton pair. The results of this study are listed below, expressed in terms of r.m.s. errors.

$M$  :  $\sigma = .14 \text{ GeV}/c^2$ , determined by the multiple scattering in the hadron absorber;

$x_F$  :  $\sigma = .04$ , increasing to .05 for  $x_F \approx 0.2$ ;

$x_1$  :  $\sigma = .03$ ;

$x_2$  :  $\sigma = .03$  at  $x_2 = 0.2$ ,

$\sigma = .05$  at  $x_2 = 0.4$ ;

$P_T$  :  $\sigma = .13 \text{ GeV}/c$ ;

$\cos\theta_t$  :  $\sigma = .07$  at  $\cos\theta_t = 0$ ,

$\sigma = .05$  at  $|\cos\theta_t| = 0.5$ .

The resolution in measuring the pair invariant mass was confirmed in data analysis by the observation of the width of the  $J/\psi$  peak.

§ Visual scanning of several hundred of triggers confirmed this result suggesting that the track reconstruction inefficiency was about 2-3% at high intensity.

Good consistency was also found in  $\sigma(x_F)$  for  $x_F \simeq 1$ , where the Montecarlo correctly reproduced the fraction of events reconstructed with  $x_F > 1$ . The uncertainty in this variable is mostly due to the width of the beam momentum spectrum rather than to the resolution in measuring the momentum of the muon pair.

### 9.7 Contamination from resonance production

The Montecarlo program was also used to study the detection of  $J/\Psi$  particles. We estimated how many of them would enter our final sample with mass larger than  $4 \text{ GeV}/c^2$  because of limited detector resolution.

Out of 4500 reconstructed  $J/\Psi$  pairs from the simulation, 8 appeared beyond  $3.7 \text{ GeV}/c^2$ , and none over  $4 \text{ GeV}/c^2$ . Our real sample contains about 60000  $J/\Psi$ 's, and we estimate an upper limit of about 30  $J/\Psi$  events affecting our final sample, with 90 % confidence level.

A similar estimate has been made for the  $\Psi'$  resonance. Preliminary analysis of our data suggests that the  $\Psi'$  is produced at 2.5 % of the rate of the  $J/\Psi$ . The resulting contamination beyond  $4.0 \text{ GeV}/c^2$  should be about 40 events, 1 % of the total final sample.

Notice that if the resolution shape of our detector were gaussian, we would obtain smaller contamination at larger masses. About 0.2 % of the  $J/\Psi$ 's appear with mass larger than  $3.7 \text{ GeV}/c^2$ , while a gaussian resolution would imply twenty times fewer events in this region. The high mass tail is due to the events produced in the absorber. The transport equations (7.9) overestimate the amount of bending for tracks which are produced inside the magnet but are analyzed as coming from the target. The effect is in part counterbalanced by the geometrical constraint of the production vertex, but the net result is a bias toward larger initial polar angles, and hence larger mass.

### 9.8 Data and Montecarlo detector illumination

Figures 9.9 to 9.11 show a comparison of scintillator bank illuminations between simulated and real data, for events with invariant mass larger than  $4 \text{ GeV}/c^2$ , and  $x_F$  larger than 0.15. Each figure is based on events from a different interval of momentum of one muon, and shows the distribution of the  $x$  intercept at the  $C$  and  $D$  banks, and the  $y$  intercept at the  $C$  bank. Data are shown with error bars, and Montecarlo results with dotted lines. The number of Montecarlo events is 3.5 times larger than that of the data sample.

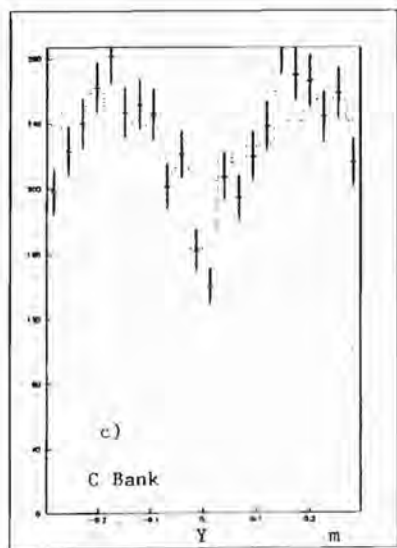
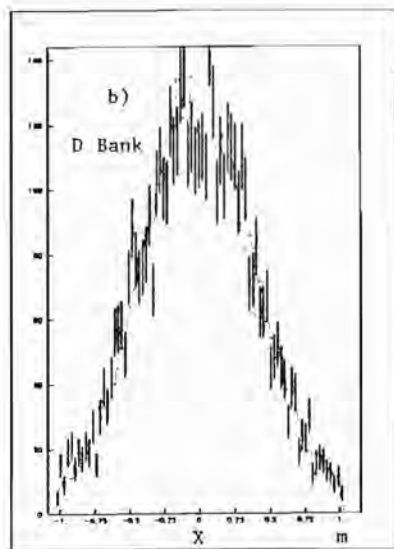
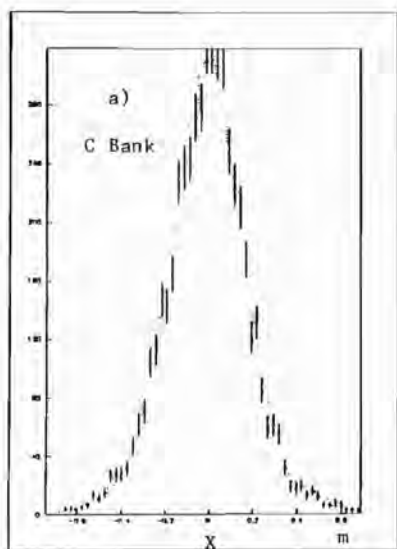


**Fig. 9.9** Illumination of the detector by tracks with momentum  $10 < P < 25 \text{ GeV}/c$ .  
 a)  $x$  intercept at the  $C$  bank;  
 b)  $x$  intercept at the  $D$  bank;  
 c)  $y$  intercept at the  $C$  bank.  
 Data points are shown with error bars; the dotted lines are generated by the Monte-carlo program.

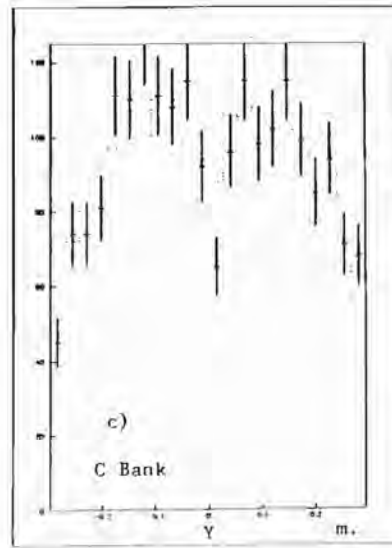
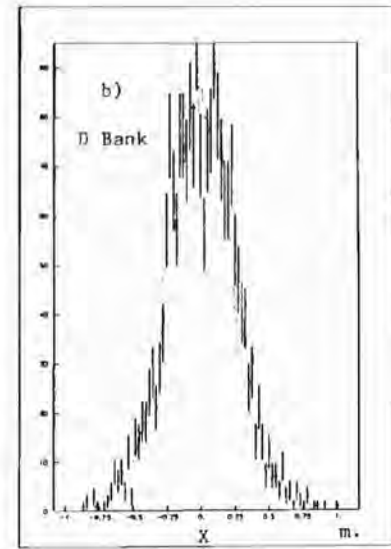
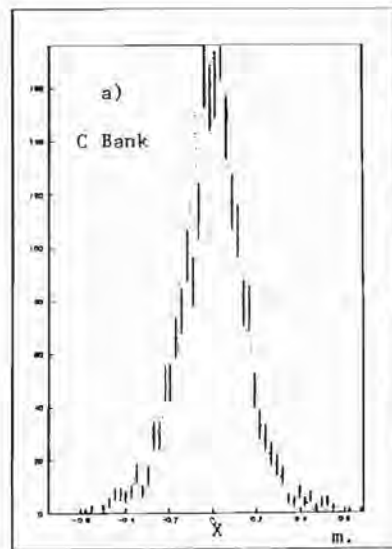


**Fig. 9.10** Illumination of the detector by tracks with momentum  $25 < P < 40 \text{ GeV}/c$ .  
 a)  $x$  intercept at the  $C$  bank;  
 b)  $x$  intercept at the  $D$  bank;  
 c)  $y$  intercept at the  $C$  bank.  
 Data points are shown with error bars; the dotted lines are generated by the Monte-carlo program.

## Chapter 10

### CROSS SECTION NORMALIZATION

#### 10.1 Chapter outline

We shall discuss the absolute normalization of our study of muon pair production. Our goal is to identify the various terms in the equation:

$$\frac{d\sigma^{DY}}{dX} = \frac{dN^{DY}}{dX} \frac{1}{\varepsilon(X)} \frac{\sigma^{abs}}{N^\pi} \quad (10.1)$$

where  $X$  is a vector in the space of the variables of physical interest,  $\varepsilon$  is the detector acceptance corrected for inefficiency,  $\sigma^{abs}$  is the effective absorption cross section for the entire target, and  $N^\pi$  is the total number of collected beam particles, corrected for detector dead-time.

#### 10.2 Effective absorption cross section and acceptance

The absorption cross section per nucleus for energetic pions has been measured in references 34 and 35. The dependence on the atomic number is given by<sup>30</sup>:

$$\sigma_A^{abs} = 25.9 A^{0.762} \text{ mbarn} \quad (\pm 3\%) \quad (10.2)$$

Our target was 97.2% tungsten by weight (Table I in Chapter 4). The intermediate elements forming 2.8% by weight of the target can be well represented by a nominal element with  $A = 60$ . Computing the

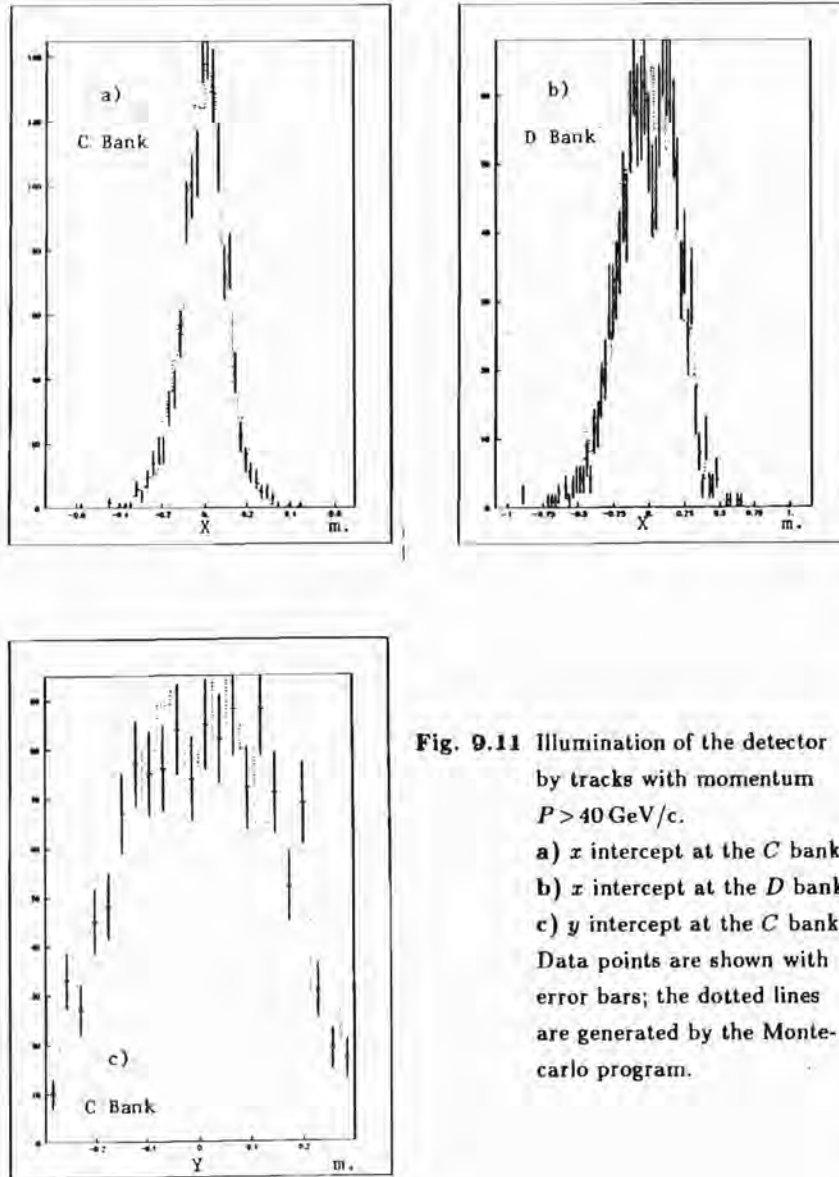


**Fig. 9.11** Illumination of the detector by tracks with momentum  $P > 40 \text{ GeV}/c$ .  
 a)  $x$  intercept at the  $C$  bank;  
 b)  $x$  intercept at the  $D$  bank;  
 c)  $y$  intercept at the  $C$  bank.  
 Data points are shown with error bars; the dotted lines are generated by the Monte-carlo program.

numerical density  $n$  of these nuclei, and using the equation above, we obtain the average absorption cross section per nucleus in our target:

$$\begin{aligned}\sigma^{abs}_t &= \frac{1}{n_t} (n_W \sigma^{abs}_W + n_{60} \sigma^{abs}_{60}) \\ &= 0.919 \sigma^{abs}_W + 0.081 \sigma^{abs}_{60} = 1.31 \text{ barn} \quad (10.3)\end{aligned}$$

The absorption length in the target is given by:

$$\frac{1}{\lambda_t} = n_t \sigma^{abs}_t = n_W \sigma^{abs}_W + n_{60} \sigma^{abs}_{60} = \frac{1}{11.90 \text{ cm}} \quad (10.4)$$

Since our target was 20.32 cm long, we obtain that 81.9% of the pions interacted inelastically. The remaining 18.1% of the pions were absorbed in the beryllium absorber, with cross section per nucleus given by:

$$\sigma^{abs}_{Be} = .138 \text{ barn}. \quad (10.5)$$

The total number of detected Drell-Yan events, including those produced by pions which interacted in the absorber, can be written in the following way:

$$\frac{dN^{DY}}{dX} = N^\pi \left( .819 \frac{d\sigma^{DY}}{dX_t} \frac{\epsilon_t}{\sigma^{abs}_t} + .181 \frac{d\sigma^{DY}}{dX_a} \frac{\epsilon_a}{\sigma^{abs}_a} \right) \quad (10.6)$$

where  $a$  indicates 'absorber', and  $t$  stands for 'target'. We have not indicated the dependence of the acceptance  $\epsilon$  on the physical parameters  $X$  and the interaction coordinates  $\vec{x}$ .

It has been experimentally observed that the Drell-Yan cross section in nuclei is proportional to the atomic number<sup>18</sup>, so that we can write equation (10.6) in the form:

$$\begin{aligned}\frac{dN^{DY}}{dX} &= N^\pi \left( .819 (183.85 \times .919 + 60 \times .081) \frac{\epsilon_t}{\sigma^{abs}_t} + \right. \\ &\quad \left. + .181 \times 9.01 \frac{\epsilon_a}{\sigma^{abs}_a} \right) \frac{d\sigma^{DY}}{dX} \\ &= N^\pi (108.6 \epsilon_t + 11.81 \epsilon_a) \frac{d\sigma^{DY}}{dX} \text{ barn} \quad (10.7)\end{aligned}$$

The Drell-Yan cross section is now measured **per nucleon**. Notice that the linear  $A$ -dependence reduces the fraction of events produced in the absorber to only 9.8% of the total.

The Montecarlo program generated dimuon production vertices according to equation (10.7). Therefore the calculation of the acceptance discussed in Chapter 9 performed an average of the efficiency, providing us with an effective acceptance  $\epsilon(X)$ :

$$\frac{dN^{DY}}{dX} = N^\pi \frac{d\sigma^{DY}}{dX} \frac{120.4 \epsilon(X)}{\text{barn}} = N^\pi \frac{d\sigma^{DY}}{dX} \frac{\epsilon(X)}{8.305 \text{ mbarn}} \quad (10.8)$$

Comparing with equation (10.1) we identify 8.305 mbarn as the total absorption cross section per nucleon of our target.

### 10.3 Beam intensity dependence

In principle, the Drell-Yan cross section could be obtained by normalizing our data sample on a run by run basis, comparing the yield of high mass pairs with the beam intensity measured by the ionization chambers (Section 6.4), corrected for the detector dead-time. However, already during the data taking we found evidence that the detector performance was affected by the large beam intensity. The trigger rate appeared to saturate for intensities larger than  $5 \times 10^9$  pions per spill, and the off-line analysis showed that the yield of Drell-Yan events was already approaching saturation for intensities

of  $4-5 \times 10^9$ , not much larger than the typical values  $3-4 \times 10^9$ . Furthermore, the comparison with the yield found for special runs at low intensity ( $4-6 \times 10^8$  pions per spill) showed that the number of events collected at high intensity was only about 60% of what expected from the low intensity runs, even after correcting for the detector dead-time. The latter was 35% on average.

This inefficiency was mostly due to pile-up effects in the scintillators (Section 6.9), which accounted for about a 25% loss, as we shall see below. The remaining inefficiency was presumably due to a number of different reasons, including the difficulty in measuring the actual dead-time and effective number of collected beam particles, due to intensity structure during a spill. Other significant losses were presumably due to the trigger multiplicity cuts (Sections 5.2, 5.3), and to the various event length cuts applied by the off-line program (Section 7.2). Some intensity dependence can also be attributed to the efficiency of the track reconstruction.

A direct approach to the normalization problem requires the detailed study of these effects, some of which were not directly measurable. Rather than follow this program, we undertook an approach based on the comparison between the full data sample, and the sample collected in the low intensity runs.

The number of high mass events collected at low intensity is too small to allow studies of intensity dependent effects, but the sample of  $J/\Psi$ 's is large enough for this purpose.

Following this program, we rewrite equation (10.1), considering the three different cases of the Drell-Yan process, and  $J/\Psi$  production at low and high intensity:

$$\begin{aligned} \frac{d\sigma^{DY}}{dX} &= \frac{dN^{DY}}{dX_{hi}} \frac{1}{\varepsilon(X)_{hi}} \frac{\sigma^{abs}}{N^{\pi_{li}}} \\ \frac{d\sigma^{J/\Psi}}{dY} &= \frac{dN^{J/\Psi}}{dY_{hi}} \frac{1}{\varepsilon(Y)_{hi}} \frac{\sigma^{abs}}{N^{\pi_{li}}} \\ \frac{d\sigma^{J/\Psi}}{dZ} &= \frac{dN^{J/\Psi}}{dZ_{li}} \frac{1}{\varepsilon(Z)_{li}} \frac{\sigma^{abs}}{N^{\pi_{li}}} \end{aligned} \quad (10.9)$$

where  $hi$  and  $li$  stand for 'high intensity' and 'low intensity'.

The acceptance/efficiency  $\varepsilon$  can be expressed as a product of the acceptance  $\varepsilon^o(X)$  calculated by the Montecarlo program, and a factor  $\varepsilon^*$  which does not depend on the measured quantities  $X$ :

$$\varepsilon(X) = \varepsilon^o(X) \cdot \varepsilon^* \quad (10.10)$$

Both  $\varepsilon^o$  and  $\varepsilon^*$  depend on the beam intensity, but  $\varepsilon^*$  is expected to be the same for Drell-Yan and  $J/\Psi$  events at a given beam intensity. The factor  $\varepsilon^*$  includes such global effects as dead time, trigger losses and multiplicity cuts mentioned above. We define  $\varepsilon^*$  to be 1 at low intensity. Recall that the Montecarlo calculation of  $\varepsilon^o$  uses the knowledge of local intensity dependence of the scintillator efficiency as obtained in special-trigger runs.

Using the second and third equations in (10.9), we obtain the total number of pions at high intensity multiplied by  $\varepsilon^*$ :

$$\varepsilon^* N^{\pi_{hi}} = N^{\pi_{li}} \left( \frac{dN^{J/\Psi}}{dY_{hi}} \frac{1}{\varepsilon^o(Y)_{hi}} \right) \left( \frac{dN^{J/\Psi}}{dZ_{li}} \frac{1}{\varepsilon^o(Z)_{li}} \right)^{-1} \quad (10.11)$$

In order to exploit the maximum statistical power, we integrate over the space of the dynamical variables, obtaining:

$$\varepsilon^* N^{\pi_{hi}} = N^{\pi_{li}} \left( \frac{N^{J/\Psi}_{hi} \langle \varepsilon_{li}^o \rangle^{J/\Psi}}{\langle \varepsilon_{hi}^o \rangle^{J/\Psi} N^{J/\Psi}_{li}} \right) \quad (10.12)$$

For the  $J/\Psi$  sample we used pairs with  $2.5 < M < 4.5$ ,  $x_F > 0.3$ . The efficiency  $\varepsilon^\circ$  was calculated to be 1.69% at low intensity, and 1.22% at high intensity. † We detected 1040 events in the former case, and 103269 in the latter, so that

$$\varepsilon^* N^{\pi}_{hi} = 138.4 N^{\pi}_{li}. \quad (10.13)$$

We can now write equation (10.1) in the new form:

$$\frac{d\sigma^{DY}}{dX} = \frac{dN^{DY}}{dX}_{hi} \frac{1}{\varepsilon^\circ(X)_{hi}} \frac{60.0 \text{ nbarn}}{N^{\pi}_{li}}. \quad (10.14)$$

#### 10.4 Beam flux normalization

The beam flux was measured by ionization chambers that were mentioned in Section 6.4. One of the two chambers with five rings was located only about 2 m upstream of our target. We used the inner four rings (labelled ION #8-11 in Table VII) of this ion chamber, which covered the same area as and were aligned with our target, to compute the beam exposure.

The outer ring typically counted 15% of the rate of the whole chamber. We did not include this rate in the normalization, and did not simulate corresponding beam particles in the Montecarlo program. The outer ring covered 90% of the total area of the ion chamber, and was greatly affected by beam-halo and particles backscattered from the target. Using a gaussian approximation for the beam shape,

† The computation was done using the Montecarlo program with the scintillator efficiency values measured by the techniques described in Section 6.9. We do not have precise measurements of the inefficiencies at low intensity for all the banks, but they are small, as shown in Figure 6.5.

and extrapolating from the inner four rings to the outer one, less than  $\frac{1}{3}$  of the observed rate on the outer ring is accounted for. As a further argument for neglecting the counts in the fifth ring, data taken with anomalous beam tuning showed event yields compatible with the rate measured in the inner rings, while the rate in the fifth ring was unusually large. Beam particles which passed through the fifth ring missed the target and directly struck the beryllium absorber. Hence this effect could be partly due to the lower Drell-Yan production rate in the low-Z absorber, and to the effect of the vertex-cut, but both reasons actually add confidence that we should disregard the count rate in the outer ring.

The behavior of the ion chambers at different intensities appeared to be consistent with the rate measured in scintillator banks. Particularly, we found good agreement with the rate measured in the  $F$  bank.

The normalization of the ion chambers was obtained on various occasions by placing copper foils near the ion chambers, and studying the production of  $^{24}\text{Na}$ , detected afterwards through radioactive decays. The results of the various foil excitation calibrations which were performed are given in Table VII. Not all the measurements appear to be consistent with each other; the most anomalous one was made during the test-run in 1982, and it is conceivable that some chamber parameters might have been changed since then, and that some interpretation errors, which are now not easily traced, might have occurred.

I shall use the value of

$$1.2 \times 10^4 \text{ pions/count} \quad (10.15)$$

for the ion chamber normalization, which is the average of the calibration results obtained with the beam momentum at 80 GeV/c. This

**Table VII** Results of the ion chamber calibrations performed with copper foil activation.

ION CHAMBER CALIBRATION			
DATE	BEAM(GeV/c)	ION #*	PARTICLES/10 <sup>4</sup> Counts
6/82	260 π <sup>-</sup>		1.74 ± .12
12/14/83	80 π <sup>-</sup>	2,3,4	1.23 ± .06
		5	1.23 ± .11
		8,9,10	1.31 ± .09
		11	1.18 ± .14
2/6/84	80 π <sup>-</sup>	2,3,4,5	1.10 ± .06
		8,9,10,11	1.16 ± .08
6/11/84	250 π <sup>-</sup>	2,3,4	1.54 ± .09
		5	1.20 ± .07
6/25/84	250 π <sup>-</sup>	2,3,4	1.05 ± .06
		5	0.91 ± .08
		8,9,10	1.07 ± .07
		11	1.00 ± .06
7/16/84	250 π <sup>+</sup> p <sup>**</sup>	2,3,4	1.68 ± .12
		5	1.34 ± .06
		8,9,10	1.71 ± .08
		11	1.41 ± .10

\* ION CHAMBERS 8-11 were the four rings aligned with the target

\*\* 58% π<sup>+</sup>(K<sup>+</sup>), 42% p

value is presumably correct to 10% accuracy.

This figure has been confirmed by a study based on the data collected during the beam spectrum measurement. All the beam was counted by scintillators, which allowed us to fix the normalization of the rate in the *F* bank. A direct normalization of the ion chambers was not possible during these measurements because the intensity was too low for the ion chamber to count, but it was possible to infer the normalization value at higher intensity by comparison with the bank of scintillators. The result was  $1.1 \times 10^4$  pions/count, with an error estimated to be of the order of 10%.

Using the normalization value quoted above, we found the effective number of pions collected at low intensity, corrected for 5.0% detector dead time:

$$N_{hi}^{\pi} = 2.471 \times 10^7 \cdot 0.95 \cdot 1.2 \times 10^4 = 2.82 \times 10^{11}. \quad (10.16)$$

To conclude this section, it is interesting to estimate the value of  $\epsilon^*$  and  $N_{hi}^{\pi}$ . This can be done by recalling the 40% loss of events at high intensity, exclusive of dead-time effects, mentioned at the beginning of Section 10.3. We factor out the loss due to  $\epsilon^0(X)$  using the values obtained for the  $J/\Psi$  events, namely  $1.22/1.69 = .7$ . Thus our first estimate is  $\epsilon^* \simeq .83$ . Then correcting for the 65% live-time we have  $\epsilon^* \simeq .54$ . Combining equations (10.13) and (10.16) we estimate  $N_{hi}^{\pi} \simeq 7.2 \times 10^{13}$ . This is to be compared with the value  $7.85 \times 10^{13}$  obtained directly from the ion chambers, integrating over the whole run.

### 10.5 Normalization uncertainty estimate and corrections

The various factors in equation (10.12) contain statistical errors due to the finite number of data and Monte Carlo events. The largest fractional error comes from real data statistics, and it is equal to

3.1%. Adding the other uncertainties in quadrature we find a 3.8% statistical error.

We made the assumption in Section 10.3 that at low intensity we could neglect losses due to global detector and reconstruction inefficiencies, and set  $\varepsilon^* = 1$ . We do not have a direct measurement of the full trigger inefficiency at low intensity, but the study of the efficiency of the  $C_u$  and  $D_u$  counters, which are the main source of the inefficiency at high intensity, suggests that a residual  $5 \pm 1\%$  inefficiency was present at low intensity (see Figure 6.5).

We must also correct for the different particles present in the beam. I shall neglect the effect of 5.2% contamination from  $K^-$ , which behave similarly to  $\pi^-$  in the production of massive lepton pairs. That is, we count the  $K$ 's as  $\pi$ 's in the normalization. The 2.9% contamination of  $\bar{p}$  modifies our estimate of the effective beam rate for two reasons. The foil excitation method is more sensitive to nucleons than to pions by about 50%. Also, anti-protons are less capable of producing lepton pairs at large  $x_F$  because the quark densities decrease with the Feynman variable much more steeply than in a meson. I shall assume that no Drell-Yan pairs come from  $\bar{p}$ , which means that the hadron count given by the ion chambers must be reduced by  $1.5 \times 2.9 = 4.4\%$ .

The error in the absorption cross section is another source of systematic uncertainty. The results in Ref. 34 and 35 differ by about 3% for heavy nuclei, which is equal to the errors quoted for the two measurements. I shall use this value as an estimate of the systematic error due to this effect.

It is difficult to evaluate the precision of the ion chamber calibration. I shall assume a value of 10% as the systematic error.

The linear  $A$  dependence of the Drell-Yan cross section has been measured with an accuracy of 2%<sup>18</sup>. This translates into a 10% error

in extracting the nucleon cross section from our data.

The final estimate of the total number of pions collected at low intensity is

$$N_{\pi}^{\text{total}} = 2.55 \times 10^{11} \quad (10.17)$$

with 10% systematic error, leading to the final form of the normalization equation:

$$\frac{d\sigma^{DY}}{dX_{\text{nucleon}}} = \frac{dN^{DY}}{dX_{hi}} \frac{1}{\varepsilon^o(X)_{hi}} \frac{\text{pbarn}}{4241} \pm 4\%_{\text{stat}} \pm 10\%_{\text{syst}} \pm 10\%_{A\text{-dep}}. \quad (10.18)$$

## 10.6 Secondary interactions

Secondary particles produced in beam particle interactions may have occasionally produced a Drell-Yan pair in a subsequent interaction. This kind of background was suppressed by several factors.

Only secondary pions with a large fraction of the beam momentum could affect our sample of high mass, large  $x_F$  dimuons. The cross section for the process  $\pi^- N \rightarrow \pi^- X$  has been measured in hydrogen<sup>36</sup>. The inclusive cross section is roughly flat for  $x_\pi > .5$ , and grows in the quasi-elastic/elastic peak for  $x_\pi$  very close to 1. The probability of producing a secondary pion with more than half of the available momentum is about 20%.

A further suppression comes from the probability that the secondary particle would interact in the target, which was equal to 63%.

A secondary pion with a fraction  $x_\pi$  of the beam energy interacted with a center-of-mass energy value of

$$\sqrt{s_{\text{sec}}} \approx \sqrt{x_\pi} \sqrt{s_o} \quad (10.19)$$

The real longitudinal momentum fraction,  $x_{F\text{sec}}$ , carried by the dimuon is related to the apparent momentum fraction  $x_F$  which the

analysis program would assign to it by the equation:

$$x_F \text{ sec} \approx x_F/x_\pi \quad (10.20)$$

From this expression we see immediately that background in a particular region of  $x_F$  could be produced only by secondary pions with momentum fraction  $x_\pi > x_F$ .

Parametrizing the mass and center-of-mass dependence of the Drell-Yan process as in equation (9.7) and assuming the form

$$\frac{d\sigma}{dx_F} \propto (1 - x_F)^1 \quad (10.21)$$

we found that the kinematical suppression to be a factor of .2-.3 for  $0.2 \leq x_F \leq 0.6$ , decreasing linearly to zero as  $x_F$  reaches 1.

If we simply multiply all the factors obtained so far, we find that the background from secondary interactions should be about 3.7% for  $x_F \approx 0.2$ , and less at larger  $x_F$  values.

We have implicitly assumed above that the production of high- $x$  secondary pions off nuclei scales as  $A^{0.7}$  like the inelastic cross section. However, measurements performed with proton beams have established that the quasi-elastic component grows more slowly with the atomic number<sup>37</sup>. This appears to be confirmed in absorption studies performed with pions<sup>30,38</sup>. Furthermore, the absorption cross section value used in our analysis is believed not to include the quasi elastic component<sup>30</sup>. Unfortunately, these results refer mostly to extreme  $x_\pi \approx 1$  region, and do not clarify the situation for  $.5 < x_\pi < .95$ .

Given these uncertainties, and especially given the smallness of the effect as estimated above, the results presented in the following chapters have not been corrected for background from secondary interactions.

## Chapter 11

### MASS AND LONGITUDINAL MOMENTUM FRACTION DEPENDENCE OF THE CROSS SECTION

#### 11.1 Variables and method

In this chapter we begin discussion of the results of our study of muon pair production in pion-nucleon collisions at the center-of-mass energy of 12.22 GeV.

We define the variable  $x_F$  in the center-of-mass frame as the ratio between the pair longitudinal momentum and the maximum longitudinal momentum allowed by energy and momentum conservation:

$$x_F \equiv \frac{P_L}{P_L^{max}} \quad ,$$

$$P_L^{max} = \frac{\sqrt{s}}{2} \left( 1 - 2 \frac{M^2 + M_R^2}{s} + \frac{(M^2 - M_R^2)^2}{s^2} - \frac{4P_T^2}{s} \right)^{\frac{1}{2}} \quad (11.1)$$

where  $P_T$  is the pair transverse momentum,  $M_R$  is the recoiling mass, and  $s$  is the square of the center-of-mass energy. This definition is the appropriate generalization of equation (2.5). Note that equation (11.1) allows the value  $x_F = 1$  even when  $P_T$  is non-zero. There is some reduction of phase space as  $x_F \rightarrow 1$ , but the effect is much less than for the simpler definition of  $x_F$ . See Section 14.1 for further discussion.

We shall use the values:

$$\sqrt{s} = 12.22 \text{ GeV} \quad , \quad M_R = .94 \text{ GeV}/c^2. \quad (11.2)$$

The acceptance correction was performed after distributing the collected events in cells in the space of  $x_F$  and  $M$ , the invariant mass of the pair. The cell size was  $\Delta M = 0.1 \text{ GeV}/c^2$ ,  $\Delta x_F = 0.1$ . Only the area  $x_F > 0.2$ ,  $M > 4 \text{ GeV}/c^2$  was considered in this analysis. The former cut eliminates a region of low acceptance (Figure 9.2), and the latter eliminates the region of the  $\Psi$  states (Section 9.6).

Events reconstructed with  $x_F > 1$  have not been used in this analysis.

## 11.2 Results

The differential cross section†  $d^2\sigma/dx_F dM$  is shown in Figures 11.1 to 11.4, as a function of one variable, for different intervals of the other. The results are also shown in Table VIII. The quoted errors are  $1\sigma$  bin to bin statistical fluctuations. The overall normalization uncertainty is discussed in Section 10.5. The curves superimposed on the first two figures derive from structure function fits discussed in Chapter 12. Figures 11.2 and 11.4 are obtained by simply summing the different regions of the Figures 11.1 and 11.3. Figure 11.5 shows the result for  $M^3 d\sigma/dM$  derived from Figure 11.4, expressed vs. the scaling variable  $\sqrt{\tau} = M/\sqrt{s}$ .

† We shall quote cross section values per nucleon. Since we have assumed linear dependence of the cross section on the atomic number, the cross section per tungsten nucleus is obtained multiplying by 184. As about 95% of our dimuons were produced in tungsten, the systematic error due to the  $A$  dependence (Section 10.5) can be neglected for cross section values per nucleus.

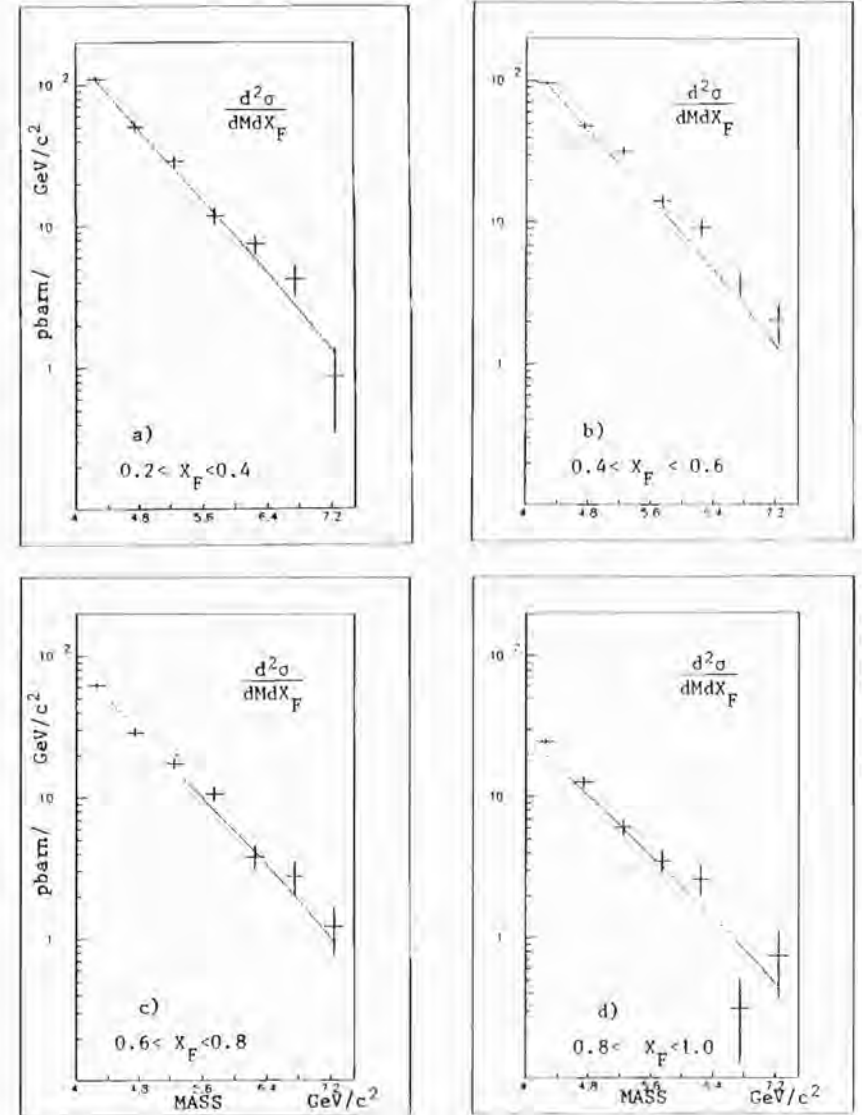


**Fig. 11.1**  $d^2\sigma/dx_F dM$  vs.  $M$  for different  $x_F$  intervals, in  $\text{pbarn}/(\text{GeV}/c^2)$ . The superimposed curves are from the structure functions fit, Chapter 12, Table XI-a and Table XII.

**Fig. 11.2**  $d\sigma/dM$  vs.  $M$ , for  $x_F > 0.2$ , in pbarn/(GeV/c<sup>2</sup>).  
The curve is from the structure functions fit.

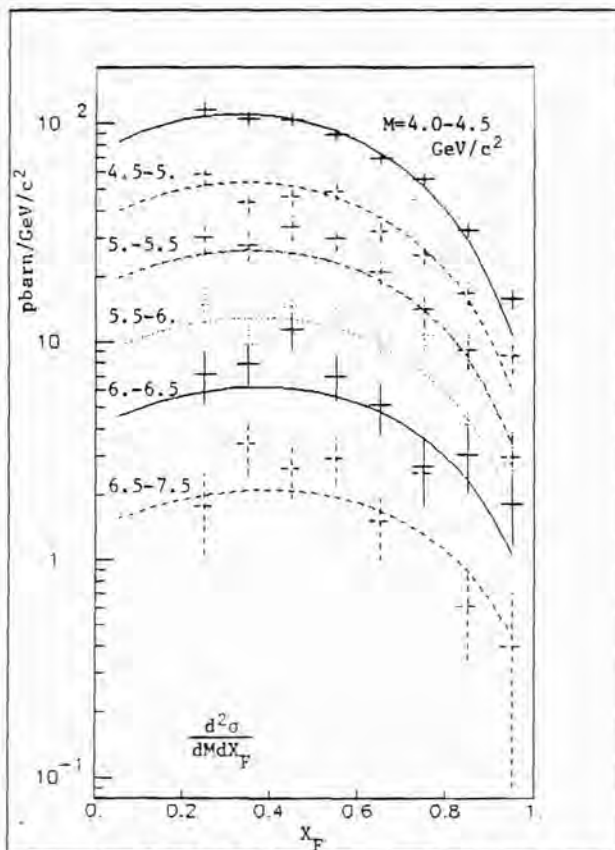
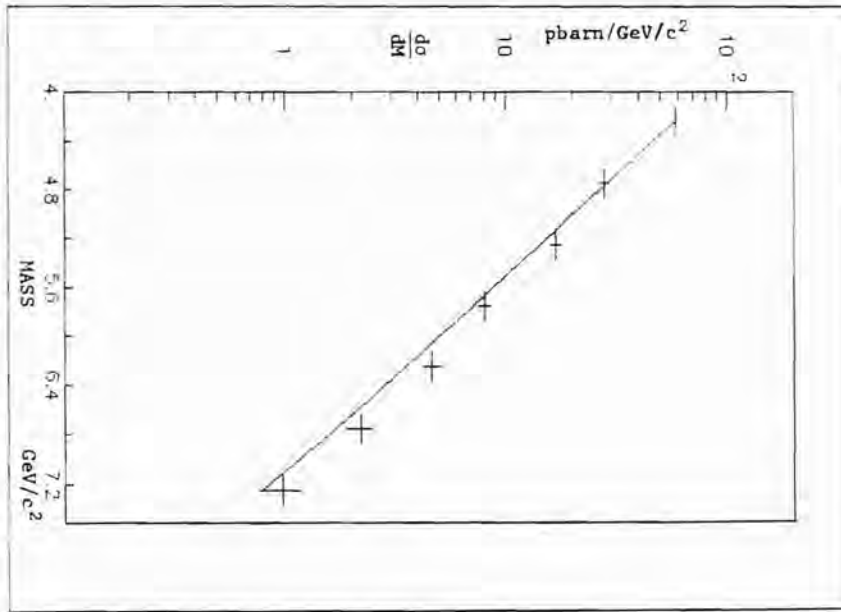


**Fig. 11.3**  $d^2\sigma/dx_F dM$  vs.  $x_F$ , for different  $M$  intervals, in pbarn/(GeV/c<sup>2</sup>). The superimposed curves are from the structure functions fit, Chapter 12, Table XI-a and Table XII.

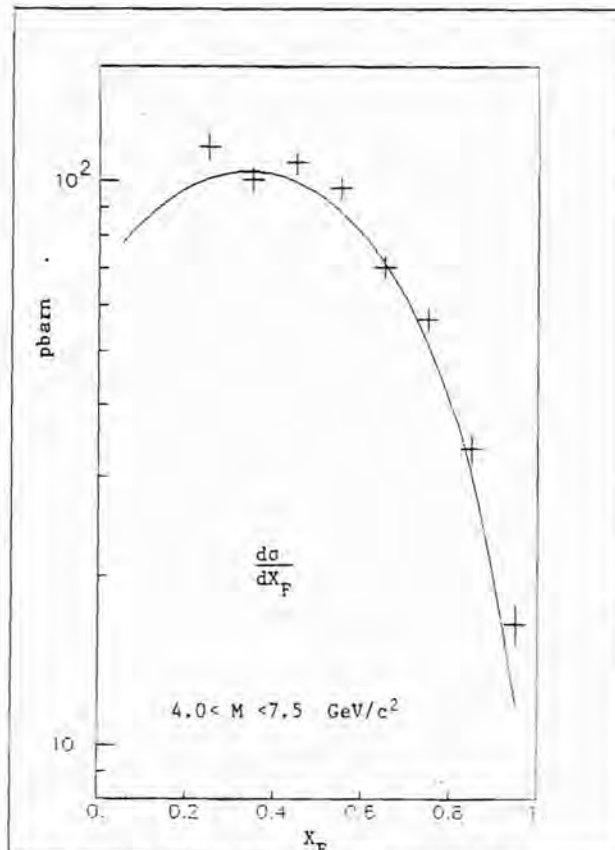


**Fig. 11.4**  $d\sigma/dx_F$  vs.  $x_F$  (for  $M > 4$  GeV/c<sup>2</sup>).  
The curve is from the structure functions fit.

**Table VIII** Cross section  $d^2\sigma/dx_F dM$  in mass and  $x_F$  intervals.

$\Delta M$ (GeV/c <sup>2</sup> )	$\Delta x_F$	$d^2\sigma/dx_F dM$ ( $\frac{\text{pbarn}}{(\text{GeV}/c^2)^2}$ )	
4.0 - 4.5	.2 - .3	115.9	$\pm$ 9.0
	.3 - .4	105.0	7.3
	.4 - .5	104.0	6.8
	.5 - .6	88.6	5.4
	.6 - .7	69.0	4.2
	.7 - .8	55.8	3.6
	.8 - .9	32.7	2.4
	.9 - 1.0	15.7	1.6
	4.5 - 5.0	.2 - .3	58.7
.3 - .4		43.8	5.2
.4 - .5		46.6	4.8
.5 - .6		49.1	4.7
.6 - .7		32.3	3.3
.7 - .8		25.1	2.7
.8 - .9		16.6	2.1
.9 - 1.0		8.7	1.5
5.0 - 5.5		.2 - .3	30.4
	.3 - .4	27.7	4.3
	.4 - .5	33.6	4.3
	.5 - .6	30.1	3.8
	.6 - .7	20.9	2.8
	.7 - .8	14.0	2.1
	.8 - .9	9.1	1.7
	.9 - 1.0	2.98	0.88
	5.5 - 6.0	.2 - .3	14.9
.3 - .4		9.7	2.1
.4 - .5		14.3	2.6
.5 - .6		13.8	2.3
.6 - .7		10.6	1.8
.7 - .8		10.7	1.9
.8 - .9		4.2	1.0
.9 - 1.0		2.75	0.89
6.0 - 6.5		.2 - .3	7.1
	.3 - .4	7.9	1.8
	.4 - .5	11.3	2.3
	.5 - .6	7.0	1.7
	.6 - .7	5.1	1.3
	.7 - .8	2.71	0.84
	.8 - .9	3.1	1.0
	.9 - 1.0	1.83	0.66
	6.5 - 7.5	.2 - .3	1.79
.3 - .4		3.43	0.98
.4 - .5		2.64	0.73
.5 - .6		2.94	0.70
.6 - .7		1.52	0.52
.7 - .8		2.51	0.72
.8 - .9		0.61	0.26
.9 - 1.0		0.40	0.31

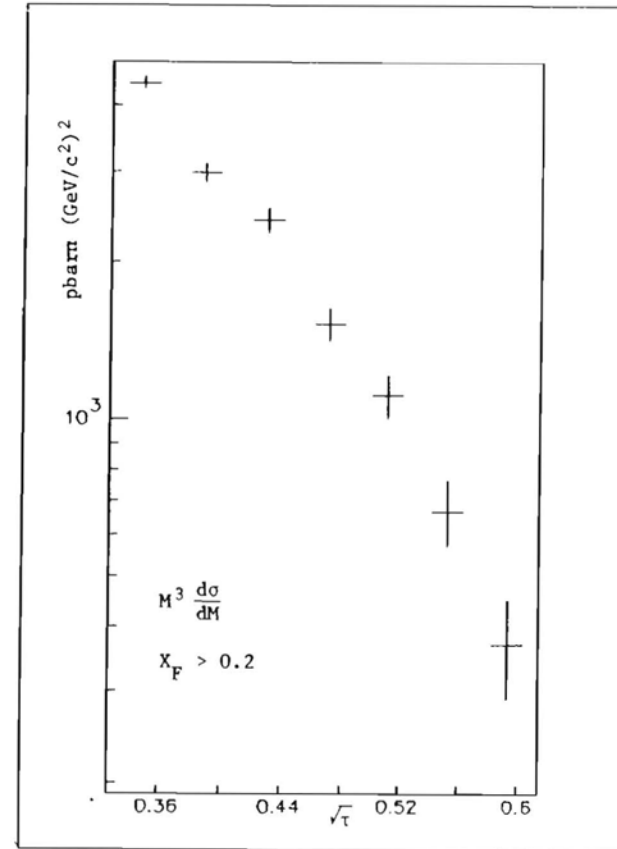


**Fig. 11.5**  $M^3 d\sigma/dM$  vs.  $\sqrt{\tau}$ , for  $x_F > 0.2$ , in  $\text{pbarn} \times (\text{GeV}/c^2)^2$ .

## Chapter 12

### STRUCTURE FUNCTIONS

#### 12.1 Definition of variables and method

In this chapter we shall apply to our data the formalism of the Drell-Yan model, as discussed in Chapters 2 and 3, and extract the pion and nucleon structure functions from the mass and longitudinal momentum distributions.

The Feynman variables  $x_1$  and  $x_2$  will refer to the pion and nucleon constituents, respectively. Our definitions of variables are the following:

$$x_1 \cdot x_2 \equiv \tau = \frac{M^2}{s} \quad , \quad x_1 - x_2 = \frac{2P_L}{\sqrt{s}} \quad (12.1)$$

where  $P_L$  is the pair longitudinal momentum in the center-of-mass frame, and  $\sqrt{s} = 12.22$  GeV. These definitions are the same as those introduced in equations (2.3) and (2.5), and thus the structure function analysis neglects the pair transverse momentum  $P_T$ . This is justified by the smallness of  $P_T^2/s$ , which fixes the scale of eventual corrections to  $x_1$  and  $x_2$  at about 0.01–0.02. Furthermore, the corrections would require a choice of a model for the source of  $P_T$ . We shall discuss the transverse momentum distributions in Chapter 14.

Figure 12.1.a shows the data distribution, uncorrected for acceptance, in the plane  $x_1$ - $x_2$ , limited by the requirements  $M > 4$  GeV/c<sup>2</sup>,

and  $x_F > 0.15$ . Figures 12.1.b and 12.1.c show the projected distributions on the  $x_1$  and  $x_2$  axes respectively. The correction for the acceptance was done according to the procedure described in Chapter 9, and the events were binned into cells of size  $\Delta x_1 = 0.05$ ,  $\Delta x_2 = 0.025$ . Figure 12.2 shows the boundaries of cells actually used in the fit. The choice of cell boundaries places a cut on  $x_F$  approximately at a value of 0.2.

Our events are distributed with  $x_1 > 0.4$ . According to theoretical expectations and to an experimental observation performed at larger values of  $\sqrt{s}$ ,<sup>10</sup> sea quarks populate only the region of  $x_1$  lower than this. We shall therefore assume that the quark densities  $f_\pi^q(x_1)$  and  $f_\pi^{\bar{q}}(x_1)$  of equation (2.7) contain only the **valence** component. As we used a  $\pi^-$  beam, the quark model allows us to identify these densities with **down** quarks and **up** anti-quarks respectively. Isospin invariance and charge conjugation invariance require that the two distributions be equal. Therefore, we may introduce a single **pion structure function**  $F_\pi$  defined as follows:

$$F_\pi \equiv x_1 \cdot \bar{u}_\pi^v(x_1) = x_1 \cdot d_\pi^v(x_1) \quad , \quad (12.2)$$

where the superscript  $v$  indicates valence quark distributions.

Within the  $x_2$  acceptance of our experiment, the nucleon participates in the Drell-Yan process through both its valence and sea quarks. For simplicity, let us first identify the quark distributions which enter Drell-Yan scattering if the nucleon is a proton:

$$\pi^- - p \quad : \quad \frac{d\sigma}{dx_2} \propto \frac{4}{9} (u(x_2) + u^s(x_2)) + \frac{1}{9} \bar{d}^s(x_2) \quad (12.3)$$

where  $u(x_2)$  is the valence up-quark distribution in the proton, and the superscript  $s$  indicates sea quark distributions. The contributions

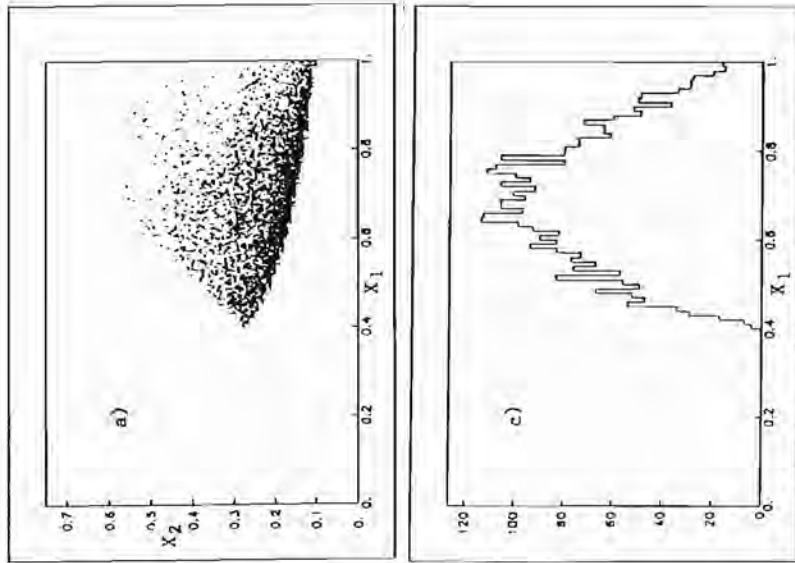


Fig. 12.1 a,b,c Scatterplot of the data sample in the  $x_1$ - $x_2$  plane with projections. The boundaries are  $x_1 \times x_2 > .107$  ( $M > 4 \text{ GeV}/c^2$ ), and  $x_F > 0.15$ .

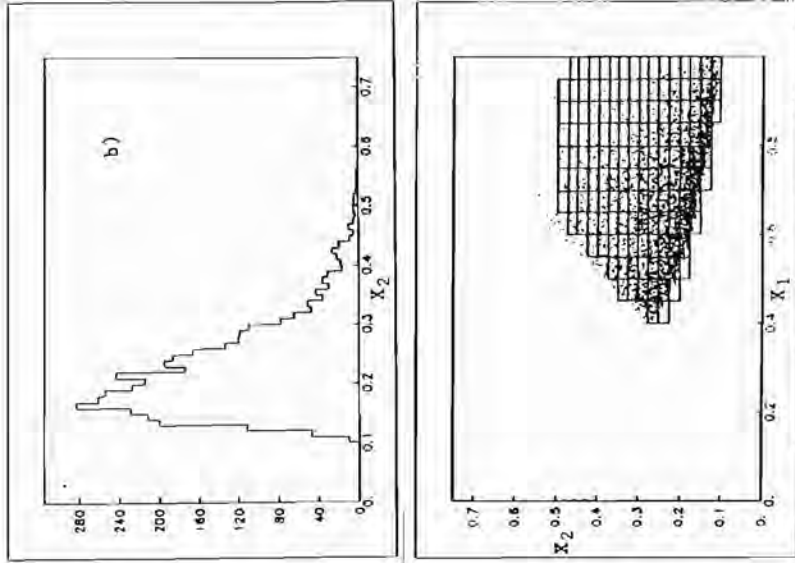


Fig. 12.2 Pattern of the  $x_1$ - $x_2$  cells used in the structure functions fit.

from different quarks are of course weighted with the squares of their electric charges. From isospin invariance we expect that

$$u^s = \bar{u}^s = d^s = \bar{d}^s \equiv S,$$

and so expression (12.3) can be written:

$$\frac{4}{9}u(x_2) + \frac{5}{9}S(x_2) \quad (12.4)$$

A pion-neutron interaction is described replacing  $u$  with  $d$  and  $d$  with  $u$ , because of isospin invariance. In case of heavy nuclei, with the ratio of the atomic numbers  $Z/A$  equal to 0.4, we may then introduce an **effective nucleon structure function**  $F_N$  by the expression:

$$\frac{4}{9}(0.4u(x_2) + 0.6d(x_2)) + \frac{5}{9}S(x_2) \equiv \frac{1}{x_2}F_N(x_2) \quad (12.5)$$

Guided by equation (2.7), we have studied the factorization hypothesis and the structure functions by comparing our data with the expression:

$$\frac{d^2\sigma}{dx_1dx_2} = \frac{4\pi\alpha^2}{9s} \frac{F_\pi(x_1)F_N(x_2)}{x_1^2x_2^2} K_f \quad (12.6)$$

The K-factor,  $K_f$ , introduced in Section 3.4, will be taken as constant. We shall discuss the normalization of the structure functions in Section 12.7.

## 12.2 Results - Factorization

As shown in Figure 12.2, we divided our data in 143 cells in the  $x_1$ - $x_2$  plane. The contents of each cell were corrected for acceptance and then normalized as discussed in Chapters 9 and 10, to produce values of the cross sections  $d^2\sigma/dx_1dx_2$ . We then examined the grid

of cross sections for compatibility with factorization into the product of two structure functions as given in equation (12.6). An analytic average of the weight function  $(x_1 x_2)^{-2}$  was calculated for each cell. Special care was taken for the cells cut by the lower mass boundary  $x_1 x_2 = .1072$ , corresponding to  $M = 4 \text{ GeV}/c^2$ . We fitted twelve values for the pion structure function for  $0.4 < x_1 < 1$ , in intervals of 0.05, and sixteen values for the nucleon structure function, for  $0.1 < x_2 < 0.5$ , in intervals of 0.025. The fit has a  $\chi^2$  value of 123 with 116 degrees of freedom, in good agreement with the factorization hypothesis. Figures 12.3 and 12.4 give the shape of the two structure functions, also given in Table IX and X.† The superimposed curves are described below.

### 12.3 Shape of the pion structure function

We have parametrized the pion structure function according to the expression:

$$F_\pi \propto x_1^\alpha \{(1 - x_1)^\beta + \gamma\} \quad (12.7)$$

Table XI contains the results of the fit (Fit a), which approximates very well the results of the previous section, as shown in Figure 12.3.

Notice that our restriction to  $x_1 > 0.4$  does not allow good accuracy in the parameter  $\alpha$ . Table XI also shows the results of the fit obtained by imposing the value of  $\alpha$  to be value 0.4 (Fit b). This value was chosen to check the consistency of our results with a previous observation of the pion structure function, performed at larger center-of-mass energy<sup>10</sup>. The quality of the new fit is almost as good

† The quoted errors were obtained for each hadron by fixing the parameters of the other hadron to the best fit values. This technique aided the convergence of the fitting program without affecting the error estimates by more than a few percent.

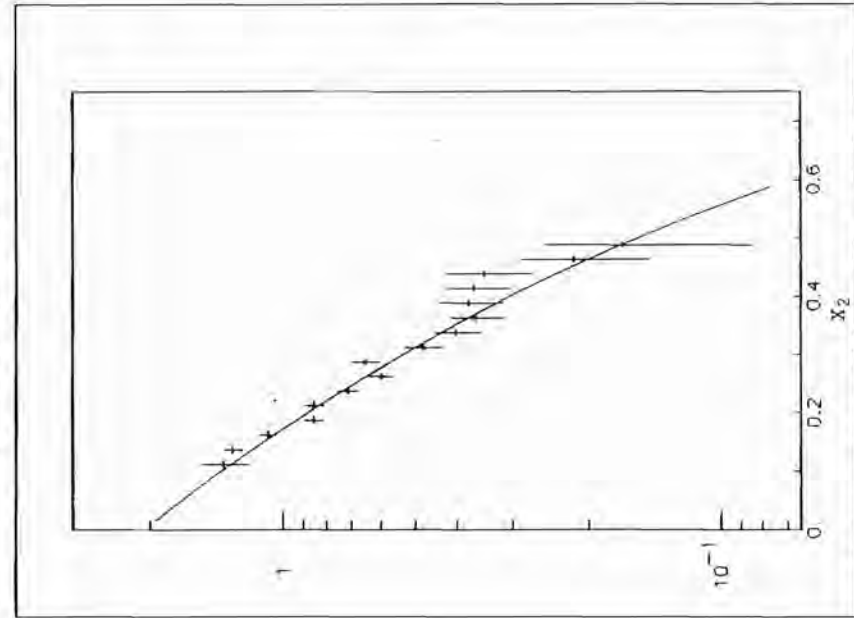


Fig. 12.4 Fit for  $F_N(x_2)$ . The points are from Table X, the curve from Table XIII.

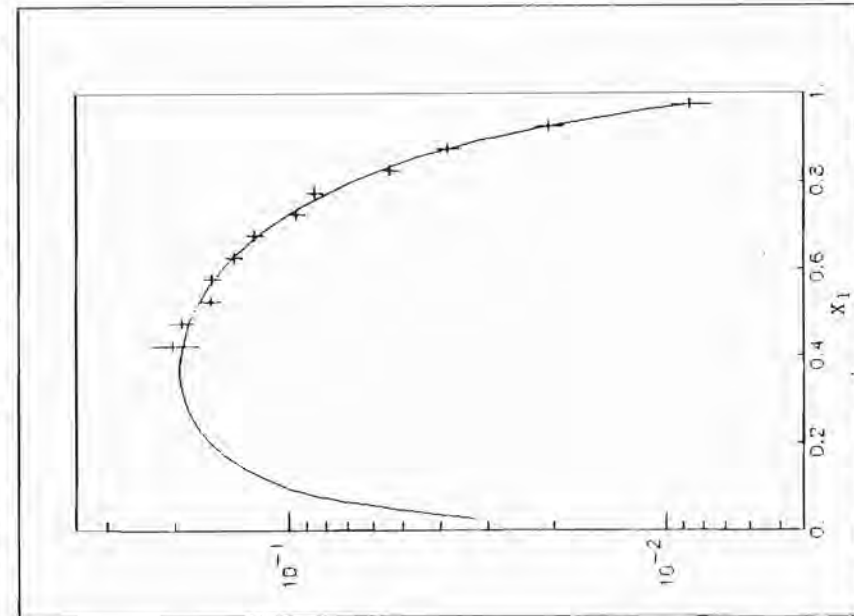


Fig. 12.3 Fit for  $F_\pi(x_1)$ . The points are from Table IX, the curve from Table XI-a.

**Table X** Nucleon structure function  $F_N(x_2)$ , in arbitrary units.

$\Delta x_2$	$F_N$	$\sigma(\text{stat})$
.100-.125	1.36	0.17
.125-.150	1.297	0.067
.150-.175	1.083	0.048
.175-.200	0.851	0.041
.200-.225	0.850	0.041
.225-.250	0.714	0.038
.250-.275	0.600	0.034
.275-.300	0.651	0.048
.300-.325	0.479	0.046
.325-.350	0.403	0.049
.350-.375	0.364	0.051
.375-.400	0.378	0.063
.400-.425	0.367	0.063
.425-.450	0.348	0.077
.450-.475	0.215	0.070
.475-.500	0.176	0.083

**Table IX** Pion structure function  $F_\pi(x_1)$ , in arbitrary units.

$\Delta x_1$	$F_\pi$	$\sigma(\text{stat})$
.40 - .45	0.199	0.029
.45 - .50	0.188	0.014
.50 - .55	0.156	0.010
.55 - .60	0.1548	0.0086
.60 - .65	0.1343	0.0069
.65 - .70	0.1177	0.0059
.70 - .75	0.0910	0.0048
.75 - .80	0.0820	0.0041
.80 - .85	0.0517	0.0031
.85 - .90	0.0367	0.0025
.90 - .95	0.0198	0.0016
.95 - 1.0	0.00832	0.00099

**Table XI** Functional fits to the pion structure function.

$F_\pi \propto x^\alpha \{ (1-x)^\beta + \gamma \}$				
	$\alpha$	$\beta$	$\gamma$	$\chi^2/\text{DOF}$
a)	$.92 \pm .38$	$1.59 \pm .13$	$.0060 \pm .0016$	130/125
b)	.4 fixed	$1.37 \pm .07$	$.0072 \pm .0021$	132/126

as that of the first one. Notice the strong correlation between  $\alpha$  and  $\beta$ .

The third parameter,  $\gamma$ , is not particularly affected by the change between the two fits. Our statistical resolution in determining its difference from zero is between 3 and 4 standard deviations.

A non-vanishing intercept of the pion structure function at  $x_1=1$  was suggested in reference 27, which predicted an effect of the size of 0.01—in our units—, and also predicted  $\alpha$  to be equal to 1 and  $\beta$  to be equal to 2 for  $x_1 > 0.5$ . This appears to be consistent with our results, which suggest a value of the parameter  $\langle K_T^2 \rangle$  in equation (3.3) in the range .6-.7. Previous experiments did not have the sensitivity to measure a finite intercept as small as 0.01. Table XII shows the residuals between the values of the cross section  $d^2\sigma/dx_1 dx_2$  and the fit obtained with the pion parametrization (Fit a) in Table XI, and the values of the nucleon structure function from Table X. The differences are given in units of  $1\sigma$  statistical error.



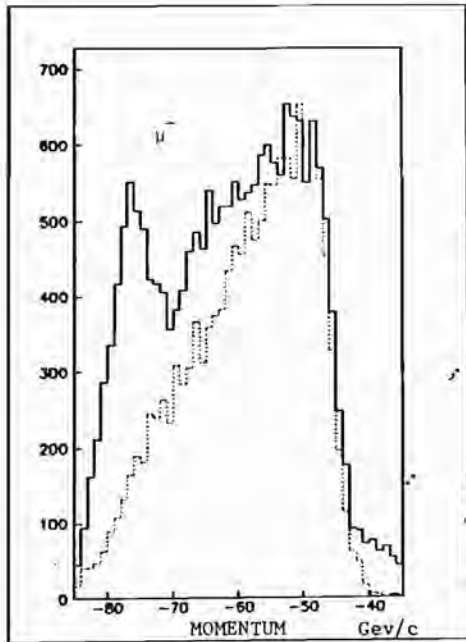


**Fig. 12.5** Distribution of negative muons detected with a Level-1 trigger (Chapter 5), without beam-muon cuts. The dotted line is from a Monte Carlo simulation using a central beam momentum of 79.0 GeV/c.

found for the width of the beam momentum distribution: the spectrum of the beam-halo muons appeared fully compatible with values of the full width at half maximum in the range 7-10%.

To study the effect of uncertainty in the beam momentum on the pion structure function, we shifted the central beam momentum used in the analysis. A momentum change of 0.4% produces the following changes in the fitted parameters:

$$\begin{aligned} \text{Fit a} & : \Delta\alpha = +.07 \quad \Delta\beta = +.05 \quad \Delta\gamma = -.0011 \\ \text{Fit b} & : \quad \quad \Delta\beta = +.02 \quad \Delta\gamma = -.0015 \end{aligned}$$

Our fits for the pion structure function did not make any use reconstruction program takes into account the average energy loss in the target, and uses an effective momentum value of 79.0 GeV/c.

of 18 events reconstructed with  $x_1 > 1$ . The number of overflows is well reproduced by the Monte Carlo simulation. The main source of these events is the beam momentum spread, and the good agreement between data and simulation adds confidence in our understanding of this aspect of our experiment. Recall that the acceptance calculation accounts for the number of overflows by a corresponding reduction in the acceptance for the bins with  $x_1$  slightly less than 1.

#### 12.4.2 Fermi motion correction

As mentioned in Section 9.4, the acceptance calculation accounts for Fermi motion in the target nuclei. We investigated the effects of ignoring this correction, obtaining the following results for the pion structure function fit:

$$\begin{aligned} \text{Fit a} & : \Delta\alpha = +.05 \quad \Delta\beta = +.03 \quad \Delta\gamma = -.0007 \\ \text{Fit b} & : \quad \quad \Delta\beta = +.02 \quad \Delta\gamma = -.0007 \end{aligned}$$

#### 12.5 Fit to the nucleon structure function

Different parametrizations were used to describe the nucleon structure function. Table XIII shows the results obtained using the form:

$$F_N(x_2) \propto (1 - x_2)^6 (1 - \epsilon x_2) \quad (12.8)$$

The resulting curve is shown on Figure 12.4.

Other parametrizations were used following the prescriptions of fits based on measurements of individual quark distributions in deep inelastic weak and electromagnetic scattering.<sup>39</sup> These fits include logarithmic variation of the parameters with the  $Q^2$  of the probe, as suggested by QCD. We evaluated the fit parameters at our scale value,  $\langle M^2 \rangle = 23 \text{ GeV}^2/c^4$ , and calculated the effective nucleon structure function according to equation (12.5). In comparing this function to

**Table XIII** Functional fit to the nucleon structure function.

$F_N(x) = K (1-x)^\delta (1+\epsilon x)$								
		correlation matrix						
K	$2.06 \pm .12$	<table border="1"> <tr> <td>K</td> <td><math>\delta</math></td> </tr> <tr> <td><math>\delta</math></td> <td><math>-.02</math></td> </tr> <tr> <td><math>\epsilon</math></td> <td><math>-.33 \quad .95</math></td> </tr> </table>	K	$\delta$	$\delta$	$-.02$	$\epsilon$	$-.33 \quad .95$
K	$\delta$							
$\delta$	$-.02$							
$\epsilon$	$-.33 \quad .95$							
$\delta$	$3.25 \pm .65$							
$\epsilon$	$-.58 \pm .67$							
$\chi^2/\text{DOF} = 19.2/13$								

our measurements only the overall normalization was free to vary. The results corresponding to two different parametrizations, described in Table XIV, are shown in Figures 12.6. § Notice that our measurements are not in agreement with these parametrizations, which however are not very compatible with each other. We find a steeper behaviour of  $F_N(x_2)$  for  $x_2 < 0.2$ , which is the region in which sea quarks become dominant. However, implausibly large sea quark distributions would be required to reproduce our measurements.

### 12.6 Systematic effects in determining $F_N$

Our parametrization (12.8) of the nucleon structure function is very stable with respect to variations in the analysis procedure. No significant variations were found when taking  $F_\pi$  to be a set of fixed values as in Table IX, or to have either of the functional forms given

§ The first parametrization was found to reproduce dimuon data. See reference 10.

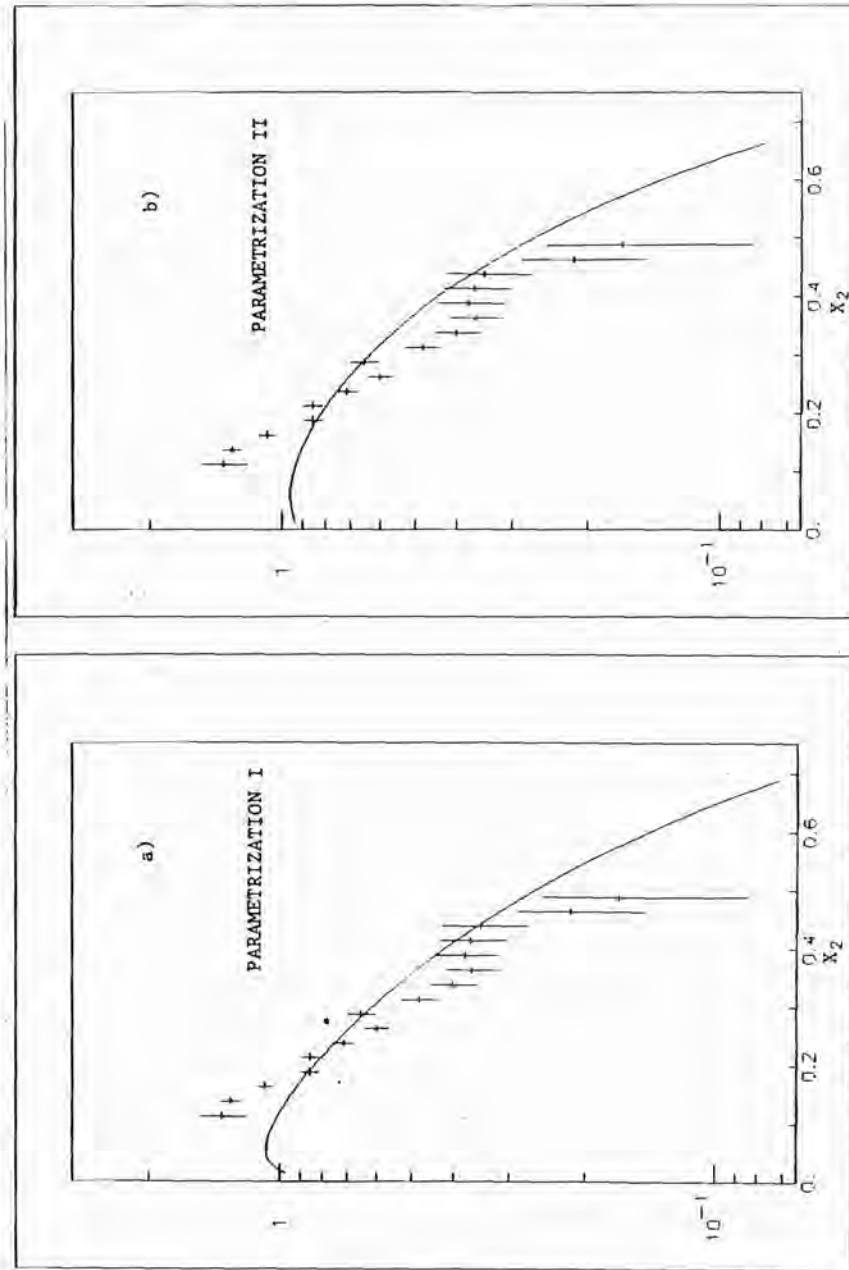


**Fig. 12.6** Our results for the nuclear structure function (data points), compared with the parametrizations of the quark densities in Table XIV, Ref. 39.

**Table XIV** Parametrization of the nucleon quark densities according to Ref. 39.

$F_N = K \{4/9(0.4x u(x)+0.6x d(x)) + 5/9x S(x)\}$
<p>PARAMETRIZATION I OF THE NUCLEON QUARK DENSITIES</p>
$x \cdot u(x) = 2.206 x^{0.51}(1-x)^{2.82}$ $x \cdot d(x) = 1.250 x^{0.51}(1-x)^{3.82}$ $x \cdot S(x) = 0.268 (1-x)^{8.2}$
<p>PARAMETRIZATION II OF THE NUCLEON QUARK DENSITIES</p>
$x \cdot (u(x) + d(x)) = 2.15 x^{0.42}(1-x)^{3.77}(1+3x)$ $x \cdot d(x) = 2.40 x^{0.69}(1-x)^{4.20}(1-.13x)$ $x \cdot S(x) = 0.156 x^{-0.126}(1-x)^{8.54}(1+1.96x-3.62x^2+5.60x^3)$

in Table XI. The results in Table X are the ones obtained using (Fit b) of Table XI for the pion structure function. Only minor changes arose after removing the Fermi motion correction from the acceptance calculation.

On the other hand, imposing a particular shape on the nucleon structure function can affect the fit to the pion structure function. Very small changes are induced on the pion structure function by using the parametrization (12.8) for the nucleon, compared to the use of a set of values as in Table X. But larger effects arise if we impose either of the nucleon structure functions extrapolated from deep inelastic scattering. For example, if we use the first parametrization in Table XIV the effects on the pion structure function parameters are the following:

$$\text{Fit a} : \Delta\alpha = +.66 \quad \Delta\beta = +.13 \quad \Delta\gamma = -.0011$$

$$\text{Fit b} : \Delta\beta = -.19 \quad \Delta\gamma = -.0022$$

These variations give an idea of the sensitivity of the pion parametrization to the nucleon structure function shape, but are certainly an overestimate of the systematic uncertainty, since the nucleon function of Table XIV does not approximate our data.

### 12.7 Normalization of the structure functions and the K-factor

If we can independently normalize the structure functions  $F_\pi$  and  $F_N$  then we can extract the K-factor which appears in equation (12.6). In Section 3.4 we discussed how a value of  $K_f \neq 1$  might be a sign of higher order QCD corrections to the Drell-Yan process.

Normalization conditions for the structure functions are, however, indirect. The structure functions are momentum distributions, so that their integrals are related to the total momentum carried by

quarks. While this must be less than or equal to 1, a value of 1/2 is considered most plausible, which is not a precise restriction. The valence quark densities must obey the conditions that their integrals yield the total number of quarks in the hadron. The densities are related to the structure functions by a factor of  $1/x$ , so we obtain a constraint mainly on the low- $x$  behavior of the structure functions.

Two effects make the determination of the K-factor from our data difficult. The first is due to the fact that our data, collected at large  $x_1$ , do not allow a good normalization of the pion structure function. The quark density is proportional to  $F_\pi/x_1$ , and the extrapolation of the quark density to the region of  $x_1 \approx 0$  is critical to the normalization.

The second difficulty is related to our measurement of the nucleon structure function. This cannot be well fit by any of the popular, and normalizable, parametrizations used in deep inelastic scattering experiments. Notice that comparison with deep inelastic data would be rather ambiguous in any case, since different quark combinations are measured in the two processes. This is best shown by the difference in the Drell-Yan nucleon structure function obtained using the two quark density distributions in Table XIV, both of which apparently give a consistent picture of the deep inelastic scattering structure functions. On the other hand our experiment by itself does not provide sufficient information to normalize all four quark density functions appearing in equations (12.2) and (12.5).

In order to estimate the range of K-factor values which is consistent with our data, we fit the cross section according to equation (12.6) for several hypotheses about the structure functions. For the pion structure function we used the form (12.7) and normalized this to one antiquark per pion after the parameters  $\alpha$ ,  $\beta$  and  $\gamma$  were known. For the nucleon structure function we used the normalized parametriza-

**Table XV** Values of the K-factor obtained approximating  $F_\pi$  according to Table XI, and using parametrization I of Table XIV for  $F_N$ .

$\alpha$	$\beta$	$\gamma$	K-factor	$\chi^2/\text{DOF}$
.92 fixed	1.59 fixed	.0060 fixed	2.0	210/143
.4 fixed	1.37 fixed	.0072 fixed	4.5	222/143
1.58	1.78	.0049	1.1	192/140
.4 fixed	1.18	.0050	3.7	204/141

tion I of Table XIV. The results are given in Table XV. The first two lines show the K-factor obtained when the pion structure function parameters were fixed to the values in Table XI, which were found without imposing a shape for the nucleon structure function. The third line shows the result obtained when the parameters  $\alpha$ ,  $\beta$  and  $\gamma$  as well as the K-factor were free to vary. In the fourth line only  $\beta$  and  $\gamma$  were varied.

The conclusion is that the indetermination in the parameter  $\alpha$  is large enough to produce fluctuations of the order of 2 in the normalization of the pion structure function, and therefore in the resulting K-factor. The use of the second nucleon parametrization from Table XIV yields values of K generally smaller by 0.1. Since an experiment measuring  $F_\pi$  at smaller  $x_1$  determined  $\alpha$  to be about 0.4,<sup>10</sup> it appears that our measurement favors values of the K-factor larger than measured before. Notice however that the difficulty in normalizing the nucleon structure function adds further uncertainty to this result.

## 12.8 Summary of results on the structure functions

Our sample allows an accurate study of the pion structure function at large values of the Feynman variable  $x_1$ . Our results suggest a finite intercept at  $x_1=1$ , measured with 3 standard deviation significance. Our data also favor values of the parameters  $\alpha$  and  $\beta$  in equation (12.7) larger than those measured before.

These effects appear to be in agreement with a prediction based on higher twist QCD computations. This subject is related to an effect in the lepton pair angular distribution, which will be discussed in the Chapter 13.

The shape of the nucleon structure function does not agree well with parametrizations deduced from deep inelastic scattering observations. A precise comparison appears to be model dependent. Nevertheless, a previous muon pair experiment observing different kinematic regions found agreement with one such parametrization<sup>10</sup>. Our data might be evidence of difficulty encountered by the Drell-Yan picture at small total energies, or at large values of  $\sqrt{\tau}$ .

## Chapter 13

### ANGULAR DISTRIBUTION

#### 13.1 Reference axes

In this chapter, we shall discuss the orientation of the muon pair in the the frame where its total momentum vanishes (the rest frame of the pair). If the pair is produced in the scattering of scalar or unpolarized hadrons, the only vectors available to define an angular distributions are the momentum of the beam particle, which we call  $\vec{\pi}$ , and the the momentum of the target nucleon  $\vec{N}$ . Notice that these two vectors would be parallel in the pair rest frame if the pair had vanishing transverse momentum in the overall center-of-mass frame.

The reference axis  $\hat{z}$  is usually chosen to approximate the direction of the annihilating quarks. Figure 13.1 shows the definition of the **t-channel** frame, also known as Gottfried-Jackson frame, in which the polar axis  $\hat{z}$  is parallel to  $\vec{\pi}$ . We shall measure the angles of the positive muon direction, using  $-\vec{N}$  to define the  $\hat{x}$  direction.

We shall also quote results in the Collins-Soper (**CS-channel**) frame, where the polar axis is defined as the bisector of the directions of  $\vec{\pi}$  and  $-\vec{N}$ . If the annihilating quarks move along the  $z$  axis in this frame, each would carry 1/2 of the transverse momentum of the resulting muon pair. Both the t- and CS-channel frames are rest frames of the muon pair. The difference between the directions of the

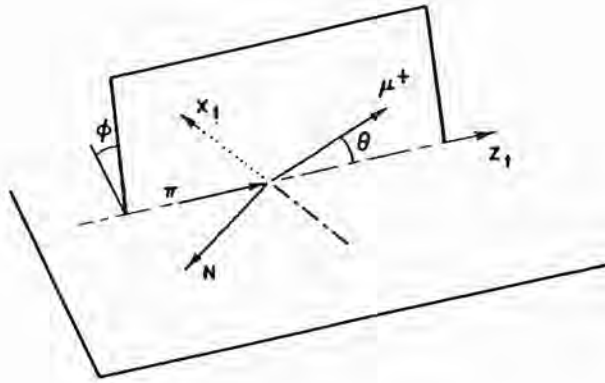


Fig. 13.1 Definition of  $t$ -channel (Gottfried-Jackson) axes.

reference axes of the two frames is of the order of

$$((P_T^2)/\langle M^2 \rangle)^{1/2} \approx 0.2 \text{ rad}$$

in our dimuon sample, using the observed average values for the invariant mass and the transverse momentum of the pairs.

### 13.2 Analysis procedure

In general, the angular distribution of a pair of fermions produced in the materialization of a massive photon should be described by the expression given in equation (2.11), which we shall use in the following form:

$$\frac{d^2\sigma}{d\Omega} = K(1 + \lambda \cos^2\theta + \rho \sin 2\theta \cos \phi + \omega \sin^2\theta \cos 2\phi) \quad (13.1)$$

However, we shall be concerned with the dependence of the angular distribution coefficients on the other variables such as  $M$ ,  $P_T$  and the Feynman variable  $x_F$ . The statistical power of our sample of 4060 high mass events is reduced by the subdivision into different kinematic

regions, and we shall mostly present results on a parametrization given by

$$\frac{d\sigma}{d\cos\theta} = K(1 + \lambda \cos^2\theta) \quad (13.2)$$

We have corrected for the acceptance both before, or after, integration over the azimuthal angle  $\phi$ . As shown below, the two methods provide the same results for the fitted parameter  $\lambda$ .

In general, the cross section calculation has been performed after dividing the data into several intervals of  $x_F$  or  $x_1$ , where the latter Feynman variable refers to the anti-quark from the pion, as well as intervals of any other variable of interest. If we wished to study the cross section dependence on, say,  $\theta$  and  $P_T$ , we first calculated the cross sections versus  $\theta$ ,  $P_T$  and  $x_F$ , and then integrated over  $x_F$ . This minimized difficulties of convergence of the acceptance-cross section calculation described in Chapter 9.

### 13.3 Results

Table XVI shows the results of a fit of the form in equation (13.2), in the  $t$ -channel and in the CS-channel for events satisfying the requirements of  $M > 4 \text{ GeV}/c^2$ ,  $x_F > 0.15$ . Only statistical errors are quoted. Figure 13.2 shows the relative differential cross sections in bins of  $\cos\theta$ , superimposed with the fit.

Notice that values of  $\lambda$  are somewhat smaller than those predicted by the Drell-Yan model ( $\lambda \simeq 0.8-1.0$ ), and also smaller than those reported by most previous experiments.<sup>12-16</sup>

Table XVI also contains results obtained by dividing the events into bins of different mass or transverse momentum. No significant variations of the angular parameter were found.

Result of fits to the angular distribution in two variables for the full sample of events are shown in Table XVII. Notice that the coefficients  $\rho$  and  $\omega$  are rather small, and consistent with zero. The

**Table XVI** Value of the parameter  $\lambda$  in  $d\sigma/d\cos\theta \propto 1 + \lambda \cos^2\theta$ , for different classes of events.

	T-CHANNEL			CS-CHANNEL		
	$\lambda$	$\sigma_\lambda$	$\chi^2/\text{DOF}$	$\lambda$	$\sigma_\lambda$	$\chi^2/\text{DOF}$
all events	$.64 \pm .13$		6.1/8	$.66 \pm .17$		4.6/7
$M < 4.8$ Gev/c <sup>2</sup>	$.60 \pm .15$		11.5/8	$.60 \pm .20$		5.4/7
$M > 4.8$	$.60 \pm .26$		3.4/8	$.72 \pm .31$		3.2/7
$p_1 < .8$ Gev/c	$.61 \pm .21$		6.2/7	$.57 \pm .18$		3.5/7
$p_1 > .8$	$.60 \pm .17$		1.5/8	$.73 \pm .24$		4.6/7

measurement of  $\rho$  is made difficult by the correlation with  $\lambda$ , due to the angular acceptance of our detector (Figure 9.7).

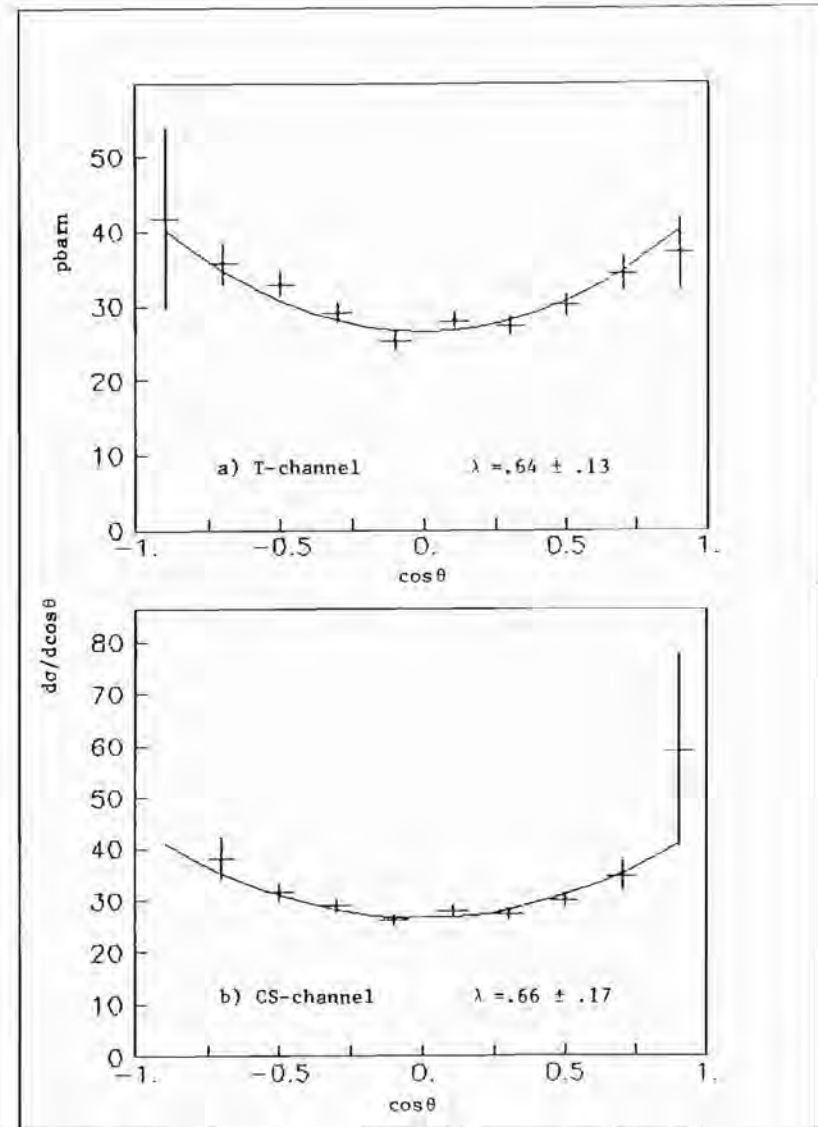
The dependence of the parameter  $\lambda$  on the Feynman variable  $x_1$  was studied in detail, since significant variations were found in the region of  $x_1 > 0.8$ . We divided our sample into bins of  $\Delta x_1$  equal to 0.1 or 0.05, and studied the results of fits to the form in equation (13.2). Figures 13.3 and 13.4 show the double differential cross section as a function of  $\cos\theta$  for different intervals in  $x_1$ .

Figure 13.5 and Table XVIII show the behaviour of the angular distribution parameter  $\lambda$  as a function of  $x_1$ , in the t- and in the CS-channel.

Figures 13.6 and 13.7 show the double differential cross section and the behaviour of  $\lambda$  in thinner  $\Delta x_1$  bins, near  $x_1 = 1$ .

Table XIX contains the corresponding values of  $\lambda$ .

Table XVII contains the results for a fit including  $\phi$ , which gives



**Fig. 13.2**  $d\sigma/d\cos\theta$  vs.  $\cos\theta$  for  $x_F > 0.15$  ( $M > 4$  Gev/c<sup>2</sup>);  
**a)** t-channel;  
**b)** CS-channel.

**Table XVII** Value of the angular distribution parameters for different classes, in the  $t$ -channel.

$d^2\sigma/d\Omega = K ( 1. + \lambda \cos^2\theta + \rho \sin 2\theta \cos \phi + \omega \sin^2\theta \cos 2\phi )$									
$\Delta x_1$	K	$\sigma_K$	$\lambda$	$\sigma_\lambda$	$\rho$	$\sigma_\rho$	$\omega$	$\sigma_\omega$	$\chi^2/\text{DOF}$
.4-1.0	12.51 ± .32		.64 ± .15		-.140 ± .062		.094 ± .034		96.9/73
.4-.5	5.78 ± .73		.62 ± .57		-.06 ± .33		.31 ± .16		16.7/13
.5-.6	8.29 ± .54		1.32 ± .39		-.37 ± .18		.12 ± .12		15.5/16
.6-.7	8.24 ± .43		.71 ± .26		-.16 ± .13		.134 ± .094		12.1/18
.7-.8	6.27 ± .33		.63 ± .26		-.22 ± .12		.116 ± .090		9.4/18
.8-.9	3.34 ± .22		.59 ± .35		.05 ± .15		.04 ± .11		11.5/17
.9-1.0	1.57 ± .14		-.46 ± .42		.13 ± .16		-.12 ± .13		7.0/13
M < 4.8 GeV/c	7.86 ± .24		.68 ± .18		-.191 ± .080		.082 ± .043		106./72
M > 4.8 GeV/c	4.21 ± .21		.79 ± .33		-.04 ± .10		.117 ± .062		56.3/66
p < 0.8 GeV/c	5.83 ± .20		.84 ± .24		-.180 ± .078		.057 ± .043		82.4/67
p > 0.8 GeV/c	6.44 ± .27		.70 ± .21		-.27 ± .12		.212 ± .061		84.3/67

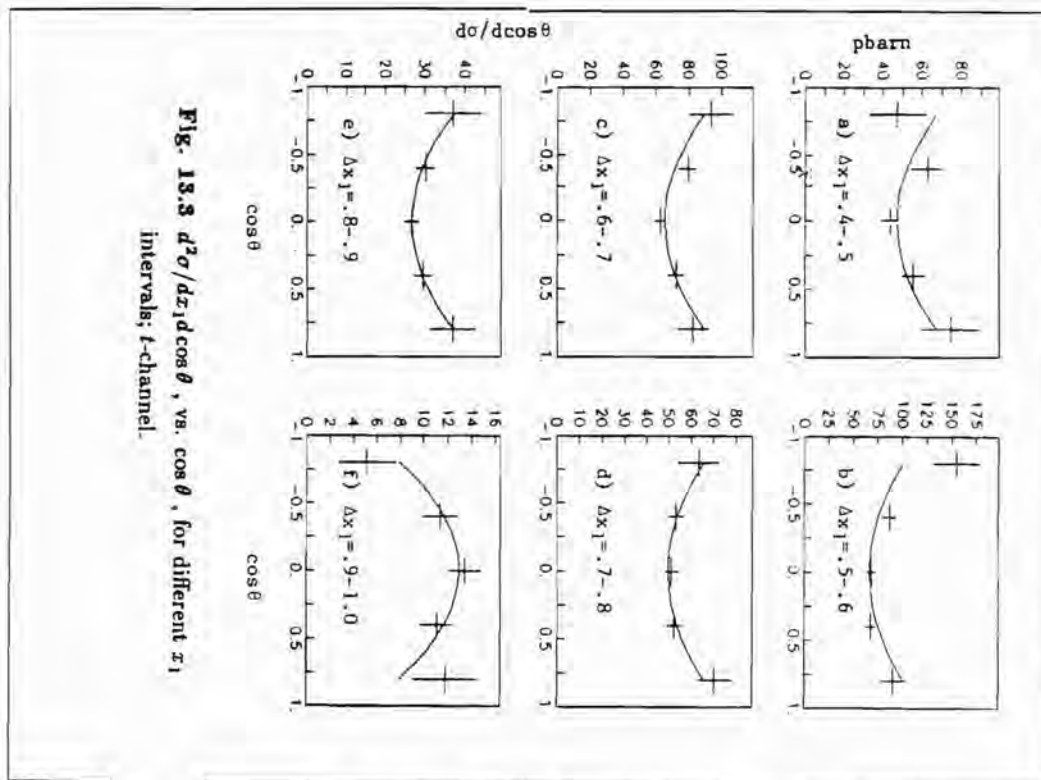
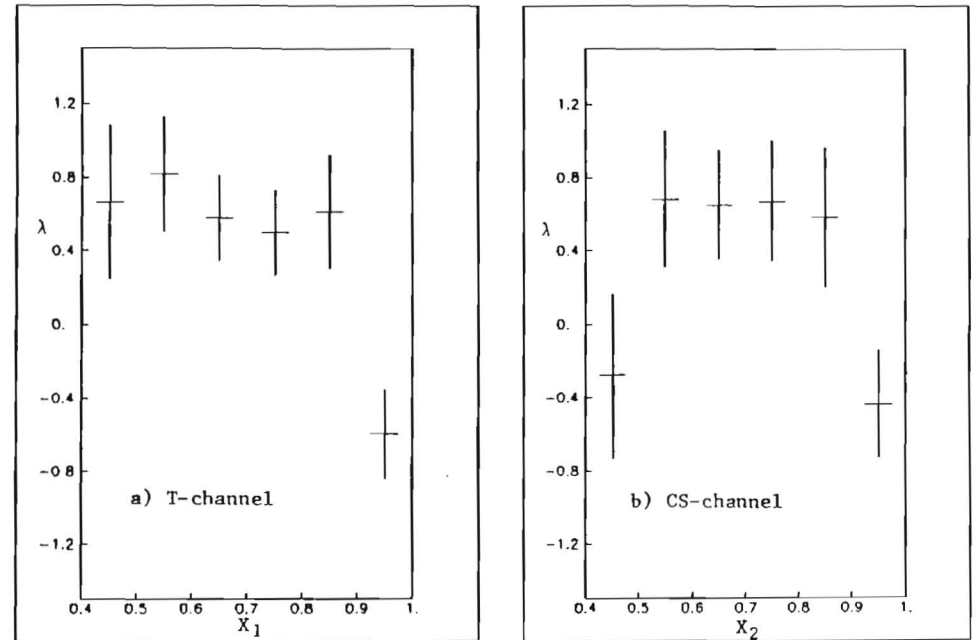
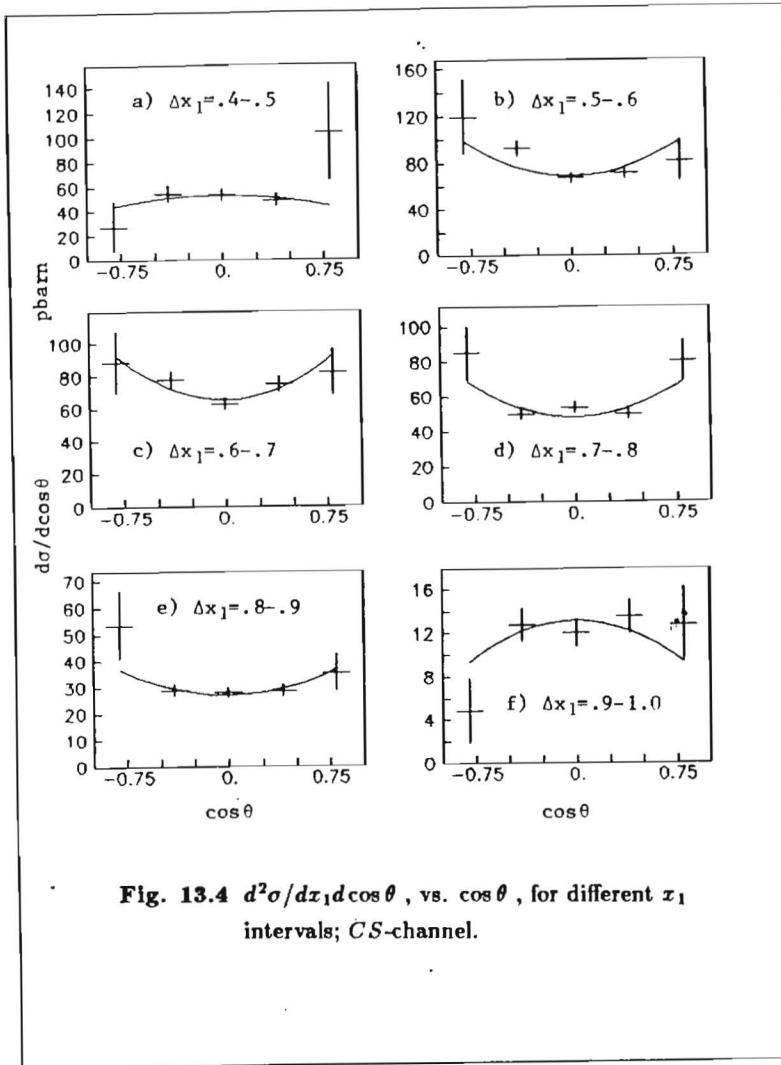


**Fig. 13.3**  $d^2\sigma/dx_1 d \cos \theta$ , vs.  $\cos \theta$ , for different  $x_1$  intervals;  $t$ -channel.



values for  $\lambda$  very similar to the ones discussed above. No evidence of large variation of  $\rho$  or  $\omega$  for different  $x_1$  bins was found.

The acceptance of our detector places a strong correlation between  $x_1$  and  $x_F$ , which is most prominent at large values. Figure 13.8 and Table XX show the dependence of  $\lambda$  on  $x_F$ , which is very similar in shape to the dependence on  $x_1$ .

Similar results on the  $x_1$  dependence of  $\lambda$  were found dividing the data into bins of mass or transverse momentum.

### 13.4 Summary and comments

Our data show that for  $x_F > 0.15$  the angular distribution of the

**Table XVIII** Value of the parameter  $\lambda$  in different  $x_1$  intervals.

$\Delta x_1$	T-CHANNEL			CS-CHANNEL		
	$\lambda$	$\sigma_\lambda$	$\chi^2$ (DOF=3)	$\lambda$	$\sigma_\lambda$	$\chi^2$ (DOF=3)
.4-.5	.66 ± .42		4.8	-.26 ± .47		3.4
.5-.6	.81 ± .31		10.8	.68 ± .37		8.0
.6-.7	.66 ± .58		3.0	.65 ± .30		2.4
.7-.8	.50 ± .23		0.8	.67 ± .33		6.7
.8-.9	.61 ± .31		0.1	.58 ± .38		2.2
.9-1.0	-.60 ± .24		3.7	-.44 ± .29		4.8

muon pair is typical of that arising from a largely transverse polarized virtual photon. At large values of  $x_1$ , or  $x_F$ , the shape of the angular distribution changes to that of a longitudinally polarized virtual photon.

This is a confirmation of an observation made by our collaboration on a previous sample of dimuon data collected in pion-nucleon interactions.<sup>21</sup> The statistical power of the new sample is significantly greater, and it is possible to measure more precisely the shape of the transition between the two spin alignments.

QCD calculations involving higher twist terms<sup>27</sup> predicted such an effect to be related to a component of the pion structure function which behaves as a constant in the region of large  $x_1$ . We have presented evidence for a finite intercept of the pion structure function in Chapter 12. Figure 13.9 shows the predicted behaviour of  $\lambda(x_1)$  using our measurement of the pion structure function. Curves a) and c) are

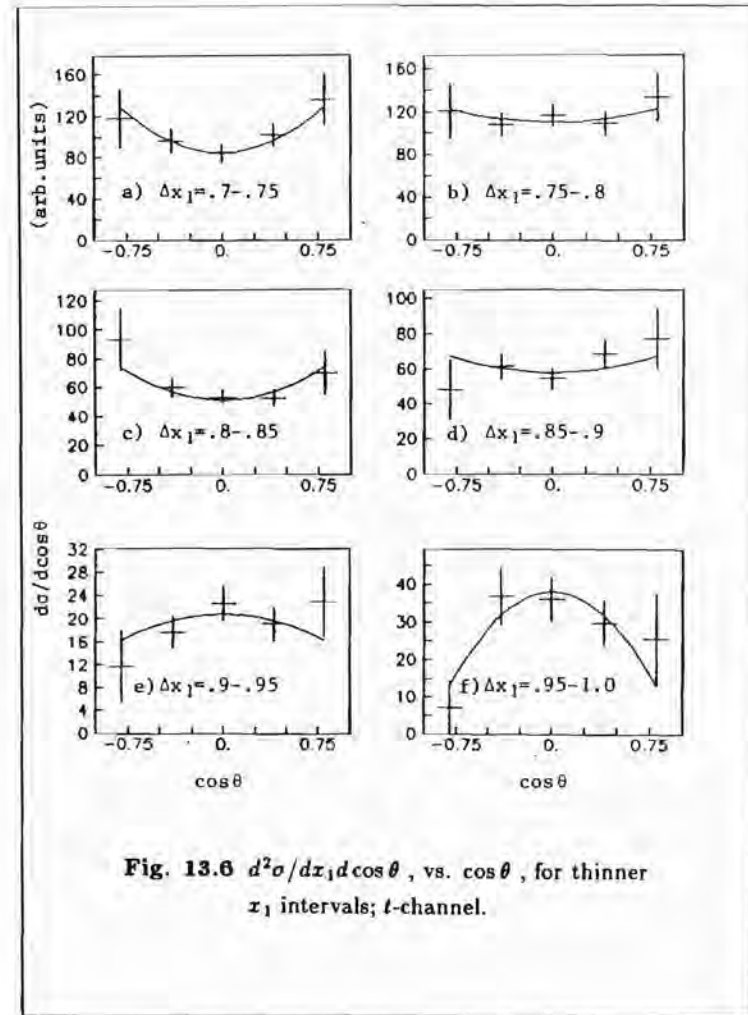


**Fig. 13.6**  $d^2\sigma/dx_1 d\cos\theta$ , vs.  $\cos\theta$ , for thinner  $x_1$  intervals;  $t$ -channel.

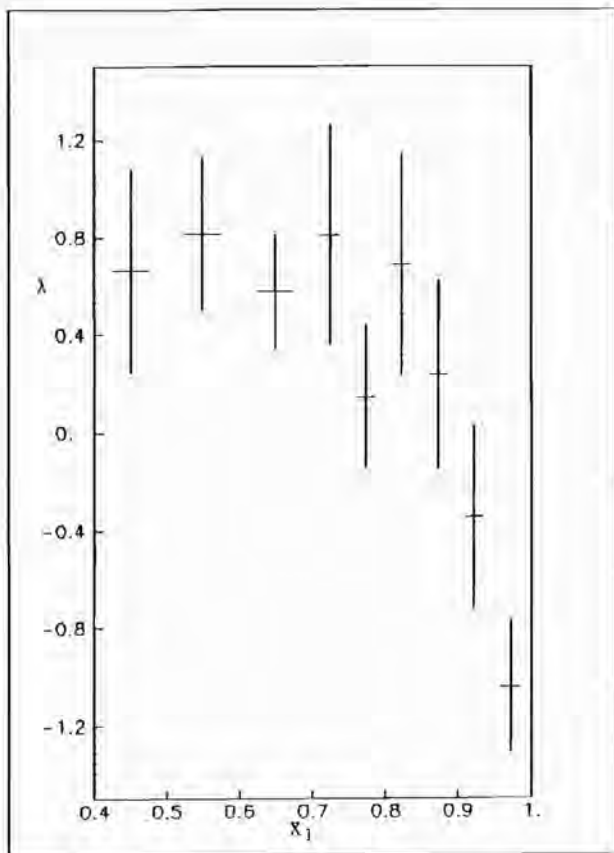


Fig. 13.7  $\lambda$  vs.  $x_1$  in the  $t$ -channel, for thinner  $x_1$  intervals.

Table XIX Value of the parameter  $\lambda$  in smaller bins of  $x_1$ , near the limit  $x_1 = 1$ , in the  $t$ -channel.

$\Delta x_1$	$\lambda$	$\sigma_\lambda$	$\chi^2(\text{DOF}=3)$
.70-.75	.83 $\pm$ .45		.4
.75-.80	.16 $\pm$ .30		.9
.80-.85	.71 $\pm$ .46		1.7
.85-.90	.25 $\pm$ .39		2.8
.90-.95	-.33 $\pm$ .37		2.7
.95-1.0	-1.02 $\pm$ .27		2.4

obtained from the pion structure function (Fit a) in Table XI, choosing for  $\beta$  the best fit value 1.59, and assigning to  $\gamma$  the values .0044 and .0076, respectively, corresponding to the  $\mp 1\sigma$  statistical deviations. Curve b) is obtained assigning to  $\gamma$  to the best fit value .0060, with  $\beta$  equal to 2, following reference 27. The curves are certainly compatible with the angular distribution measurement.

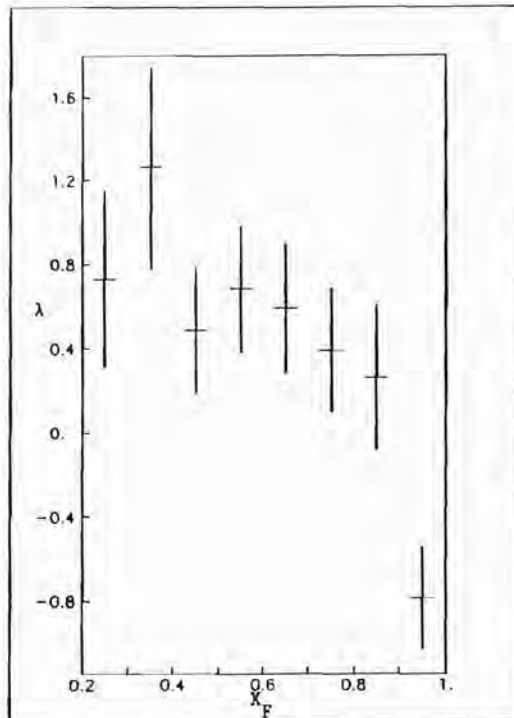


Fig. 13.8  $\lambda$  vs.  $x_F$  in the  $t$ -channel.

Table XX Value of the parameter  $\lambda$  in different  $x_F$  intervals, in the  $t$ -channel.

$\Delta x_F$	$\lambda \quad \sigma_\lambda$	$\chi^2$ (DOF=3)
.2 - .3	.73 $\pm$ .42	2.2
.3 - .4	1.26 $\pm$ .48	4.4
.4 - .5	.49 $\pm$ .30	1.3
.5 - .6	.68 $\pm$ .30	2.0
.6 - .7	.59 $\pm$ .31	1.0
.7 - .8	.39 $\pm$ .29	1.2
.8 - .9	.26 $\pm$ .34	2.8
.9 - 1.0	-.79 $\pm$ .24	6.8

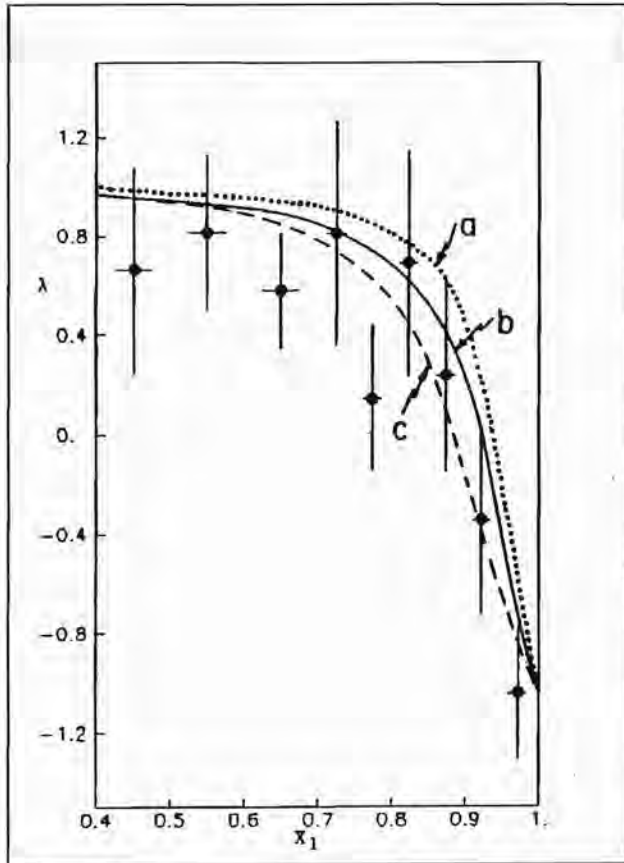


Fig. 13.9  $\lambda$  vs.  $x_1$  in the  $t$ -channel. The superimposed curves are described in the text.

## Chapter 14

### TRANSVERSE MOMENTUM DISTRIBUTION

#### 14.1 Definition of variables and results

The last aspect of muon pair production in pion-nucleon interactions which we shall cover in this dissertation is the transverse momentum. This has not played an important role in the previous chapters because of the smallness of the average squared transverse momentum compared with the scale of invariant masses and center-of-mass energy.

The analysis of the differential cross section  $d\sigma/dP_T$  has been performed binning the events in the variables  $P_T$ ,  $x_F$  and  $M$ . Figure 14.1 shows our results for the double differential expression  $d^2\sigma/dP_T dx_F$  as a function of  $P_T$ , for various intervals in  $x_F$ .

Recall our definition of  $x_F$ :

$$x_F \equiv \frac{P_L}{P_L^{max}} \quad ,$$

$$P_L^{max} = \frac{\sqrt{s}}{2} \left( 1 - 2 \frac{M^2 + M_R^2}{s} + \frac{(M^2 - M_R^2)^2}{s^2} - \frac{4P_T^2}{s} \right)^{\frac{1}{2}} \quad (11.1)$$

where the momenta are defined in the center-of-mass frame,  $\sqrt{s}$  is the center-of-mass energy, equal to 12.2 GeV,  $M$  is the invariant mass of

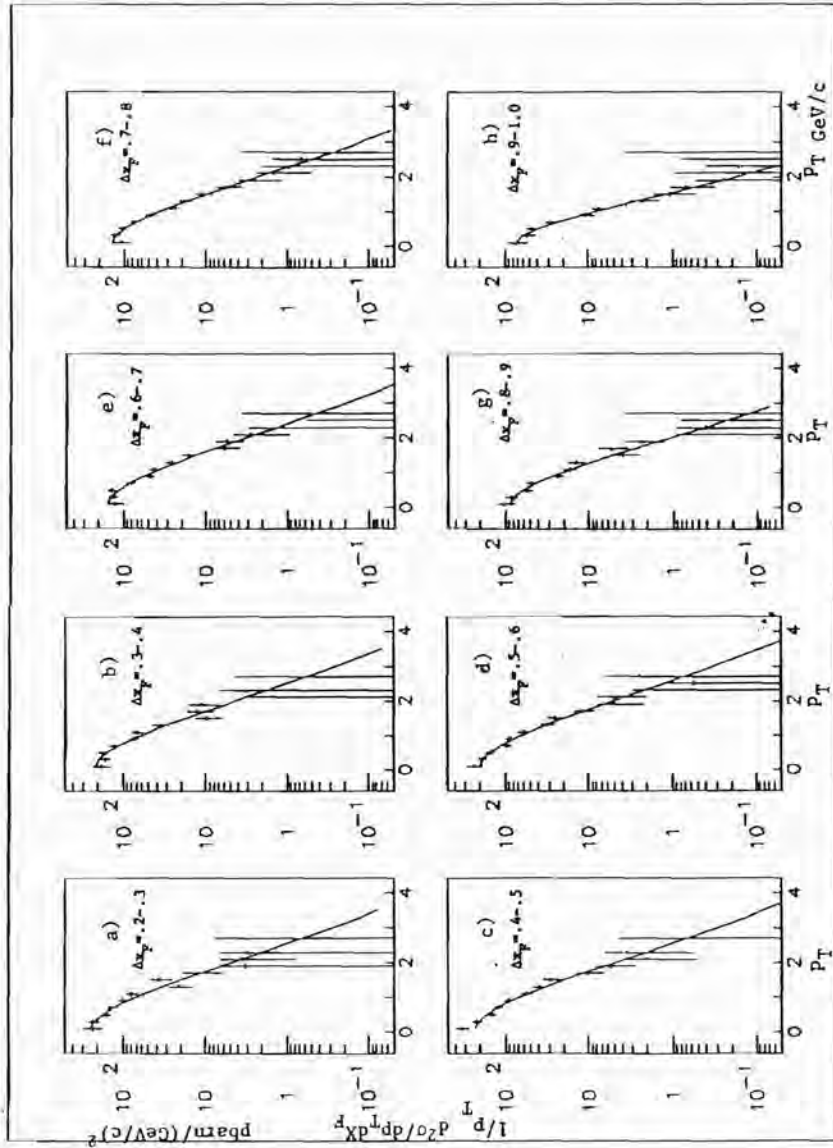


Fig. 14.1  $\frac{1}{P_T^2} \frac{d^2 \sigma}{dx_F dP_T}$  vs.  $P_T$ , for different  $x_F$  intervals.

the lepton pair, and  $M_R$  is the mass of the recoiling system, which we shall assume to be equal to  $0.94 \text{ GeV}/c^2$ . Observe that kinematics do not force the transverse momentum to vanish in the limit of  $x_F \rightarrow 1$ .†

We observe a significant decrease of  $\langle P_T \rangle$  and  $\langle P_T^2 \rangle$  for  $x_F$  approaching 1, as shown in Figures 14.2 and 14.3. Average values and statistical errors are shown in Table XXI.

No significant dependence of the transverse momentum distribution on the invariant mass was found.

The transverse momentum spectra are well described by the parametrization:

$$\frac{d^2 \sigma}{dP_T dx_F} \propto \frac{P_T/A(x_F)}{(1 - (P_T/A(x_F))^2)^6} \quad (14.1)$$

Fits to this form are superimposed to the measurements shown in Figure 14.1. The relation between the parameter  $A$  and the average transverse momentum of the distribution is  $\langle P_T \rangle = 0.430A$ . Table XXI shows the result of the fits in terms of the average transverse momentum of the distributions. Figure 14.4 shows the detector acceptance as a function of  $P_T$  in the region  $x_F > 0.9$ .

† Some reduction of the  $P_T^{max}$  is conceivable due to dependence of  $M_R$  on  $x_F$  and  $P_T$ . We can estimate the effect in the case of  $x_F \approx 1$  by supposing the recoiling system to consist of the spectator partons from the nucleon, and of a transverse gluon or quark with momentum equal to  $P_T$ , which balances the transverse momentum of the muon pair. Then we obtain  $M_R \approx x_F(1 - \tau)\sqrt{s}P_T$ . Inserting this expression in equation (11.1) we find that with our values for  $\sqrt{s}$  and  $\tau$  the maximum allowed transverse momentum for  $x_F = 1$  is  $4.3 \text{ GeV}/c$ . This is not much less than the value of  $5.2 \text{ GeV}/c$  obtained for  $M_R = 0.94 \text{ GeV}/c^2$ .

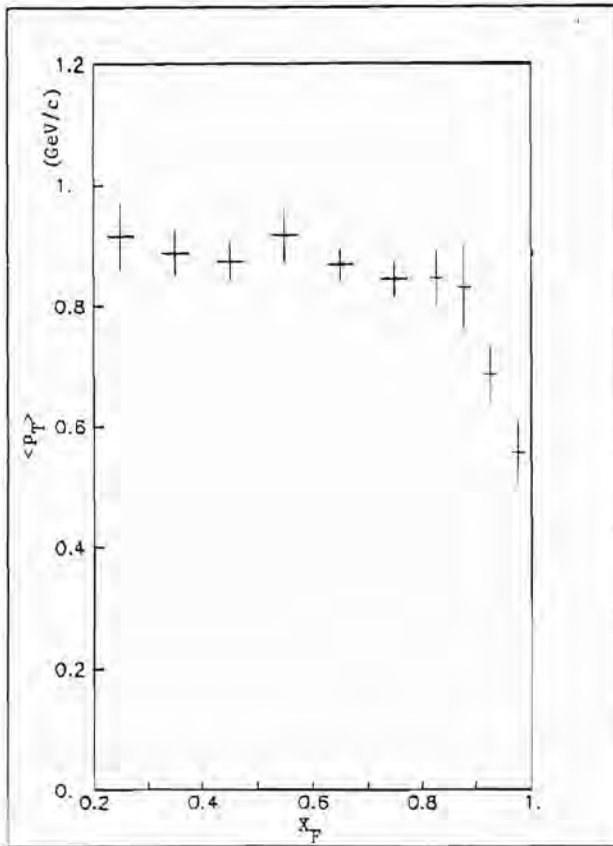


Fig. 14.2  $\langle P_T \rangle$  vs.  $x_F$ .

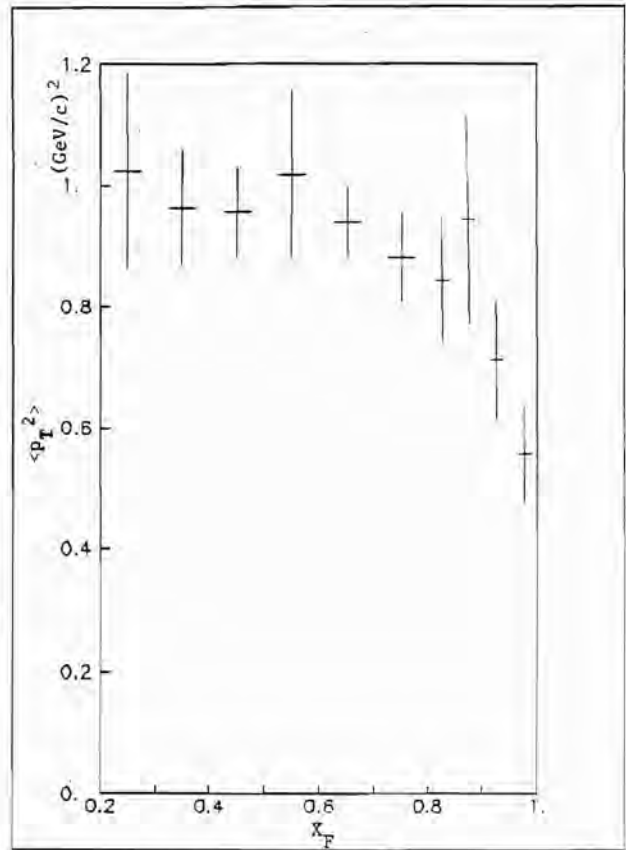


Fig. 14.3  $\langle P_T^2 \rangle$  vs.  $x_F$ .

Table XXI Values of  $\langle P_T \rangle$  and  $\langle P_T^2 \rangle$  in different  $x_F$  intervals.

The last two columns refer to the result of a fit to  $d\sigma/dP_T$  according to equation (14.2).

$\Delta x_F$	$\langle P_T \rangle$ GeV/c	$\langle P_T^2 \rangle$ (GeV/c) <sup>2</sup>	$\langle P_T \rangle_{\text{fit}}$ GeV/c	$\langle P_T^2 \rangle_{\text{fit}}$ (GeV/c) <sup>2</sup>	$\chi^2/\text{DOF}$
.2 - .3	.915 ± .053	1.023 ± .162	.892 ± .041	12.0/11	
.3 - .4	.887 ± .037	.963 ± .095	.892 ± .034	16.1/11	
.4 - .5	.875 ± .031	.955 ± .076	.905 ± .032	10.5/11	
.5 - .6	.917 ± .044	1.018 ± .138	.926 ± .030	9.9/11	
.6 - .7	.869 ± .026	.940 ± .059	.899 ± .031	13.6/11	
.7 - .8	.844 ± .029	.881 ± .073	.862 ± .028	2.8/12	
.80-.85	.846 ± .046	.846 ± .104	.820 ± .048	13.4/8	
.85-.90	.831 ± .070	.947 ± .173	.747 ± .070	11.6/8	
.90-.95	.689 ± .045	.714 ± .096	.669 ± .036	6.3/9	
.95-1.0	.560 ± .052	.560 ± .079	.577 ± .057	4.0/8	

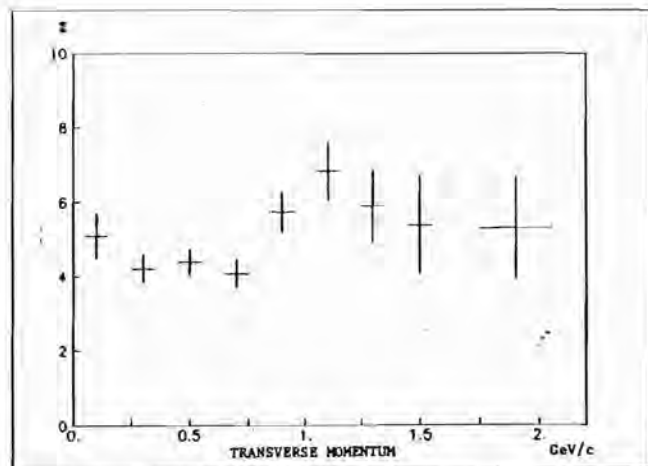


Fig. 14.4 Detector efficiency vs.  $P_T$  for events with  $x_F > 0.9$ .

## 14.2 Comparisons with expectations

We have measured values for the average  $P_T$  and for the average  $P_T^2$  smaller than those observed in previous observations with larger center-of-mass energy.<sup>20</sup> Our result is compatible with the trend suggested by an experiment performed with lower energy.<sup>19</sup> This is at least qualitatively in agreement with QCD expectations.

A precise comparison between theory and observation is made difficult by the fact that the region  $P_T < 1$  GeV/c cannot be analyzed by perturbative techniques only. The limited number of events at larger  $P_T$  precludes comparison in the region where diagrams such as those in Figure 3.1.a,b might dominate.

The observation of the decrease of  $\langle P_T \rangle$  and  $\langle P_T^2 \rangle$  at large  $x_F$  is also in qualitative agreement with QCD. Various models describing the quark transverse momentum have been proposed, often with incompatible results in the limit of  $x_F \rightarrow 1$ , which can now be compared with our experimental observation.

## Chapter 15 OVERVIEW OF RESULTS

We have studied various aspects of the production of muon pairs in pion-nucleon interactions, in the region of  $x_F > 0.2$  and  $\sqrt{\tau} = M/\sqrt{s} > 0.33$ . The differential cross section  $d^2\sigma/dM dx_F$  has been analyzed using the model of Drell and Yan. Our results on the pion structure function are not incompatible with previous ones, but our greater sensitivity at large  $x_1$  favors a steeper behaviour of the structure function, as well as a finite intercept at  $x_1 = 1$ , measured with 3 standard deviations.

This effect is expected to be related to a change in the angular distribution of the muon pair. We indeed observe strong evidence of the predicted behaviour. In both the t-channel and the CS-channel the angular distribution changes from a 90%  $J_Z = \pm 1$  spin alignment for  $x_1 < 0.8$  to a distribution typical of  $J_Z = 0$  as  $x_1 \rightarrow 1$ .

Our result for the nucleon structure function is hardly consistent with parametrization of the nucleon quark densities based on deep inelastic scattering observations. Since different quark densities are measured by the different experiments, it is not immediately possible to identify the cause of the disagreement, such as a violation of the 'strong factorization hypothesis'. Still, a previous  $\pi N \rightarrow \mu^+ \mu^- X$  experiment<sup>10</sup> found good agreement with a similar parametrization,

so that our new result might indicate difficulties encountered by the Drell-Yan Model in the regions of rather small  $\sqrt{s}$  or large  $\tau$ .

The ambiguity in the normalization of the nucleon structure function, and also the difficulty in normalizing the pion structure function because of lack of acceptance at low  $x_1$ , prevent us from a direct measurement of the K-factor.

The transverse momentum distribution for the full sample of events is compatible with previous observations at different center-of-mass energies. We find also a clear decrease of the average  $P_T$  and  $P_T^2$  at large  $x_F$ , which adds interest to this already rather exciting region of the phase space. This observation cannot be explained by kinematic effects.

To conclude, we have found evidence for several aspects of muon pair production which are not predicted by the standard Drell-Yan Model, even after including QCD corrections in the leading-log approximation. Some of these effects can be accommodated by means of 'higher twist' calculations.

The importance of these results will be increased by scaling comparisons with other data sets. Results at larger  $\sqrt{s}$  and similar  $\tau$  are expected from an experiment looking mainly at the intermediate  $x_F$  region.<sup>28</sup> A better comparison will be possible with the data that we have recently collected at larger  $\sqrt{s}$ , and in wide ranges of  $x_F$  and  $\tau$ . In particular, scaling tests should allow us to confirm the contribution from higher twist effects, which would demonstrate a common source for the effects observed in the pion structure function and in the angular distribution at large  $x_F$ .

However, the results presented in this dissertation already represent strong evidence for interesting effects at large  $x_F$ , which reinforces the importance of the study of the production of lepton pairs

in hadronic interactions towards an understanding of the dynamics of the fundamental constituents of matter.

## REFERENCES

1. M. Gell-Mann and Y. Ne'eman, *The Eightfold Way*, Benjamin, New York (1964).
2. E.D. Bloom *et al.*, Phys. Rev. Lett. **23**, 930 (1969) ;  
M. Breidenbach *et al.*, Phys. Rev. Lett. **23**, 935 (1969);  
J.D. Bjorken, Phys. Rev. **179**, 1547 (1969) ;  
J.D. Bjorken and E.A. Paschos, Phys. Rev. **185**, 1975 (1969).
3. H.D. Politzer, Phys. Rep. **14**, 129 (1974).
4. D.J. Gross and F. Wilczek, Phys. Rev. Lett. **30**, 1343 (1973) ;  
H.D. Politzer, Phys. Rev. Lett. **30**, 1346 (1973).
5. J.H. Christenson *et al.*, Phys. Rev. Lett. **25**, 1523 (1970).
6. S.D. Drell and T.-M. Yan, Phys. Rev. Lett. **25**, 316 (1970).
7. R.P. Feynman, *Photon Hadron Interactions*, Benjamin, New York (1972) ;  
F.E. Close, *An Introduction to Quarks and Partons*, Academic Press, London (1979).
8. For a detailed review of the Drell-Yan physics see: *Proceedings of the Drell-Yan Workshop*, Fermilab (1982).
9. C.B. Newman *et al.*, Phys. Rev. Lett. **42**, 951 (1979) ;  
J. Badier *et al.*, Phys. Lett. **96B**, 422 (1980).
10. J. Badier *et al.*, Z. Phys. C, Particles and Fields, **18**, 281 (1983).
11. A.S. Ito *et al.*, Phys. Rev. **D23**, 604 (1981);  
D. Antreasyan *et al.*, Phys. Rev. Lett. **47**, 12 (1981); Phys. Rev. Lett. **48**, 302 (1982).
12. C. Kourkoumelis *et al.*, Phys. Lett. **91B**, 475 (1980).
13. G.E. Hogan *et al.*, Phys. Rev. Lett. **42**, 948 (1979).
14. D. Antreasyan *et al.*, Phys. Rev. Lett. **45**, 863 (1980).
15. R. Barate *et al.*, Phys. Rev. Lett. **43**, 1541 (1979).
16. J. Badier *et al.*, Z. Phys. C, Particles and Fields, **11**, 195 (1981).
17. J. Badier *et al.*, Phys. Lett. **89B**, 145 (1979).
18. J. Badier *et al.*, Phys. Lett. **104B**, 335 (1981) ;  
H.J. Frisch *et al.*, Phys. Rev. **D25**, 2000 (1982).
19. M. Corden *et al.*, Phys. Lett. **96B**, 417 (1980).
20. J. Badier *et al.*, Phys. Lett. **117B**, 372 (1982).
21. K.J. Anderson *et al.*, Phys. Rev. Lett. **43**, 1219 (1979).
22. G. Altarelli and G. Parisi, Nucl. Phys. **B126**, 298 (1977).
23. H.D. Politzer, Nucl. Phys. **B129**, 497 (1977) ;  
C.T. Sachrajda, Phys. Lett. **73B**, 185 (1978).
24. For a review and references on the topic of the transverse momentum in the Drell-Yan Process see: E.L. Berger, Ref. 8, p. 1.
25. R.K. Ellis, *Proceedings of the Moriond Workshop on Lepton Pair Production*, Les Arcs, p. 231 (1981) ;  
W.J. Stirling, Ref. 8, p. 131.
26. P.V. Landshoff, Phys. Lett. **66B**, 452 (1977) ;  
F.E. Close, F. Halzen and D.M. Scott, Phys. Lett. **68B**, 447 (1977) ;  
H. Hanada, T. Kaneko, N. Sakai and O. Savada, Progress of Theor. Phys. **60**, 1824 (1978).
27. E.L. Berger and S.J. Brodsky, Phys. Rev. Lett. **42**, 940 (1970) ;  
E.L. Berger, Z. Phys. C **4**, 289 (1980) ;  
S. Matsuda, Phys. Lett. **119B**, 207 (1982).

28. B. Betev *et al.*, NA10 contribution to the *XXII Conf. on High Energy Physics*, Leipzig (1984).
29. The members of the E615 collaboration are: C.E. Adolphsen, J.P. Alexander, K.J. Anderson, J.S. Conway, J.G. Heinrich, K.W. Merrit, A. Possoz, J.E. Pilcher - University of Chicago; E.I. Rosenberg, D.T. Simpson - Iowa State University; C. Bino Palestini, J.F. Greenhalgh, W.C. Louis, K.T. McDonald, S. Palestini, F.C. Shoemaker, A.J.S. Smith - Princeton University.
30. A.S. Carrol *et al.*, *Phys. Lett.* **80B**, 319 (1979).
31. G.D. Gollin, M.V. Isaila, F.C. Shoemaker and P. Surko, *IEEE Trans. Nuc. Sci.* **NS-26**, 59 (1979).
32. The trigger processor is also described in: J.F. Greenhalgh, *Proceedings of the Symposium on Recent Development in Computing, Processor and Software Research for High Energy Physics*, Guanajuato, Mexico (1984).
33. H.W. Atherton *et al.*, CERN Yellow Report **80-07** (1984).
34. B. Rossi, *High Energy Particles*, Prentice Hall, Englewood, NJ (1952).
35. A. Bodek and J.L. Ritchie, *Phys. Rev.* **D23**, 1970 (1981).
36. A.E. Brenner *et al.*, *Phys. Rev.* **D26**, 1497 (1982).
37. G. Bellettini *et al.*, *Nucl. Phys.* **79**, 609 (1966).
38. S.P. Denisov *et al.*, *Nucl. Phys.* **B61**, 62 (1973).
39. Parametrization I is derived from J.G.H. de Groot *et al.*, *Phys. Lett.* **82B**, 456 (1979) , *Z. Phys. C, Particles and Fields*, **1**, 143 (1979) ;  
parametrization II is from D.W. Duke and J.F. Owens, *Phys. Rev.* **D30**, 49 (1984).

